

Development of a Liquid-Fueled Micro-Combustor

by

Jhongwoo Jay Peck

B.S. Mechanical and Aerospace Engineering, Seoul National University, 2001
S.M. Aeronautics and Astronautics, Massachusetts Institute of Technology, 2003

Submitted to the Department of Aeronautics and Astronautics
in partial fulfillment of the requirements for the degree of

Doctor of Philosophy

at the

MASSACHUSETTS INSTITUTE OF TECHNOLOGY

June 2008

© Massachusetts Institute of Technology 2008. All rights reserved.

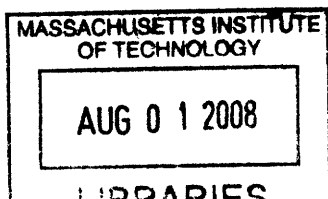
Author
Department of Aeronautics and Astronautics
May 23, 2008

Certified by
Ian A. Waitz
Jerome C. Hunsaker Professor
Head of the Department of Aeronautics and Astronautics
Thesis Supervisor

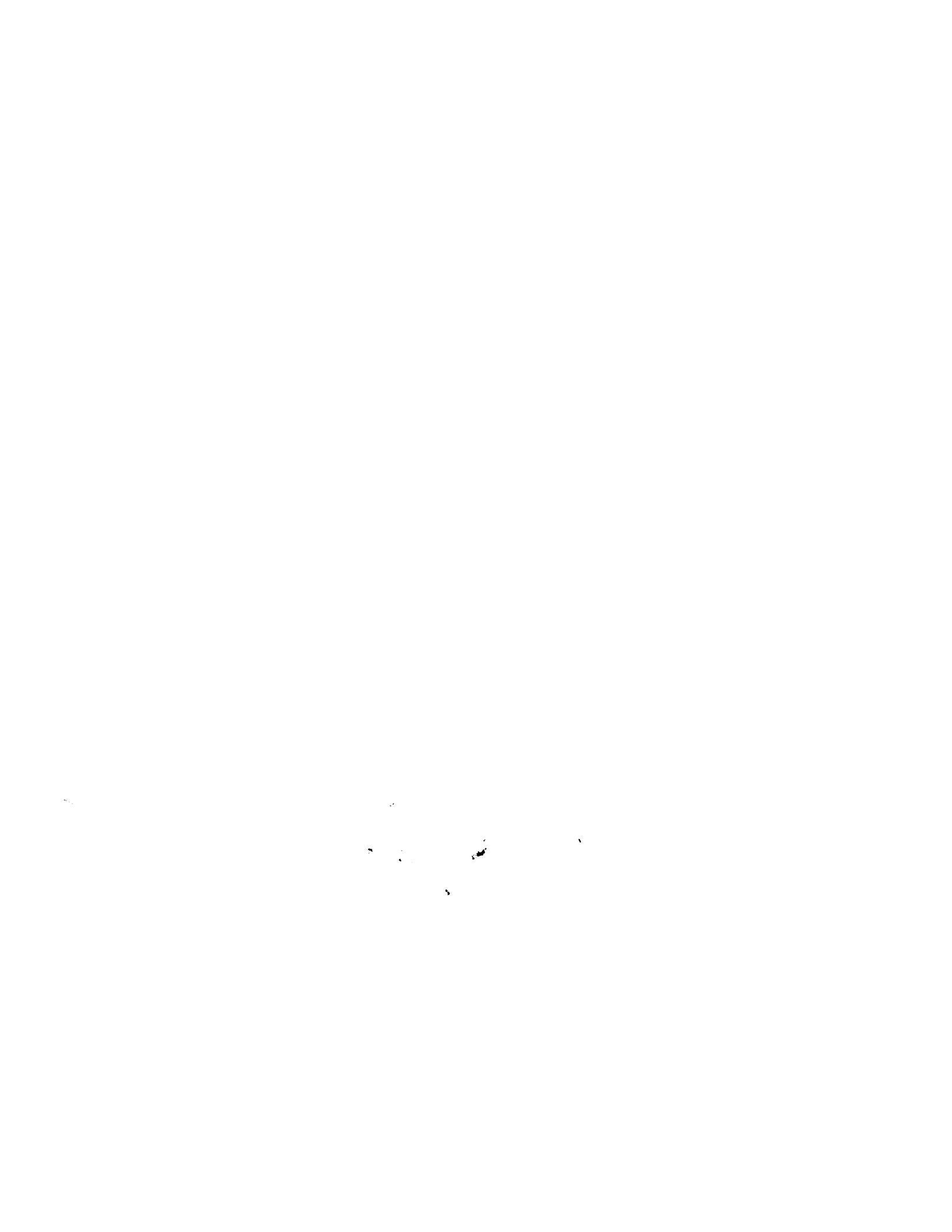
Certified by
Alan H. Epstein
R. C. MacLaurin Professor

Certified by
Stuart A. Jacobson
Principal Research Engineer

Accepted by
David L. Darmofal
Associate Department Head
Chair, Committee on Graduate Students



ARCHIVES



Development of a Liquid-Fueled Micro-Combustor

by

Jhongwoo Jay Peck

Submitted to the Department of Aeronautics and Astronautics
on May 23, 2008, in partial fulfillment of the
requirements for the degree of
Doctor of Philosophy

Abstract

Advances in Micro-Electro-Mechanical Systems (MEMS) have made possible the development of shirtbutton-sized gas turbine engines for use as portable power sources. As part of an effort to develop a microscale gas turbine engine, this thesis presents the modeling, design, fabrication, and experimental characterization of a micro-combustor that catalytically burns JP8 fuel. Due to high energy densities stored in hydrocarbon fuels, microscale heat engines based on them are estimated to have specific energies about one order of magnitude higher than those of current battery systems. In addition, utilizing a commonly available logistics fuel would provide advantages for military applications. Thus, a microengine burning JP8 fuel is attractive as a portable power source and potential replacement for batteries.

The thesis first presents a number of models developed to design the fuel vaporizer, the fuel-air mixing chamber, and the combustion chamber. Among these is a reduced-order mass transfer model that simulates catalytic combustion of a slow-diffusing hydrocarbon fuel. A two-phase heat transfer model was also developed to design an on-board fuel vaporizer with an array of micro-channels. Using the model results, a liquid-fueled micro-combustor test rig with a combustion chamber volume of 1.4 cc and an overall die size of $36.4\text{ mm} \times 36.4\text{ mm} \times 6.5\text{ mm}$ was built. This device is a hybrid structure composed of silicon, sapphire, and glass. Deep reactive ion etching was mainly used to fabricate the silicon parts. The sapphire and glass parts were built by ultrasonic machining.

The liquid-fueled micro-combustor was then experimentally characterized. Two configurations were tested and compared; one with the whole combustion chamber filled with a catalyst, and the other with a catalyst filling the chamber only partially. In the fully-loaded configuration, JP8 combustion was stably sustained at mass flow rates up to 0.1 g/sec , and an exit gas temperature of 780 K , an overall combustor efficiency of 19%, and a power density of 43 MW/m^3 were achieved. The primary limitation on increasing the mass flow rates and temperatures further was structural failure of the device due to thermal stresses. With the partially-loaded configuration,

a mass flow rate of 0.2 g/sec , and a corresponding power density of 54 MW/m^3 were obtained. The exit gas temperature for the partially-loaded configuration was as high as 720 K , and the maximum overall efficiency was over 22% . Although the reduced amount of catalyst led to incomplete combustion, smaller thermal losses resulted in an increase in the overall combustor efficiencies and power densities. The overall efficiency and the exit gas temperature were lower than the operational requirement of the microengine in both of the device configurations. A non-dimensional operating map was constructed based on the experiment, and suggestions for future liquid-fueled micro-combustors were made; to achieve maximum efficiency for a volume as small as possible, improving the thermal efficiency would be necessary.

Thesis keywords: Power-MEMS, microengine, micro-combustor, catalytic combustion, JP8 combustor, micro fuel vaporizer, micro-fabrication, deep reactive ion etching

Thesis Supervisor: Ian A. Waitz
Title: Jerome C. Hunsaker Professor
Head of the Department of Aeronautics and Astronautics

Acknowledgments

This thesis was completed with help of many people. First and foremost, I sincerely thank my advisor Professor Ian Waitz. His extraordinary guidance and encouragement made this work possible, and he deserves the greatest acknowledgment.

Professor Alan Epstein served as a member of my thesis committee. I am thankful for his insightful advice during the course of this research. I am truly grateful also to Dr. Stuart Jacobson for managing the microengine program and serving in the thesis committee. He provided precious advice throughout the research.

Dr. Chris Spadaccini and Professor Zolti Spakovszky willingly became readers of the thesis. I appreciate their valuable comments.

My gratitude extends to the fellow students who worked on the microengine project with me. Dr. Chiang Juay Teo has been a close friend and good counselor. Bernard Yen shared useful tips in the cleanroom.

Our wonderful micro-fabrication team also deserves thanks. Dr. Hanqing Li, Dr. Haifeng Dong, and Linhvu Ho provided helpful advice on the micro-fabrication. Dr. Woo Sik Kim, purely out of friendship, helped me with doing the micro-fabrication, coating catalysts, and taking SEM images.

During my stay in the Gas Turbine Laboratory, it was my privilege that I was raised by the excellent faculty. This includes Professor Jack Kerrebrock, Professor Edward Greitzer, Dr. Gerald Guenette, and Dr. Choon Tan. I also owe many thanks to the technical and administrative staff at the GTL: Dr. Yifang Gong, James LeTendre, Lori Martinez, Holly Anderson, Susan Parker, and Diana Park.

Robin Palazzolo at Professor Waitz's office, Marie Stuppard at the department office, and Maria Brennan at the International Student Office should also receive my special thanks as their aid was just as essential as the academic guidance.

Finally, I thank my parents and brother whose love and care carried me through. My wife Hyeju and my first son Nathan should be esteemed for their support.

This research was sponsored by DARPA and the U.S. Army Research Laboratory under the Collaborative Technology Alliance Program.

Contents

1	Introduction	23
1.1	Need for portable power sources	23
1.2	Power-MEMS	24
1.2.1	Applications	24
1.2.2	Pertinent technologies	25
1.3	MIT microengine	27
1.4	Motivation and objectives of the research	32
1.5	Contributions of the research	35
1.6	Review of previous research	36
1.6.1	Previous MIT micro-combustor research	36
1.6.2	Other microscale combustion research	46
1.7	Micro-combustor challenges	48
1.7.1	Short residence time for high power density devices	49
1.7.2	Large heat loss	49
1.7.3	Materials and fabrication constraints	51
1.7.4	Challenges specific to the use of liquid-fuels	52
1.8	Organization of the thesis	54
2	Experimental Apparatus Design	57
2.1	Material selection	58
2.2	Combustor volume	59
2.2.1	Overview of the model	60
2.2.2	Governing equations	62

2.2.3	Results	66
2.2.4	Summary of the combustor volume model	68
2.3	Fuel vaporizer	68
2.3.1	Two-region heat transfer model	73
2.3.2	Results	76
2.3.3	Summary of the fuel vaporizer model	78
2.4	Fuel injection holes and mixing chamber	78
2.5	Packaging and fluid connections	81
2.6	Clamps	86
2.7	Final design	86
2.8	Chapter summary	90
3	Apparatus Fabrication and Experimental Setup	91
3.1	Silicon micro-fabrication	91
3.1.1	Overview	91
3.1.2	Photolithography	93
3.1.3	Deep Reactive Ion Etching	95
3.1.4	Silicon fusion bonding	95
3.1.5	Silicon-to-glass anodic bonding	97
3.2	Ultrasonic machining	102
3.3	Preparation of the catalytic inserts	104
3.4	Experimental setup and diagnostics	106
3.5	Chapter summary	108
4	Experimental Characterization	111
4.1	Ignition procedure of catalytic combustion	111
4.2	Catalytic JP8 combustion	112
4.2.1	Temperature response	112
4.2.2	Efficiency breakdown	117
4.2.3	Non-dimensional operating map	118
4.3	Catalytically-anchored gas-phase combustion	124

4.3.1	Temperature response	126
4.3.2	Efficiency breakdown	126
4.4	Device comparison	127
4.5	Catalytic combustor design case studies	131
4.5.1	Case #1: Liquid-fueled micro-combustor revisited	133
4.5.2	Case #2: Combustor for TPV application	137
4.6	Performance of the fuel vaporizer	139
4.7	Assessment of device degradation	139
4.8	Chapter summary	143
5	Summary and Conclusions	145
5.1	Summary of research	145
5.2	Review of contributions	147
5.3	Recommendations for future work	149
A	Drawings of Photomasks	151
B	Mechanical Drawings of Ultrasonically Machined Parts	159
C	Monte-Carlo Simulation on the Fuel Vaporizer Design Model	163
D	Heat Loss Model	165
D.1	Convective heat loss	166
D.2	Radiative heat loss	167
D.3	Conductive heat loss	167
E	Uncertainty Analysis on Experimental Measurements	169
E.1	Uncertainties in the independent measurements	169
E.2	Uncertainties in the derived quantities	170
E.2.1	Equivalence ratio	170
E.2.2	Overall combustor efficiency	171
E.2.3	Chemical efficiency	172
E.2.4	Thermal efficiency	173

E.2.5 Peclet number 174

List of Figures

1-1	Potential for power-MEMS technologies	26
1-2	Cross-sectional view of the MIT microengine (a) and schematic of the fully packaged engine system (b) (Courtesy of Diana Park)	29
1-3	Schematic (a) and SEM image (b) of three-stack silicon micro-combustor [1]	38
1-4	Schematic (a) and SEM image (b) of six-wafer engine static structure [1]	40
1-5	Exit gas temperature (a) and combustor efficiency (b) vs. mass flow rate for premixed hydrogen-air combustion in the six-wafer micro-combustor [1]	41
1-6	Combustor efficiency for six-wafer micro-combustor with ethylene-air (a) and propane-air (b) [1]	42
1-7	Cross-sectional diagram of the dual-zone micro-combustor [2]	44
1-8	Schematic of the catalytic micro-combustor (adapted from Spadaccini [2])	46
1-9	Development paths of the MIT micro-combustor	47
2-1	Definition of the control volume for the combustor volume design model	62
2-2	Results of the catalytic combustion model for various equivalence ratios (tube diameter = $700\ \mu m$, $P = 2.0\ atm$)	69
2-3	Results of the catalytic combustion model for various tube diameters ($\phi = 1.0$, $P = 2.0\ atm$)	70
2-4	Results of the catalytic combustion model for various pressures ($\phi = 1.0$, tube diameter = $700\ \mu m$)	71

2-5	Final design of the combustion chamber layer	72
2-6	Thermocouple locations	72
2-7	Illustrative description of the two-region heat-transfer model	74
2-8	Modeling results for various design cases ($\dot{m}_f = 0.04\text{ g/sec}$, $D = 500\ \mu\text{m}$, and $N = 49$, unless otherwise noted)	79
2-9	Final design of the fuel vaporizer layer (a) and a zoom-in view (b)	80
2-10	Fuel injection holes viewed from above (a) and below (b)	82
2-11	Penetration of a jet injected into a cross-flowing air [3]	82
2-12	Normalized coverage of the injected fuel vapor as a function of the hole diameter	83
2-13	Fuel-air mixing chamber layer	83
2-14	Extended packaging block	85
2-15	Finite element model of the extended packaging	85
2-16	Schematic of a spring-laoded clamp that holds the parts together	86
2-17	Exploded view of the experimental apparatus	88
2-18	Flow paths in the experimental apparatus	88
2-19	Schematic of the experimental apparatus assembly	89
2-20	Schematic of the fully packaged test bed	89
3-1	Label, material, features, and fabrication method for each part	92
3-2	Schematic description of the micro-fabrication procedure (not to scale)	94
3-3	Layer 1 after Deep Reactive Ion Etching	96
3-4	Infrared images taken during the silicon direct bonding: immediately after contact (a), after the voids were pressed down (b), and after annealing for an hour (c)	99
3-5	Picture of the bonded wafers for Layers 3 and 4	99
3-6	Front side of the completed silicon piece (showing the front side of Layer 3)	100
3-7	Back side of the completed silicon piece (showing the back side of Layer 4)	101

3-8	Schematic of anodic bonding between silicon and SD-2 glass	101
3-9	SD-2 glass and silicon pieces mounted in an anodic bonding chuck . .	102
3-10	Electric current across the silicon-SD2 interface during anodic bonding under 1200 V	103
3-11	Layers 1 and 2 anodically bonded	103
3-12	Picture of ultrasonically machined Layer 2 (SD-2 glass)	104
3-13	Picture of ultrasonically machined Layer 5 (sapphire)	105
3-14	Picture of ultrasonically machined exit tube (sapphire)	105
3-15	Prepared catalytic insert	107
3-16	Test stand assembly built out of steel	107
3-17	Complete test rig	108
3-18	Schematic of the experimental facility	109
4-1	Photograph of the JP8 combustor in operation (a) and a zoomed view (b)	113
4-2	Thermal infrared image of the liquid-fueled micro-combustor during JP8 combustion ($\phi = 1.1$, $\dot{m} = 0.1 \text{ g/sec}$)	114
4-3	JP8 combustion result: exit gas temperature vs. equivalence ratio for different mass flow rates	115
4-4	JP8 combustion result: exit gas temperature (a) and structural tem- perature (b) vs. mass flow rate for different equivalence ratios	116
4-5	JP8 combustion result: efficiency breakdown for $\phi = 1.1$	119
4-6	JP8 combustion result: Peclet number vs. mass flow rate	121
4-7	JP8 combustion result: lines of constant Peclet numbers on a chemical efficiency and thermal efficiency plane	122
4-8	JP8 combustion result: chemical efficiency (a) and thermal efficiency (b) vs. Peclet number	123
4-9	Relevant parameters divided into non-dimensional parameters	125
4-10	Partially-loaded catalytic micro-combustor result: temperatures vs. mass flow rate for $\phi = 0.9$	127

4-11	Partially-loaded catalytic micro-combustor result: efficiencies vs. mass flow rate for $\phi = 0.9$	128
4-12	Device comparison: exit gas temperatures (a) and structural temperatures (b) vs. mass flow rate for $\phi = 0.9$	129
4-13	Efficiency breakdown comparison between the fully-loaded and the partially-loaded catalytic combustors ($\phi = 0.9$)	130
4-14	Comparison of chemical efficiencies vs. Peclet number between the fully-loaded and the partially-loaded (with corrected Peclet number) catalytic combustors	131
4-15	Device comparison on a non-dimensional operating space	132
4-16	Non-dimensional operating map of liquid-fueled micro-combustor	133
4-17	Peclet number vs. mass flow rate for all data acquired in the liquid-fueled micro-combustor	135
4-18	Thermal efficiencies vs. Peclet number for the liquid-fueled micro-combustor and the silicon micro-combustor based on catalytic propane combustion	135
4-19	Non-dimensional operating map of silicon micro-combustor based on catalytic propane results (data obtained from Spadaccini [2])	136
4-20	Boiling front formed in the middle of the fuel supply channel at low fuel flow rates	140
4-21	Fuel injection holes before testing (a) and after 10 hours of operation (b)	141
4-22	Catalytic insert before testing (a) and after 10 hours of operation (b)	142
A-1	Mask #1	151
A-2	Mask #2	152
A-3	Mask #3	153
A-4	Mask #4	154
A-5	Mask #5	155
A-6	Mask #6	156
A-7	Mask #7	157

B-1	Layer 2 (SD-2 glass)	159
B-2	Layer 5 featuring the combustion chamber (sapphire)	160
B-3	Exit tube (sapphire)	161
D-1	Control volume for heat loss calculations	166

List of Tables

1.1	Specific energies and energy densities of different fuels for a power-MEMS device	33
1.2	Comparison of all the gas-phase micro-combustors	45
1.3	Comparison of micro-combustors from other research groups	49
2.1	Operational specifications of the liquid-fueled micro-combustor	58
2.2	Fluid properties used for the solutions	67
2.3	Variances in the estimated reaction times [<i>ms</i>] (and deviations from the baseline value, 1.54 <i>ms</i>) due to uncertainties in the fluid properties	67
2.4	Fluid properties of JP8	76
2.5	List of the vaporizer design parameters and the dimensions set by the design model	77
2.6	Key dimensions of the experimental apparatus	87
3.1	Description of each photomask	92
3.2	List of equipments in the experimental facility	110
4.1	A workable set of design parameters for liquid-fueled catalytic combustor for a microscale TPV system	138
C.1	Input parameters for the Monte-Carlo simulation	164
C.2	Monte-Carlo simulation result: percentile	164
E.1	Uncertainties of the independently measured quantities	169
E.2	Uncertainties of the derived quantities	175

Nomenclature

Roman

A	area [m^2]
B	transfer coefficient
Bi	Biot number
$B.P.$	boiling point [K]
C	local concentration [mol/m^3]
C_b	bulk concentration [mol/m^3]
C_p	constant pressure specific heat of air [J/kgK]
D	diameter [m]
D_{ab}	molecular diffusion coefficient [m^2/sec]
Da	Damköhler number
g	constant of gravity [m/sec^2]
h	heat transfer coefficient [W/m^2K] / specific enthalpy [J/kg] / height [m]
h_f	heating value of fuel [J/kg] or [J/mol]
h_{fg}	latent heat of vaporization [J/kg]
h_m	mass transfer coefficient [m/sec]

J	mole flux [mol/m^2sec]
k	thermal conductivity [W/mK]
L	length scale [m]
M	molecular weight [g/mol]
\dot{m}	mass flow rate [kg/sec]
Nu	Nusselt number
P	pressure [Pa] or [atm]
p	periphery [m]
Pe	Peclet number
Pr	Prandtl number
q	heat flow [W]
q''	heat flux [W/m^2]
R	Gas constant of air [J/kgK]
R	radius [m] / thermal resistance [K/W]
r	radial location [m]
Ra	Rayleigh number
Re	Reynolds number
SA	surface area [m^2]
Sh_D	Sherwood number based on diameter
T	temperature [K]
t	time [sec]
U	velocity [m/sec]
u	velocity [m/sec]

V	volume [m^3]
v	diffusion volume
x	location [m]
y	location [m]
z	location [m]

Greek

α	thermal diffusivity [m^2/sec] / coefficient of thermal expansion [K^{-1}]
β	volumetric thermal expansion coefficient [K^{-1}]
δ	jet spreading [m]
ε	emissivity of thermal radiation
η	efficiency
μ	dynamic viscosity [Ns/m^2]
ν	kinetic viscosity [m^2/sec]
ρ	density [kg/m^3]
σ	surface tension [N/m] / Stefan-Boltzmann constant [W/m^2K^4]
τ	characteristic time [sec]
ϕ	equivalence ratio

Subscripts

<i>a</i>	air
<i>b</i>	boiling region
<i>cond</i>	conduction
<i>conv</i>	convection
<i>D</i>	diameter
<i>diff</i>	diffusion
<i>f</i>	fuel / fluid
<i>h</i>	heating region / hydraulic
<i>j</i>	jet
<i>l</i>	liquid / lower
<i>rad</i>	radiation
<i>res</i>	residence
<i>s</i>	solid structure
<i>u</i>	upper
<i>v</i>	vapor
0	initial
∞	ambient

Chapter 1

Introduction

1.1 Need for portable power sources

Personal electronic devices such as cellular phones, personal media players, digital cameras, and laptop computers are commonly used today. Market demand for these products is steadily growing. The current trend in these portable devices is towards including more features in a smaller form factor. As the devices have been getting smaller, it has come to a point where the battery is a factor that limits the device size. There is a need for compact and reliable power sources.

The U.S. military services also need electric power sources that are reliable and portable. Today's soldiers carry numerous electronic devices for communication, surveillance, target acquisition, and navigation. When infantry personnel are dispatched to a battlefield, they carry batteries to power their equipments such as portable radio communications (PRC), global positioning systems (GPS), night vision goggles, and range finders. They use both primary (non-rechargeable) and secondary (rechargeable) batteries; typically, rechargeable batteries are used for training due to low cost, and primary batteries for real operations. The reason for this is because primary batteries have longer shelf life, better specific energy (energy per unit mass), and wider range of operating temperatures. BA5590, a lithium sulfur dioxide (LiSO_2) primary battery system with a capacity rated as 200 Whr at room temperatures, is one of the most used batteries in the U.S. military. The U.S. military services pur-

chase about 350,000 BA5590 batteries every year. The BA5590 weighs about 1.2 *kg* with a package size of 880 *cc* (127 *mm* × 112 *mm* × 62 *mm*). When deployed in the field for several days, soldiers typically need 10 – 20 *W* continuous power, and this translates to tens of pounds of batteries. This limits other carrying resources, such as food, water, or ammunition.

1.2 Power-MEMS

There have been extensive efforts to invent a battery replacement technology. Progress in Micro-Electro-Mechanical Systems (MEMS) during the last few decades has opened a possibility that a micro-fabricated device could be used to generate electrical power. Power-MEMS is a field that explores the capabilities of MEMS technology for developing such power-generating devices. Diverse concepts are being pursued. Internal heat engines, fuel cells, and (thermo)photovoltaics are among them. Power-MEMS devices are often based on hydrocarbon fuels. The specific energy of hydrocarbons is larger than that of batteries by two orders of magnitude; hydrocarbons have a specific energy of approximately 40 *MJ/kg*, whereas the best lithium-ion batteries have about 0.5 *MJ/kg* for safe operation. Therefore, a hydrocarbon-based device with a chemical-to-electric efficiency of only a few percent could have benefits over batteries. Another noteworthy merit of fuel-burning devices is short charging time and ease of checking fill level. Fueling can be done in a matter of minutes as opposed to many hours for battery recharge. Power-MEMS manifests itself as a promising technology to resolve the need for high-density power sources.

1.2.1 Applications

Power-MEMS technologies, for the most part, aim to replace current battery systems that are in the tens-of-watts regime. Power systems for individual soldiers, such as described in the previous section, fall into this category. Small robotic platforms such as PackBot[®]¹ ask for high-power/high-density energy sources and thus, are an area

¹PackBot[®] is a trademark of iRobot.

in which a power-MEMS device could also replace batteries.

As for civil applications, laptop computers typically require 10 – 50 *W* power. Current laptop batteries can hold about 60 *Whr* of charges, providing up to 5 hours of battery life. Among other criteria, consumers often shop for laptops with a long battery life, so this is a potential market in which a high-density power-MEMS device can compete. ICAO (International Civil Aviation Organization) passed a regulation, effective since January 1, 2007, that allows airline passengers and crew to carry and use certain fuel cartridges on board [4]. So there is an open opportunity for portable fuel-burning generators to be used in laptop computers.

Portable generators are one of the potential markets as well. Due to lifestyle changes, portable power generators are a growing market. People enjoying activities such as camping and tailgating use portable generators to power diverse electronic gadgets. According to SBI (Specialists in Business Information) [5], the U.S. market for portable power generators with an output up to 15 *kW* was driven to \$723 million in 2006 at a compound annual growth rate (CAGR) of 21% since 2002. The market is expected to keep growing at a 19% CAGR through 2011. Although not specified outright in this report, a new market for a portable generator with sub-*kW* power is emerging owing to fuel cell technologies.

Figure 1-1 lists feasible implementations of power-MEMS technologies. Soldiers, laptop computers, and most robotic platforms are currently powered by batteries (primary and rechargeable), whereas portable generators and some robotic platforms use internal combustion engines. These applications fall into a category of 10 – 1000 *W* power. For smaller power/energy devices, batteries are likely to prevail for a time being. And for devices requiring larger powers, heat engines are expected to dominate. However, there exists a healthy market between them in which micro-fabricated power-generating devices may seriously contend.

1.2.2 Pertinent technologies

There are several competing power-MEMS technologies, and fuel cell is one of them. A fuel cell is an energy conversion device producing electricity between fuel (anode)

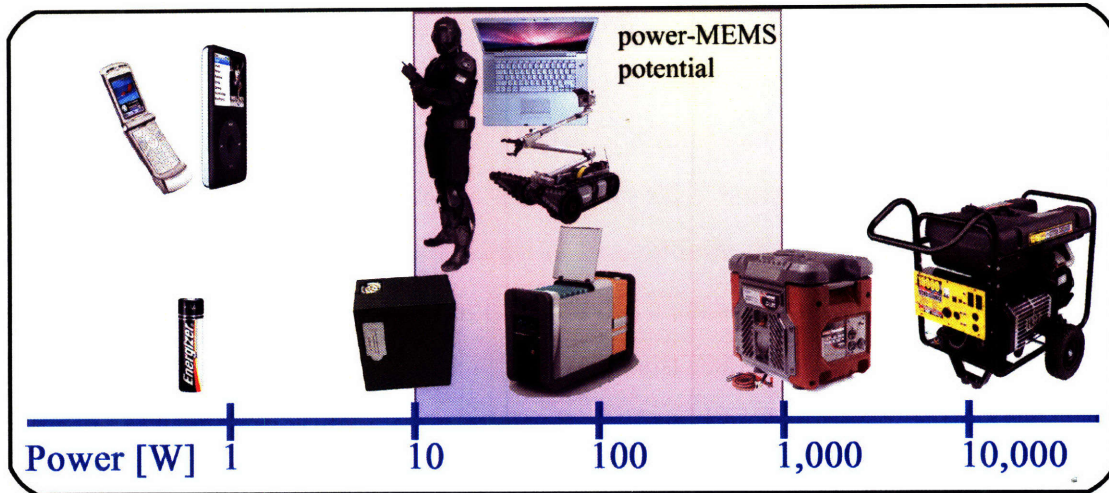


Figure 1-1: Potential for power-MEMS technologies

and oxidizer (cathode). The Direct Methanol Fuel Cell (DMFC) is one of the major fuel cell technologies, and is available commercially. Smart Fuel Cell is one of the market leading companies in fuel-cell-based mobile power supply. They manufacture fuel cell systems that can deliver $\sim 50\text{ W}$ of power out of a 7 kg (without fuel) device. One 5 L methanol cartridge (weighing 4 kg) can provide 4.5 kWhr of energy [6]. This translates to a specific energy of 1.5 MJ/kg , a three-fold increase over Li-ion batteries.

Proton Exchange Membrane Fuel Cell (PEMFC) is also recognized as a promising technology. With help of a fuel reformer, PEMFC is fuel-flexible allowing the use of high-density hydrocarbon fuels. Since hydrocarbon fuels have higher specific energy than methanol ($\sim 40\text{ MJ/kg}$ as opposed to methanol's $\sim 20\text{ MJ/kg}$), PEMFC is more prospective for higher specific energy than DMFC.

Thermophotovoltaics (TPV) are another technology being researched as a portable power source. A TPV system consists of a thermal emitter and a photovoltaic diode cell. The thermal emitter radiates photons when it is heated to $900 - 1300\text{ }^\circ\text{C}$. The photovoltaic diode absorbs these radiated photons and converts them into electricity. Photovoltaics, commonly known as solar cells, are effectively TPV devices in which the Sun functions as the emitter. Photovoltaics have been used to power calculators and watches for many years. Recently, owing to the advance of MEMS technology, highly efficient emitters and photovoltaic diodes can be micro-fabricated. If combined

with a heat source burning hydrocarbon fuels, TPV may be a contender as a battery replacement.

1.3 MIT microengine

MIT initiated a research program in the mid 1990's to develop a technology for microscale gas turbine engines. Epstein *et al.* [7, 8] led this initiative in designing and building shirtbutton sized gas turbine engines using silicon semiconductor micro-fabrication technology. These engines are about one hundredth the length scale of their conventional-sized counterparts, thus one millionth the volume. This is why they are called *microengines* [9]. Since power level scales with fluid mass flow rate, and flow rate scales with intake area, the microengines could produce about one ten-thousandth (1/10,000) the power level of the conventional-sized. This would be on the order of kilowatts, since typical power levels of those large engines are a few tens of megawatts. In reality, the microengines will have smaller pressure ratio and lower efficiencies, so the power level will be lower. Bench-top microengines are designed to produce about 10 W of electrical power or 0.1 N of thrust within a package about 1 cc in volume. The resulting engine power density² would be on the order of 10 MW/m³. As seen in Figure 1-2, the size of the engine itself would be negligible compared to the volume of fuel. So, with just 10% chemical-to-electric conversion efficiency³, the microengines would have a specific energy of 4 MJ/kg, which is about an order of magnitude higher than that of the best batteries available today.

Based on a gas turbine Brayton cycle, the MIT microengine contains all the functional components of a conventional gas turbine engine as shown in Figure 1-2. Air is drawn in axially through the inlet, and makes a right-angle turn into the compressor. Then fuel is injected into the compressed air. The fuel and air are mixed in the recirculation jacket, which provides 1) preheating of the fuel/air mixture and 2)

²This power density is based on the volume of engine only, excluding fuel or fuel storage device. Unlike power density, specific energy should be based on the system volume (or weight) including fuel system.

³Conventional gas turbine engines have efficiencies of 40-45%

thermal isolation of the combustion chamber. The fuel/air mixture enters the combustion chamber, in which combustion reactions take place; chemical energy stored in the fuel is converted to fluid thermal energy. Then, the high-enthalpy combustor exhaust passes through the turbine, and finally exits the engine. During this process, the turbine extracts mechanical power from the fluid, and the power is used to drive the compressor and the electric generator.

There exist challenges for developing novel technologies for these microscale gas turbine engines. Abridged descriptions of the technical challenges are listed below. During the past ten years, each of these challenging problems has been addressed, and many publications were made by the MIT research group.

Engine system design : The microengine is based on a Brayton cycle. The advantages of the Brayton cycle are simplicity and high power density. As this is a first-of-its-kind device based on pioneering technologies, simplicity is an attractive virtue. For the Brayton cycle to be self-sustaining, however, each component should meet a minimum efficiency (typically 40-50%). In addition, operating conditions such as temperatures, pressures, and mass flow rates are limited by fabrication and material constraints. For details on these issues references [7, 8, 9, 10, 11] should be consulted.

Turbomachinery : The current micro-fabrication techniques dictate the turbomachinery geometries to be only two-dimensional extrusions with constant blade heights. Due to fabrication and size issues, the compressor and turbine are limited to a single-stage as well. Furthermore, because of the small scale, the flow has low Reynolds numbers leading to high viscous losses. And due to unavailability of active turbine blade cooling, the spool between the turbine and the compressor must be short, so that the heat transferred to the turbine can be conducted and rejected to the compressor fluid. Although this is a simple way to keep the turbine below 950 K at which silicon starts to lose strength, it has a severe disadvantage of lowering the compression ratio. Finally, a sharp right-angle turn of intake flow into the compressor is detrimental to the compressor

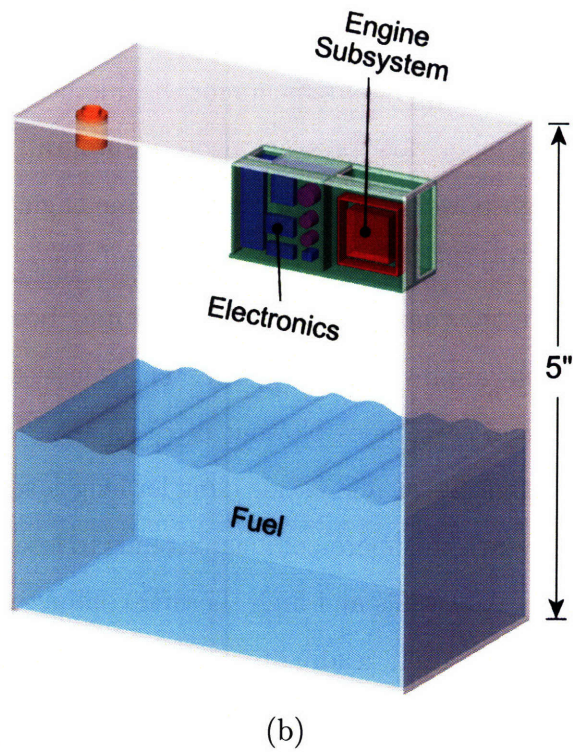
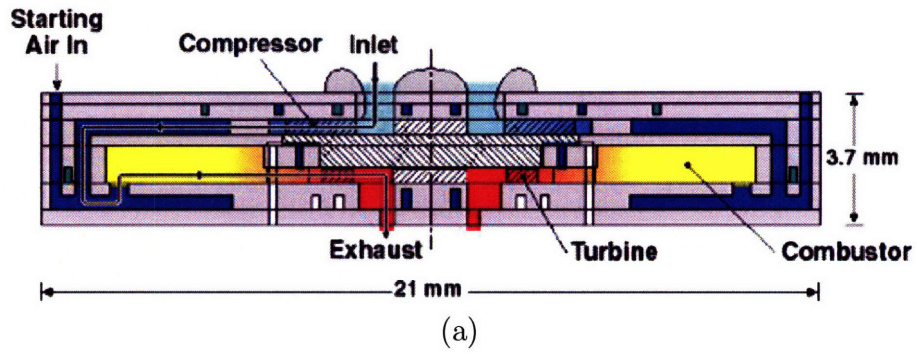


Figure 1-2: Cross-sectional view of the MIT microengine (a) and schematic of the fully packaged engine system (b) (Courtesy of Diana Park)

efficiency. Details on these topics can be found in references [10, 11, 12, 13].

Bearings : To get the required pressure ratios, the tip speed of the turbomachinery must be about 500 m/sec . With a rotor diameter of 4 mm , this translates to a rotational speed of approximately 2.4 million RPM. To achieve these high rotational speeds while retaining simplicity, air bearings were selected. Implementations of the air bearings pose challenges. Complex rotor and bearing dynamics problems must be resolved. Due to extremely tight clearance of the air bearings, even a small imbalance of the rotor disk can result in a failure of the device. Progress has been made in this subject, and test devices demonstrated repeatable high speed operation near tip speeds of 380 m/sec , making MEMS turbomachinery viable. More details are available in references [10, 11, 14, 15, 16, 17, 18].

Combustion : The key design requirements for the microengine combustor are temperature rise, efficiency, low pressure drop, structural integrity, ignition, and stability. The high power density of a gas turbine engine is realized by putting large mass flow rates through small cross sectional areas. As a consequence, flow residence times in the combustor are short and may become less than chemical reaction times that are invariant with size. This causes incomplete combustion, low efficiencies, and sometimes blowout of the flame. Moreover, due to larger heat transfer coefficients at microscale (smaller length scales result in thin thermal boundary layers), the micro-combustor tends to lose much heat through the combustor walls. Thin walls and high thermal conductivity of silicon make the structure nearly isothermal, leading to poor thermal isolation of the combustor. This exacerbate the heat loss problem. The non-adiabatic operation lowers combustor temperatures, and the low temperatures reduce chemical reaction rates, making the residence time issue more severe. Thus, fluid dynamics, chemical kinetics, and heat transfer are more strongly coupled and more significant in the micro-combustor. These challenges are reviewed in detail in Section 1.7, and references [1, 2, 19, 20, 21, 22, 23, 24, 25, 26].

Electrical machinery : Micro-electrical machinery is needed for power generation and to start the engine. The requirements for the devices of interest here differ from conventional-scale generators in that the power densities are at least two orders of magnitude larger. For simplicity, it is desirable for the electrical machinery to be integrated within the engine structure, typically on top of the compressor, because no additional bearings or structure would be needed. But this brings an adverse thermal environment for the generator, as the magnetic properties become deficient at high temperatures. The Curie temperature, above which a ferromagnetic material loses magnetization, is no higher than 1400 K for most useful ferromagnetic materials. Since silicon fusion bonding is followed by annealing typically at 1400 K , keeping the electrical machinery intact during the fabrication processes is challenging. References on this topic include [8].

Fabrication : Micro-fabrication technology is the key enabler of the microengine. However, the micro-fabrication techniques restrict the geometries that can be manufactured. In many cases, this makes development of the microengine quite challenging. For instance, inability to fabricate three-dimensional compressor/turbine blades undermines turbomachinery performance. Difficulty in etching high aspect ratio trenches to the very stringent tolerances is a concern for bearing development. Etch non-uniformity can unbalance the rotor disk and cause instability. Wafer bonding is demanding too; mis-alignment can also cause rotor imbalance, and any particles trapped between wafers can trigger leakage flow. Each component of the microengine, and the engine as a whole, must be designed to address these challenges. Additional details on the microengine fabrication can be consulted in references [10, 11, 27, 28, 29].

This thesis focuses on the combustion system for the MIT microengine. More specifically, a combustor utilizing the most common logistics fuel, JP8, is studied.

1.4 Motivation and objectives of the research

Previous researchers at MIT have made significant progress in the field of microscale combustion. Using platinum as a catalyst, stable propane combustion has been demonstrated at mass flow rates of 0.35 g/sec with exit gas temperatures of 1100 K within a combustor volume of 191 mm^3 , resulting in a combustor power density⁴ of about 1200 MW/m^3 [2]. Burning hydrogen fuel, a power density over 1400 MW/m^3 was achieved. Although hydrogen or propane are good fuels in general, in order for the microengine to be more practical, it is desirable to utilize a fuel that is easier to store, transport, and more readily available in the battlefield settings.

Table 1.1 compares the specific energy (energy per unit mass) and the energy density (energy per unit volume) of several fuels appropriate for power-MEMS applications. Because an attraction of a power-MEMS device relative to a battery is the large energy stored in a small volume (or weight), these are important criteria for judging which fuel is preferable. Liquid or liquefiable hydrocarbon fuels have high energy density. Although hydrogen's combustion times are very short, which is an advantage for a micro-combustor, it is considered not practical due to low energy density. Even at extremely high pressure (700 bar), the energy density of liquid hydrogen is only around the same order as a Li-ion battery. Only when hydrogen is stored as a form of metal hydride does the energy density become reasonably high, but its specific energy becomes so low that the system will be very heavy.

JP8 is a kerosene-based liquid jet fuel that is widely used for military operations. More than 5 billion gallons are consumed every year by the U.S. Air Force, the U.S. Army, and NATO. JP8 is the U.S. Army's logistic fuel, and is the fuel of choice for most Army vehicles, and also for appliances such as heaters, stoves, and power generators. JP8 is projected to remain as the primary fuel at least until 2025. For these military applications, it is an advantage for a portable power generating device to work on a fuel that is readily available in the battlefield.

There are significant challenges, however, to using JP8 in a microengine since

⁴fluid power over combustor volume

Fuel	Specific energy [MJ/kg]	Energy density [MJ/L]
hydrogen (room temperature)	143	0.0011
hydrogen (at 700 bar)	143	4.7
hydrogen (metal hydride)	2.1	11.4
methanol	19.7	15.6
ethanol	30.0	24.0
natural gas (at 200 bar)	53.6	10.0
liquefied propane	46.4	27.0
liquefied butane	49.1	28.1
LPG	34.4	22.2
gasoline	46.9	34.6
JP8	42.8	33.0
Li-ion battery	0.54-0.72	0.9-1.9

Table 1.1: Specific energies and energy densities of different fuels for a power-MEMS device

burning JP8 fuel in an environment resembling the microengine has not hitherto been done; the combustion model is not well known, and liquid-fuels necessitate additional component for vaporization. There is also an issue of device degradation due to coking. These challenges motivated the research program described in this thesis. Key scientific questions were identified and addressed. Test devices were designed and fabricated. Then, the devices were tested, and experimental data were collected, reduced, and analyzed. This thesis presents general guidelines for designing a combustor that burns liquid-fuels such as JP8 within several cubic centimeters of volume.

A liquid-fueled micro-combustor is a combustor with approximately one millionth the volume of a conventional gas turbine combustor, burning fuels that are in liquid-phase at standard temperatures and pressures. A liquid-fueled micro-combustor has many of the same technical challenges as a gaseous-fueled micro-combustor. However, there are several additional hurdles due to different combustion time-scales, liquid-phase at room conditions, and stability of the fuel molecules. Scientific issues associated uniquely with burning liquid-fuels at microscale are listed below. These points will be discussed in detail later in Section 1.7.4.

Combustion time-scales : The designer of a liquid-fueled micro-combustor needs to size the combustion chamber large enough so that the fuel and air mixture resides in the combustion chamber longer than it takes to complete the combustion reaction. The ratio between the flow residence time-scale and the reaction time-scale is defined as the Damköhler number:

$$Da \equiv \frac{\tau_{residence}}{\tau_{reaction}} \quad (1.1)$$

The Damköhler number is required to be greater than unity. However, due to unavailability of a chemistry model for catalytic JP8 combustion, it is difficult to estimate the reaction time-scales. Thus, determining the minimum combustor volume for a JP8-fueled combustor is challenging.

Fuel vaporization : A liquid-fueled combustor differs from a gaseous-fueled combustor in that the former requires a fuel atomizer or vaporizer. The fuel vaporizer should be compact, and it should be easily integrated with the engine system. Further, there is limited experience in designing vaporizers at this scale.

Coking : JP8 decomposes at high temperatures and leaves residual carbons on device surfaces. This is referred to as coking or sooting. The residual carbons may build up and clog the fuel flow paths including the vaporizing surfaces and the fuel injection nozzles. In addition, the coking can degrade the catalyst. Device deterioration by coking must be evaluated.

The research presented in this thesis attends to these scientific/technical problems, aiming to become a general reference in designing a microscale liquid-fuel burning system. To do so, a design model that can estimate the time-scale of the catalytic JP8 combustion must be developed. The best scheme for fuel vaporization needs to be selected, and a MEMS fuel-vaporizer must be designed and built. Research objectives also include fabrication and demonstration of a working JP8 combustor that can be integrated in the MIT microengine. Based on data collected in the test devices, general design guidelines for microscale liquid-fueled micro-combustor should

be suggested.

1.5 Contributions of the research

The contributions of this research project include:

- ***Demonstration of JP8 combustion in a microengine setting***

Catalytic JP8 combustion was achieved at a mass flow rate of 0.2 g/sec , and a corresponding exit gas temperature of 640 K within a combustor volume of 1.4 cc . This results in a combustor power density of 54 MW/m^3 and an overall efficiency of 19%. However, operational requirements of the microengine were not achieved mainly due to large thermal loss. Based on the experimental results, recommendations for better thermal management were made.

- ***Development of a design methodology for catalytic combustion time-scales***

Catalytic combustion of heavy hydrocarbon fuels is not well understood to date. A simplified model was developed to estimate catalytic combustion time-scales, based on an assumption that catalytic combustion is a diffusion-limited process. Although this model is only applicable for diffusion-limited catalytic combustion, it can serve as a preliminary design tool in estimating the combustion time-scale and determining the required combustor volume for slow-diffusing fuels.

- ***Design, fabrication, and integration of an on-board MEMS fuel vaporizer***

A two-phase heat transfer model was constructed to calculate the required surface area for vaporizing the fuel. An on-board fuel vaporizer consisting of an array of micro-channels in parallel was designed using the model, and fabricated with silicon micro-fabrication techniques. Its operability was successfully demonstrated at a fuel flow rate up to 0.01 g/sec , which is approximately a

quarter of the design specification. Inability to test at the design flow rate was because the total mass flow rate could not be pushed further.

- ***Construction of an empirical non-dimensional operating map***

A non-dimensional operating map was generated based on the experimental data acquired in the test apparatus. The operating map is useful in explaining the characteristics of a liquid-fueled catalytic micro-combustor and in designing a similar combustor. Based on analyses via the non-dimensional operating map, suggestions for future liquid-fueled micro-combustor design were made.

- ***Investigation of device deterioration***

After over ten hours of operation, degradation of the device was studied. Although some local destruction of the catalyst was observed, the exit gas temperature response was repeatable for the same conditions, showing that the catalyst did not degrade. Deposition of decomposed carbon was observed on the walls of the device, especially along the fuel flow path. However, pressure change in the fuel supply tube due to a blockage in the fuel flow path was not observed.

1.6 Review of previous research

1.6.1 Previous MIT micro-combustor research

Feasibility study of hydrogen combustion at microscale

Waitz, Gauba, and Tzeng [20, 21] were the first to study combustion systems for microengines. To meet operational specifications for the microengine combustion system⁵, a lean-burning hydrogen-air combustor was elected as a strategy. In a flame tube experiment, they proved that this concept was appropriate for micro-combustors. To further study the subject, a model micro-combustor was built. This combustor

⁵At the initial stage of the project, operational specifications for the combustor were 4 atm of inlet total pressure, 0.18 g/sec of mass flow rate, 500 K of inlet total temperature, and 1600 K of exit temperature.

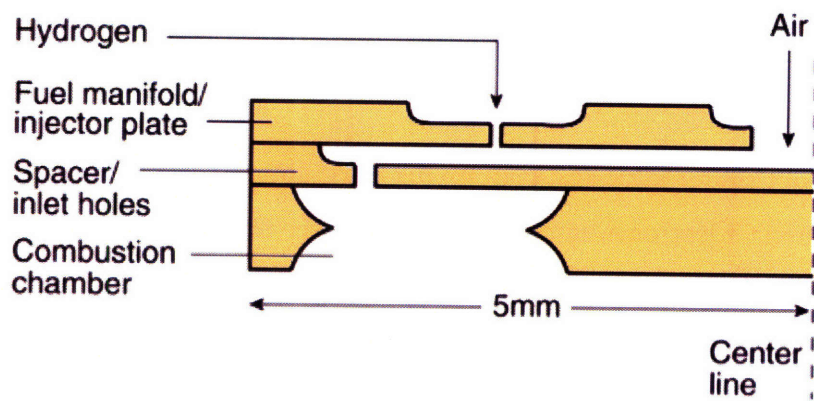
was macro-machined out of steel, and had a combustor volume of 0.13 cc. In this device, premixed hydrogen-air combustion was demonstrated, and stability limits were mapped. Computational Fluid Dynamics (CFD) was also used to better understand reacting flow phenomena at microscale. These results became the basis for the development of micro-combustors.

Three-stack silicon micro-combustor

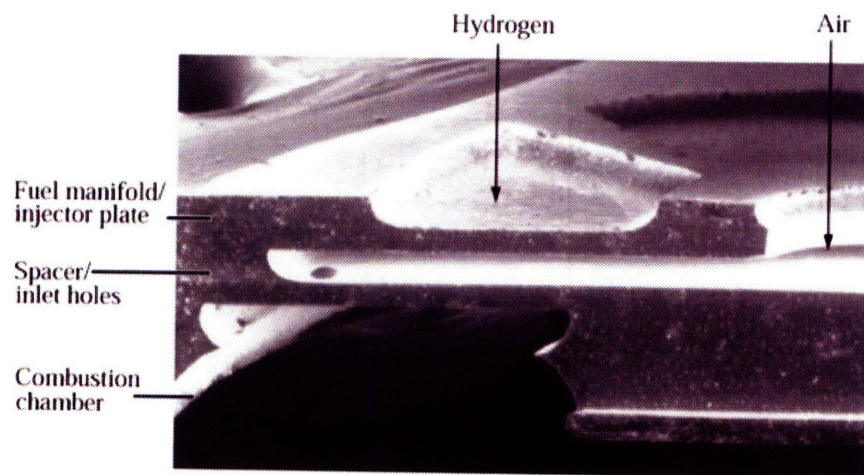
Mehra [19, 30] built a three-stack silicon micro-combustor. A cross-sectional schematic and a Scanning Electron Microscope (SEM) image of Mehra's combustor are shown in Figure 1-3. This combustor was micro-fabricated using Deep Reactive Ion Etching (DRIE), and the three wafers were permanently bonded via aligned fusion-bonding. The three-stack micro-combustor mimicked the baseline microengine geometry. The combustor volume was 0.066 cc, and it had the ability to explore fuel injected combustion. Premixed and non-premixed hydrogen-air combustion were successfully sustained in this device. For premixed combustion, exit gas temperatures were in excess of 1800 K at mass flow rates of 0.045 g/sec, corresponding to a power density near 1200 MW/m³. For non-premixed operation, the maximum temperature achieved was approximately 1700 K. The combustor efficiencies were in the 40-60% range. Extensive structural studies were also conducted in this device to assess silicon's durability in an oxidizing environment.

Six-wafer engine static structure

Mehra designed and fabricated a second micro-combustor with silicon micro-fabrication techniques [1, 19]. Figure 1-4 shows a cross-sectional schematic and SEM image of this device, which had a combustor volume of 0.191 mm³. This device replicated the MIT microengine design as conceived at the time, approximating the microengine's flow paths and thermal boundary conditions. The engine static structure did not include the rotating spool, which is complex to fabricate and not considered critical to the micro-combustor functionality. Air enters the device axially and makes a 90-degree turn into the compressor blades that have a modified blade angle, providing the flow



(a)



(b)

Figure 1-3: Schematic (a) and SEM image (b) of three-stack silicon micro-combustor [1]

more swirl to compensate for the absence of the rotor. Fuel is injected immediately downstream of the compressor. Fuel and air mix while passing through a recirculation jacket that wraps around the combustion chamber. The role of the recirculation jacket is three-fold: it provides a mixing zone, preheats the combustion reactants, and thermally isolates the combustion chamber. The fuel-air mixture then enters the combustion chamber, where the combustion reactions take place. The combustion product goes through the turbine guide vanes, which are designed to choke the flow and thus offer an ability to experiment at elevated combustor pressures.

This device was developed primarily as a hydrogen combustor, and tested with both premixed and non-premixed hydrogen. As seen in Figure 1-5, for premixed hydrogen-air combustion, an exit gas temperature in excess of 1600 K was achieved at mass flow rates of 0.11 g/sec , resulting in a power density of 1100 MW/m^3 and a combustor efficiency in excess of 80%. But the design mass flow rate of 0.36 g/sec could not be realized in this device because of flame blowout around 0.16 g/sec . Hydrocarbon fuels such as ethylene and propane were also tested in the six-wafer engine static structure, and the results are shown in Figure 1-6. When burning hydrocarbons, however, the mass flow rate capabilities were limited. Ethylene-air combustion yielded exit gas temperatures as high as 1400 K , at mass flow rates of 0.07 g/sec , corresponding to a power density of 500 MW/m^3 and a combustor efficiency of 60%. When burning propane, a maximum power density of 140 MW/m^3 was achieved at a flow rate of 0.02 g/sec with 1250 K of exit gas temperature. The corresponding overall efficiency was 55%. Combustion was blown out around 0.04 g/sec . The reduced mass flow capabilities for hydrocarbon fuels are due to their slow reaction rates; reaction time-scales of hydrocarbon fuels are approximately an order of magnitude longer than those of hydrogen.

Dual-zone micro-combustor

To broaden the operating range of the micro-combustor, Spadaccini [2, 24] designed and fabricated a dual-zone combustor. This device was similar in design to Mehra's six stack micro-combustor, but included a bypass air flow. As shown in Figure 1-7,

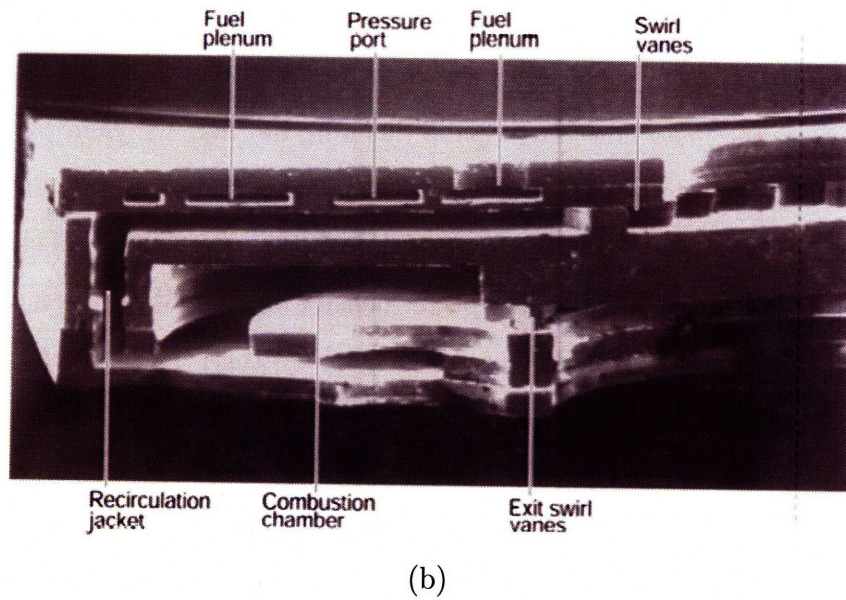
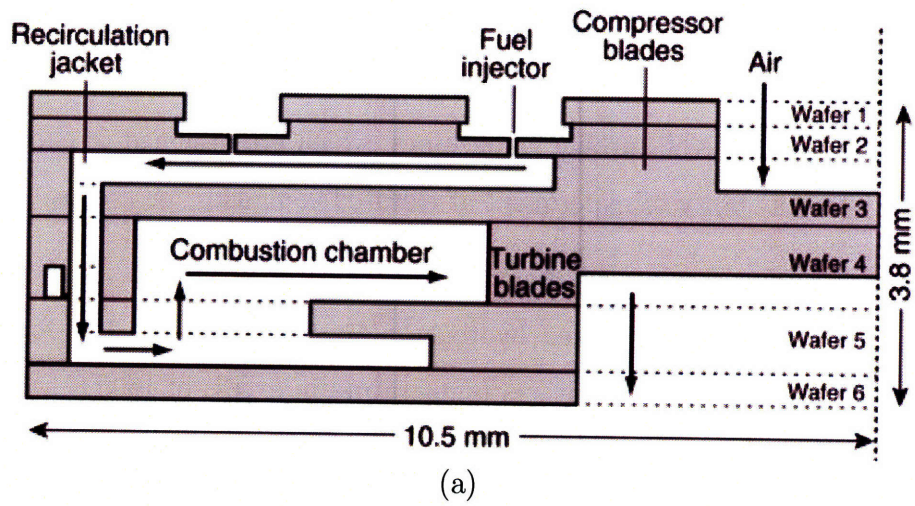
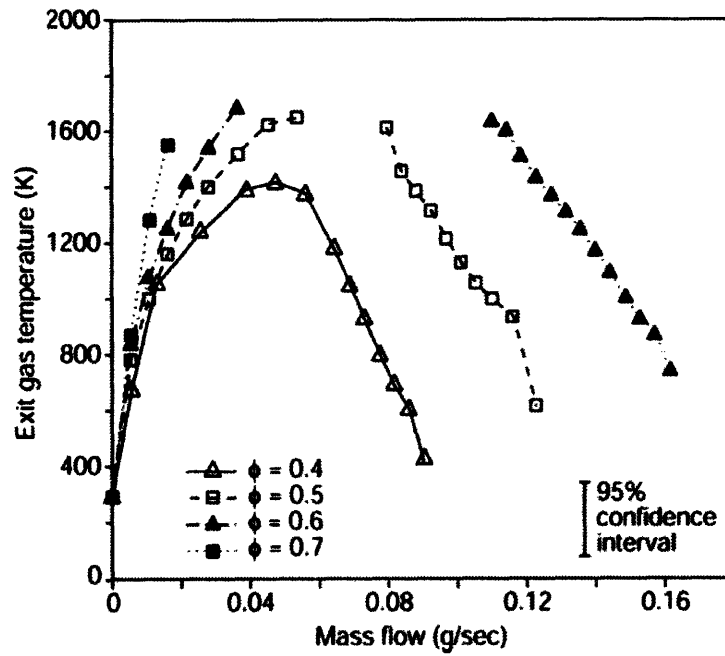
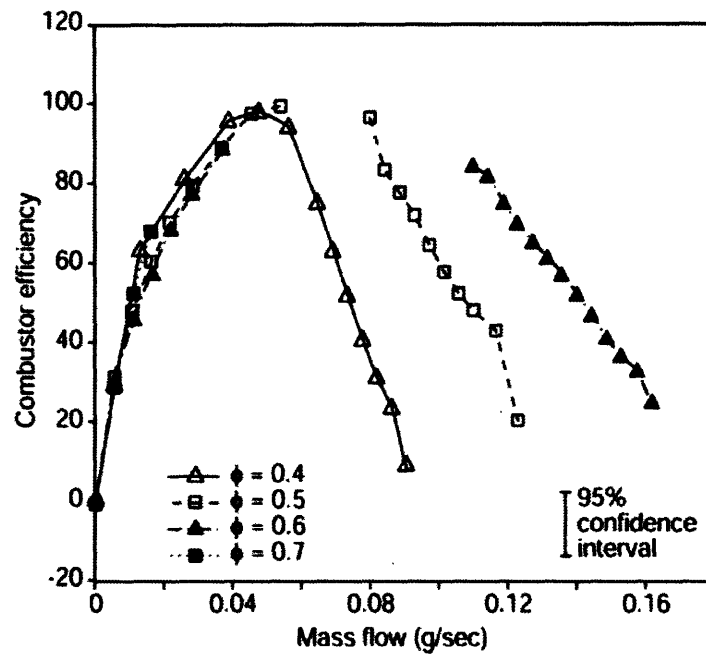


Figure 1-4: Schematic (a) and SEM image (b) of six-wafer engine static structure [1]

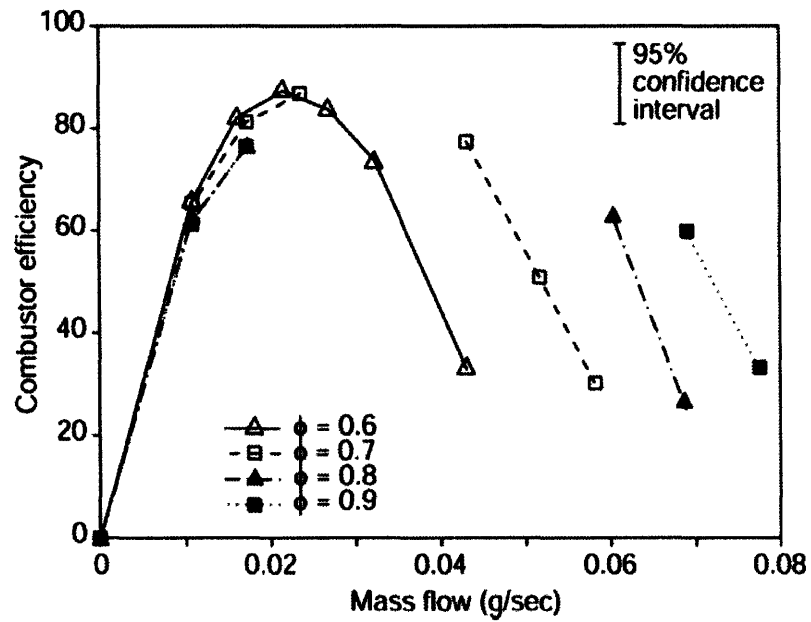


(a)

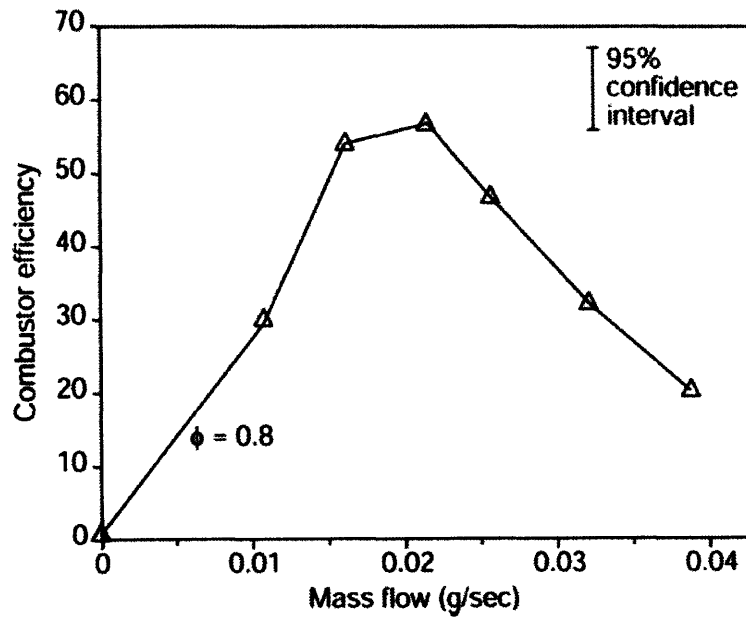


(b)

Figure 1-5: Exit gas temperature (a) and combustor efficiency (b) vs. mass flow rate for premixed hydrogen-air combustion in the six-wafer micro-combustor [1]



(a)



(b)

Figure 1-6: Combustor efficiency for six-wafer micro-combustor with ethylene-air (a) and propane-air (b) [1]

the dilution air is taken from the compressor discharge prior to fuel injection, and fed into the rear half of the combustion chamber. Thus, the combustor is bisected into a fuel-rich primary zone and a diluted secondary zone. This scheme is used in most conventional gas turbine combustors to sustain combustion at lean overall fuel-to-air ratio. Because flammability limits of hydrocarbon fuels are relatively narrow in terms of fuel-to-air ratio, the primary zone needs to be supplied with near stoichiometric fuel-air mixture to sustain combustion and produce hot combustion products. Then in the secondary zone, dilution air is mixed in to cool the combustion products to a temperature at which the turbine can safely operate.

Using hydrogen, exit gas temperatures in excess of 1600 K and efficiencies over 85% were achieved at mass flow rates of 0.12 g/sec . The maximum power density was 1400 MW/m^3 . Due to enhanced stability, the dual-zone combustor was able to sustain combustion at equivalence ratios⁶ as low as 0.2, whereas the single-zone micro-combustor was limited to 0.4. However, with hydrocarbon fuels, the dual-zone micro-combustor did not achieve the expected broader range of mass flow rates. Mass flow rates only up to 0.06 g/sec and efficiencies less than 50% were achieved with ethylene, while flow rates up to 0.035 g/sec and efficiencies less than 30% with propane. Corresponding power densities are 100 MW/m^3 and 75 MW/m^3 for ethylene and propane respectively. The reason for the limited performance is believed to be inadequate mixing; due to the nature of the device, fuel injection should happen downstream of the dilution holes. Moving the fuel injection ports downstream shortened the available mixing length by 3.2 mm . Mehra surveyed this effect of variant fuel injection locations with hydrogen in his six-wafer micro-combustor [1, 19]. He found that fuel injected operation decreases combustor efficiencies by about 5%-point compared to premixed operation. In addition, when fuel injection location is moved downstream by 3.2 mm , there was another 20%-point drop in the efficiencies. Due to longer mixing times, hydrocarbon fuels will be affected more severely. This can explain why the dual-zone micro-combustor exhibited limited performance when using

$${}^6\phi = \frac{\text{actual fuel/air ratio}}{\text{stoichiometric fuel/air ratio}}$$

hydrocarbon fuels.

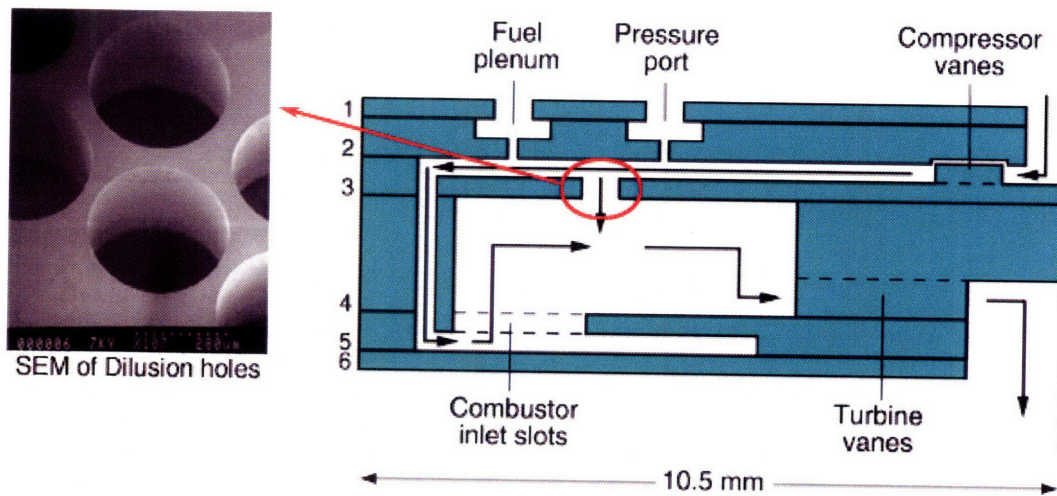


Figure 1-7: Cross-sectional diagram of the dual-zone micro-combustor [2]

Table 1.2 summarizes the results from previous work at MIT on homogeneous gas-phase micro-combustors.

Catalytic micro-combustor

Hydrogen was chosen for initial studies of micro-combustors as it is a fast burning fuel with wide flammability range. However, hydrogen is not a practical fuel for the microengine due to storage issues and low energy density (see Table 1.1). Experimental and modeling results indicated that it would not be possible for gas-phase hydrocarbon combustion to achieve the design mass flow rate of 0.36 g/sec within a combustor volume of 0.191 cc . This is due to slow reaction kinetics of hydrocarbons compared with hydrogen. To enhance the kinetics and thus to extend the mass flow

Fuel		3-stack silicon	6-wafer engine static	Dual-zone
hydrogen (H ₂)	power density	1200 MW/m ³	1100 MW/m ³	1400 MW/m ³
	efficiency	50%	70%	85%
ethylene (C ₂ H ₄)	power density		500 MW/m ³	100 MW/m ³
	efficiency		60%	38%
propane (C ₃ H ₈)	power density		140 MW/m ³	75 MW/m ³
	efficiency		55%	29%

Table 1.2: Comparison of all the gas-phase micro-combustors

rate capabilities, Spadaccini *et al.* [2, 25, 26] developed a catalytic micro-combustor. A metal high porosity foam coated with platinum was placed inside the combustion chamber. Platinum is the catalyst which promotes hydrocarbon combustion. The catalytic insert occupies the entire combustion chamber as shown in Figure 1-8. Spadaccini found that a 78% porous foam results in about a 2% total pressure loss, which is within the allowable pressure loss limit of 5%. The enhanced reaction kinetics increased mass flow rate capabilities, as expected. Stable propane-air combustion was achieved at mass flow rates in excess of 0.35 g/sec. However, exit gas temperatures were somewhat low and limited to 1100 K. The reduced exit gas temperature is believed to result from lower thermal efficiency. In the catalytic micro-combustor, heat is generated on the catalytic surfaces and transferred to the flow by convection. But considerable heat is also transferred into the surrounding silicon structure by conduction along the short paths between the hot catalytic insert and the silicon structure. This increased loss to the structure lowers the thermal efficiency of the device. Nevertheless, the increased mass flow rate results in a combustor power density of 1200 MW/m³ burning propane fuel, which is a 8.5-fold increase over the non-catalytic propane-air combustion.

Summarized in Figure 1-9 are all the versions of the micro-combustors developed at MIT including the liquid-fueled micro-combustor that is the theme of this thesis. As seen in the diagram, the dual-zone combustor and the catalytic combustor are variations of the six-wafer engine static structure. The liquid-fueled micro-combustor inherits the catalytic micro-combustor in that it catalytically burns a hydrocarbon

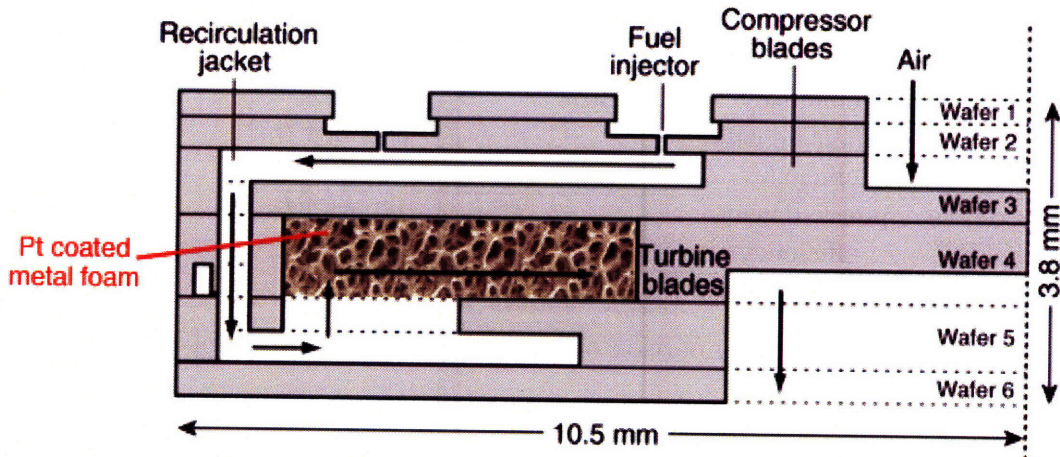


Figure 1-8: Schematic of the catalytic micro-combustor (adapted from Spadaccini [2])

fuel. But it is a unique endeavor as it has a fuel vaporizer and utilizes a liquid-fuel whose reaction mechanism is not known.

1.6.2 Other microscale combustion research

Several micro-combustors are being developed by other researchers for various applications. Yang *et al.* [31] developed a hydrogen-based combustor as a heat source for micro-thermophotovoltaics. Their stainless steel micro-combustor is a tubular type with a diameter of 3 mm and a volume of approximately 1 cc. They obtained temperatures about 1300 K along the wall at a mass flow rate of 0.1 g/sec. Combustors for micro-thermophotovoltaic systems are somewhat different from gas turbine combustors in that the former utilizes the heat flowing across the combustor walls while the latter wants to minimize that flow and maintain heat in the fluid.

Hatfield *et al.* [32] studied catalytic combustion of propane/air at much smaller scales than MIT microengines. Their combustor was 0.25×10^{-3} cc in volume, which is roughly a thousandth of the MIT micro-combustors. It was fabricated from quartz, and contained a platinum coil inside the combustor to serve as a catalyst. The device also had a counterflow heat exchanger, so that the fuel and air were premixed and preheated by combustor exhaust before entering the combustion chamber. Reaction temperatures over 1200 K were achieved at mass flow rates of 0.43×10^{-4} g/sec.

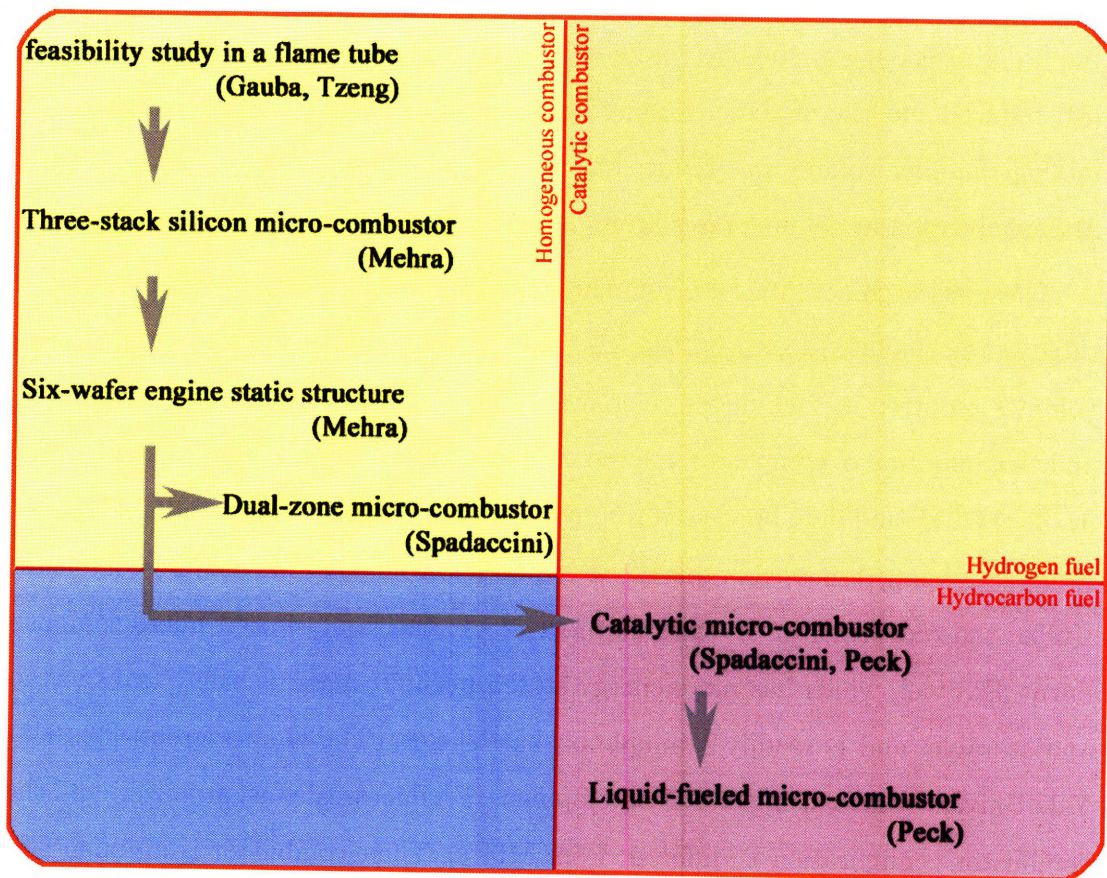


Figure 1-9: Development paths of the MIT micro-combustor

The Gomez group at Yale University is one of the research groups actively working on microscale liquid-fueled combustors. They developed a miniature fuel atomizer with multiplexed electrosprays. Kyritsis *et al.* [33] integrated the electrospray fuel atomizer into a combustion system. Their combustors, however, are open-flame type combustors as opposed to a closed-flame type of the MIT micro-combustor. So the device volumes cannot be compared directly. With catalytic JP8 combustion, they were able to achieve a catalyst temperature of 1500 K. Nominal air flow rate was on the order of 0.1 g/sec, and the volume of the mixing chamber was 15 cc. Deng *et al.* [34] reduced the size of these combustion systems utilizing MEMS technology. The mixing chamber volume was reduced to 0.22 cc. They were able to sustain catalytic JP8 combustion at air flow rates around 0.04 g/sec.

These research activities are summarized in Table 1.3. The power densities in the table were calculated based on the flow rates, combustion temperatures, and device volumes reported in each of the references. Since the device geometries are different and the definition of combustor volume used are not completely consistent, the values in the table should only be viewed to provide a rough sense of magnitude. The micro-combustor being discussed in this thesis is different from all of these micro-combustors. Unlike those of Yang *et al.* and Hatfield *et al.*, the liquid-fueled micro-combustor burns JP8 fuel, which has more energy stored per unit mass, is safely transportable and storable, and is readily available on battlefields. The Gomes group [33, 34] at Yale University is focusing on the development of a microscale fuel atomizer, and their combustor configuration is different from MIT's. Their combustor is an open-flame type, and the volume listed in Table 1.3 is that of the air and fuel mixing chamber in which JP8 fuel is vaporized and mixed with air.

1.7 Micro-combustor challenges

Reduction in length scale poses several challenges on micro-combustors relative to conventional-scale combustors. This section discusses these challenges.

Device	Fuel	Power	Volume	Power density	Reference
Yang <i>et al.</i>	hydrogen	10 W	1 cm ³	10 MW/m ³	[31]
Hatfield <i>et al.</i>	propane	1 W	0.00025 cm ³	4000 MW/m ³	[32]
Kyritsis <i>et al.</i>	JP8	100 W	15 cm ³	7 MW/m ³	[33]
Deng <i>et al.</i>	JP8	60 W	0.22 cm ³	270 MW/m ³	[34]
MIT catalytic	propane	200 W	0.19 cm ³	1100 MW/m ³	[2]

Table 1.3: Comparison of micro-combustors from other research groups

1.7.1 Short residence time for high power density devices

Combustor power density is calculated as:

$$\begin{aligned}
\text{Power density} &= \frac{\eta \dot{m}_f h_f}{V} \\
&= \frac{\eta (\dot{m}_f / \dot{m}_a) \dot{m}_a h_f}{V} \\
&= \eta (\dot{m}_f / \dot{m}_a) \rho h_f \frac{\dot{m}_a}{\rho V} \\
&= \frac{\eta (\dot{m}_f / \dot{m}_a) \rho h_f}{\tau_{res}} \tag{1.2}
\end{aligned}$$

where η is combustor efficiency, \dot{m}_f and \dot{m}_a fuel flow rate and air flow rate respectively, h_f heating value of fuel, V combustor volume, ρ fluid density in the combustion chamber, and τ_{res} flow residence time. In general, power density is inversely proportional to flow residence time; as we desire high power densities, flow residence times in the combustion chamber become inevitably short. However, chemical reaction time is not a function of size, but only temperature, pressure, and composition of reactants. As we increase flow rates through the combustor, flow residence times decrease whereas chemical reaction times do not vary significantly. Residence times approach reaction times, and this eventually prevents complete combustion.

1.7.2 Large heat loss

Micro-combustors tend to have low thermal efficiencies. One of the reasons for this is the large heat transfer coefficient at small scale. Since the dependence of Nusselt number on Reynolds number differs between the flow regimes of a conventional

combustor and a micro-combustor, the following three flow conditions are compared:

1. *Laminar, fully developed*

$$Nu_D = \text{const.} \quad (1.3)$$

$$h \equiv \frac{k Nu_D}{D_h} \propto D_h^{-1} \quad (1.4)$$

If the length scale is reduced by a hundredth, the convective heat transfer coefficient increases by a factor of 100 times.

2. *Laminar, entrance region* (Sieder and Tate [35])

$$Nu_D = 1.86 \left(\frac{Re_D Pr}{L/D} \right)^{1/3} \left(\frac{\mu}{\mu_s} \right)^{0.14} \propto Re_D^{1/3} \quad (1.5)$$

(when $L \propto D$)

$$h \propto D_h^{-2/3} \quad (1.6)$$

For a hundredth the length scale, the heat transfer coefficient increases by a 22-fold.

3. *Turbulent* (Dittus-Boelter equation [36])

$$Nu_D = 0.023 Re_D^{4/5} Pr^n \propto Re_D^{4/5} \quad (1.7)$$

$$h \propto D_h^{-1/5} \quad (1.8)$$

If the length scale is reduced by a hundredth, the convective heat transfer coefficient increases by a factor of 2.5 times.

In all flow regimes, the convective heat transfer coefficient becomes larger as the length scale is reduced, so the device loses more heat per unit area. Particularly, the flow in the micro-combustors is likely to be laminar that is influenced by the scale the most.

Another reason for the micro-combustor's large heat loss is attributed to the low Biot number. The Biot number is the ratio of conductive heat resistance to the convective resistance:

$$Bi \equiv \frac{hL}{k_s} \quad (1.9)$$

where h is the convective heat transfer coefficient, L the length scale, and k_s the thermal conductivity of the structure. By the definition of the Nusselt number,

$$hL = k_f Nu_L \quad (1.10)$$

where k_f is the thermal conductivity of the fluid. Hence,

$$Bi = \frac{k_f}{k_s} Nu_L \quad (1.11)$$

As seen in Equations (1.5) and (1.7), Nusselt number decreases with Reynolds number in general. Therefore, for a low Reynolds number flow as in the micro-combustor, the Biot number becomes small. Furthermore, thermal conductivity of silicon is about 150 W/mK at the room temperature, whereas that of steel is only about 50 W/mK . This high thermal conductivity reduces the Biot number even more, so it becomes approximately 0.01 for typical microengine settings. The low Biot numbers suggest that the microscale silicon structure cannot sustain a temperature gradient. The structure is nearly isothermal, so the inner wall is at relatively low temperatures, and the outer wall at high temperatures (as opposed to a large difference between the inner and the outer walls for a structure with a high Biot number). The device loses more heat through the walls. A designer of a micro-combustor must carefully address these heat transfer issues.

1.7.3 Materials and fabrication constraints

The microengine operates in nearly isothermal conditions due to low Biot numbers. As a consequence, the rotating spool is at temperatures as high as the combustor. Because these rotating components are under centrifugal load, the structure should

be kept below 900 K at which silicon starts to creep [37]. Lacking an active cooling scheme on the rotating spool, the maximum operating temperature of the combustor is limited by the material constraints. This exacerbates the residence time issue as the low temperatures slow down the chemical reactions and demand longer flow residence times.

1.7.4 Challenges specific to the use of liquid-fuels

Liquid-fueled micro-combustors inherit the issues of gaseous-fueled micro-combustors. In addition, there are challenges specific to the use of liquid-fuels consisting of heavy hydrocarbons.

Longer combustion times A combustion time-scale consists of vaporization, mixing, diffusion, and reaction times:

$$\tau_{\text{combustion}} = \tau_{\text{vaporization}} + \tau_{\text{mixing}} + \tau_{\text{diffusion}} + \tau_{\text{reaction}} \quad (1.12)$$

It is known that the gas-phase reaction time is not noticeably different between light and heavy hydrocarbons. Levebvre *et al.* [38] published an experimental report on ignition delays of various fuels⁷. According to the report, the spontaneous ignition delay of premixed propane-air combustion is approximately 50 ms at the stoichiometric equivalence ratio and atmospheric pressure. With the same conditions, it is about 30 ms for prevaporized and premixed JetA, which is a kerosene-based jet fuel similar to JP8. The reason for this is because heavy hydrocarbon molecules are less stable, so they tend to crack quickly into light hydrocarbons that can react. Although detailed chemistry of catalytic JP8 combustion is not known, we may assume that there will not be a big difference in the catalytic reaction time-scales between propane and JP8. However, the diffusion time-scale, which is approximately one order of magnitude longer than the reaction time-scale in the micro-combustor environment, is longer for JP8

⁷These experiments were conducted in a simple flame tube, which is different from the microengine geometry. Therefore, only the relative numbers are meaningful.

fuel than for gaseous fuels such as propane because the diffusion rate of JP8 is around one half that of propane. As a result, for a prevaporized and pre-mixed case, catalytic JP8 combustion will take longer than catalytic propane combustion. The combustor volume needs to be increased accordingly.

The mixing time, which is usually longer than the diffusion time and the reaction time⁸, is also longer for heavy hydrocarbons due to their slower diffusion rates. In addition, heavy hydrocarbon fuels that are in the liquid-phase at standard temperatures and pressures need to be converted to the vapor-phase prior to the chemical reactions. Following Kuo [40], the vaporization time of a fuel droplet with a diameter D_0 is given by

$$\tau_{vaporization} = \frac{\rho_l D_0^2}{8\rho_v \alpha_v \ln(1+B)} \quad (1.13)$$

where ρ_l and ρ_v are the densities of the liquid-phase and the vapor-phase respectively, α_v the thermal diffusivity of the vapor, and B the transfer coefficient. Using this formula, a fuel droplet with a diameter of $20 \mu m$ takes about $5 ms$ to be vaporized at an ambient temperature of $700 K$.

Considering these aspects, a strategy for a liquid-fuel burning micro-combustor was chosen; the fuel would be prevaporized and mixed with air prior to entering the combustion chamber in order to minimize the required volume of the combustion chamber. To further reduce the combustion time-scale, catalytic combustion would be adopted.

Fuel vaporizer A fuel atomizer or a vaporizer is required to prevaporize the fuel. If an atomizer was to be used, it would have to be able to generate fuel droplets as small as $20 \mu m$ in diameter, so that the droplets could be vaporized within a few milliseconds. Atomizing a liquid-fuel into such small droplets is not trivial, especially with constraints on the fabrication techniques and the size.

⁸According to Dodds and Bahr [39], of the typical $5-8 ms$ combustor residence time in a conventional gas turbine, approximately 60% ($3-5 ms$) is devoted to fuel vaporization and mixing, and about 40% ($2-3 ms$) to mixing of dilution air. The chemical reaction time is fairly negligible.

Another option is to vaporize the fuel on a hot surface. Due to the low Biot number, the microengine is almost isothermal, and hot surfaces are readily available. We may design a component, enclosed in the engine structure, with enough surface area to provide the fuel with the required heat for vaporization. This type of vaporizer has some advantages over others. First, it does not need external power to operate. By vaporizing the fuel on the hot surfaces, several watts of waste heat could be reused, enhancing overall efficiencies. The fuel atomizer developed by the Gomez group [33, 34] operates across a high voltage. The voltage has to be supplied by an external source, or be fed back from the power output of the engine, which will compromise the efficiencies. Second, a vaporizer with hot surfaces can be realized with simpler geometries than atomizers.

Fuel decomposition (coking) Liquid hydrocarbon fuels, especially JP8, are known to easily decompose at high temperatures and leave carbon residues. This could be responsible for fouling or coking of the engine system. The phenomenon might become significant on the fuel-vaporizing surfaces, the fuel injection holes, and the catalytic insert. The residual carbons may clog the fluid paths or deteriorate the catalyst. Because the coking is heavily dependent on the temperature, the surface roughness, and the geometry of the system, it is difficult to theoretically predict its characteristics. It should be assessed experimentally during the course of the liquid-fueled micro-combustor research.

1.8 Organization of the thesis

This thesis consists of three main areas of development for a liquid-fueled micro-combustor: design, fabrication, and experiment. Each aspect of the research is presented in the subsequent chapters.

The introduction is followed by Chapter 2, which provides information regarding the experimental apparatus design. All the design models developed are explained in this chapter. Detailed design of each part of the device is presented. This chapter also

offer general design guidelines that can be referred to in designing other hydrocarbon micro-combustors of a similar size.

Chapter 3 reports how the liquid-fueled micro-combustor was fabricated, and how the experimental setup was developed. Detailed steps of micro-fabrication are included.

Chapter 4 discusses the experimental results from the liquid-fueled micro-combustor. Experimental data acquired from the device are presented, and interpretations thereof are also provided. Based on the experiments, a non-dimensional operating map was generated. Design case studies are presented using the non-dimensional operating map.

Finally, the main body of the thesis is concluded in Chapter 5. The research is summarized and areas of future work are suggested.

Appendices A and B contain the photomask drawings for the micro-fabrication and the mechanical drawings for the ultrasonically machined parts, respectively. Appendix C discusses a Monte-Carlo simulation conducted on the fuel vaporizer design model. Appendix D introduces the heat transfer models that were used to estimate heat loss from the device. Uncertainties in the experimental measurements and their derivatives are reported in Appendix E.

Chapter 2

Experimental Apparatus Design

As discussed in Section 1.7.4, designing a JP8 combustor at this small length scale is challenging because few data are available to reference in the design process. Therefore, several design models had to be developed and used in determining the geometries and dimensions of each component of the experimental test rig. This chapter presents how the test rig was designed, and explains the details of each design model. The design models developed for the liquid-fueled micro-combustor can be more generally referenced when designing similar micro-combustors in the future.

To design an experimental apparatus, its design requirements must be carefully specified. The following is the key requirements for the testbed:

- It must be able to explore the feasibility of using JP8 fuel in the microengine settings.
- It must serve as a platform to study flow physics and combustion chemistry of the liquid-fueled combustor at microscale.
- It must have a geometry that would be compatible with the microengine system.

In order for the experimental test rig to be compatible for integration with the microengine, it must have a geometry and a flow path that are similar to the microengine. Hence, the combustion chamber will be a shape of an annulus, allowing the flow to enter from the outer diameter, travel radially toward the inner diameter, and finally

exit through the inner diameter. Other operating parameters should also follow those of the microengine. Table 2.1 specifies the operating conditions of the microengine and thus, the liquid-fueled micro-combustor.

Parameter	Value
total mass flow rate	0.3 g/sec
fuel flow rate	0.04 g/sec
combustor discharge temperature	1300 K
combustor pressure	2 atm

Table 2.1: Operational specifications of the liquid-fueled micro-combustor

2.1 Material selection

The MIT microengine is fabricated out of silicon. Silicon was chosen for several reasons:

- To leverage existing fabrication technology developed for the integrated circuit industry, allowing for batch fabrication (making several devices in parallel)
- Fabrication tools developed for silicon allow for precision control of feature size and etch depth

The micro-combustor must be compatible with the MIT microengine, so silicon or other MEMS-compatible materials should be used eventually. The goal of the present project, however, is to explore the concept of liquid-fuel combustion at microscale. To allow more flexibility in the device fabrication and experiments, it was decided that materials other than silicon would be used for some parts. Complex components with small features were fabricated out of silicon using the micro-fabrication techniques. Less intricate parts such as the combustion chamber were made out of sapphire. Sapphire is an excellent material for the micro-combustor for two reasons: it is functional at high temperatures up to 2100 K [41], and offers visual access into the combustion chamber. However, sapphire has some drawbacks as well. First, its

thermal conductivity differs from that of silicon¹, which makes it difficult for the test apparatus to exactly replicate the thermal boundary conditions of the microengine. In addition, because sapphire’s thermal expansion coefficient does not match silicon², it is not eligible for anodic bonding to silicon. To address this limitation, the device stack was designed to be mechanically clamped instead of permanently bonded as it was for previous silicon micro-combustors.

Another material used besides silicon was Hoya’s proprietary SD-2 glass. This specialty glass is designed for anodic bonding with silicon. An extended packaging block on top of the fuel vaporizer was made with SD-2 glass as it can be bonded to silicon while providing a visual window through the vaporizer. Section 2.5 will discuss this in more detail.

2.2 Combustor volume

The combustor volume is chosen so that flow residence times in the combustor are longer than reaction time-scales, i.e. the Damköhler number larger than unity. Selecting an adequate combustor volume is particularly crucial when designing a micro-combustor because a high power density is desired, i.e. maximum power output should be achieved for a given combustor volume. The combustor needs to be sized as small as possible, but still be sufficiently large so that the residence time of the fuel-air mixture is longer than the reaction time. As stated in Section 1.7.4, the fuel will be vaporized and mixed with air prior to entering the combustion chamber. Only the reaction time-scales determine the combustor volume. Therefore, it would be most useful if one can estimate the reaction time-scales of catalytic JP8 combustion. To do it accurately, we need to understand the reaction kinetics of catalytic combustion of such hydrocarbons as n-octane(C8), n-nonane(C9), n-decane(C10), n-undecane(C11), n-dodecane(C12), and n-tridecane(C13) as well as various aromatic species. However, detailed kinetics data are not currently available for these chemical reactions. De-

¹ $k_{silicon} = 150 \text{ W/mK}$ vs. $k_{sapphire} = 40 \text{ W/mK}$ [41]

² $\alpha_{silicon} = 3.6 \times 10^{-6} \text{ K}^{-1}$ vs. $\alpha_{sapphire} = 7.3 - 8.1 \times 10^{-6} \text{ K}^{-1}$ [42]

tailed surface reaction mechanisms for hydrocarbons heavier than ethane are yet to be studied. For this reason, it was necessary to develop a simplified methodology to estimate the reaction time-scales of catalytic JP8 combustion. Developing a comprehensive surface reaction mechanism for each species in JP8 requires intensive efforts and resources, and was considered beyond the scope of the micro-combustor research described here. Thus, we pursued a simplified design model that enabled us to estimate the reaction time-scales of JP8 combustion over platinum catalyst.

2.2.1 Overview of the model

The model was constructed under the following assumptions:

- The combustor is a simple tube, and the fluid flow inside the combustor is modeled as a steady, compressible, viscous flow along a circular tube with a constant cross-section. The inner wall of the tube is coated with catalyst, and the chemical reactions occur only on the walls. Thus, gas-phase combustion is ignored.
- It is a constant-pressure combustion process like typical gas turbine combustors.
- The fuel is prevaporized and uniformly mixed with air before entering the combustion chamber.
- The catalytic combustion of hydrocarbon fuels is a diffusion-controlled process; the fuel molecules diffuse onto the catalytic surfaces slowly relative to the times required for the fuel molecules to be consumed by chemical reactions. Moreover, the diffusion of oxygen is approximately 70 times faster than that of the fuel. So the diffusion rate of the fuel molecules dictates the overall reaction rate. Spadaccini [2, 26] found that diffusion-based Damköhler number³ is in the range of 5 to 20, which indicates that the combustion is mass transfer controlled [43]. Under these conditions, the concentration of the fuel species on the catalytic

³ $Da = \frac{\tau_{dif}}{\tau_{reac}}$

surfaces is less than 5% of the mean bulk value. But to further simplify the problem, the surface concentration is assumed to be zero.

- JP8 is approximated as $C_nH_{1.8n}$ with $n = 13$. Average molar weight of JP8 is about 179 [44].
- Fluid properties in the bulk stream such as the density and the specific heat were represented by those of air since the stoichiometric mixture has only 7% of fuel by weight.
- There is no heat transfer to the wall (adiabatic walls).

With these assumptions, the reacting flow problem becomes a mass transfer problem. The mass transfer equations can be applied without modeling the detailed reaction kinetics, which is a considerable advantage. Under the assumptions listed above, the fuel concentration forms a profile that becomes zero on the wall and peaks at the center of the tube. This concentration gradient causes the fuel molecules to diffuse onto the catalytic walls. And because the reaction rates are much faster than the diffusion rates, the fuel molecules are immediately consumed by chemical reactions. Using a mass transfer equation, it can be calculated how much fuel is transported onto the wall via diffusion and thus converted. This fuel conversion can be traced along the tube, and a lengthwise profile of the fuel concentration can be obtained. Then, the axial location where the fuel concentration becomes 10% of the initial concentration can be found, and the time for the flow to reach this location can also be determined. This time is defined as the diffusion time-scale. Eventually, the volume of the combustion chamber will be determined so that the flow residence time⁴ in the combustion chamber is longer than the diffusion time; in other words, the Peclet number larger than unity:

$$Pe \equiv \frac{\tau_{residence}}{\tau_{diffusion}} > 1 \quad (2.1)$$

⁴ $\tau_{residence} = \frac{\rho V}{\dot{m}}$, ρ being the average density in the combustion chamber with a volume of V . The validity of using an average density was demonstrated by Mehra [19].

Due to the exothermic reactions, the fluid temperature increases moving downstream. The temperature changes, in turn, have an impact on the diffusion rates. Thus, there is a coupling between the fuel concentration and the temperature, so the governing equations of the model become a set of coupled equations.

2.2.2 Governing equations

Let us take the control volume just inside the tube as shown in Figure 2-1. The fuel molecules are transported axially in and out of the control volume via the bulk fluid flow, and some of them diffuse out of the control volume radially as well (diffusion in the axial direction is ignored because the concentration gradient in the axial direction is much smaller than in the radial direction).

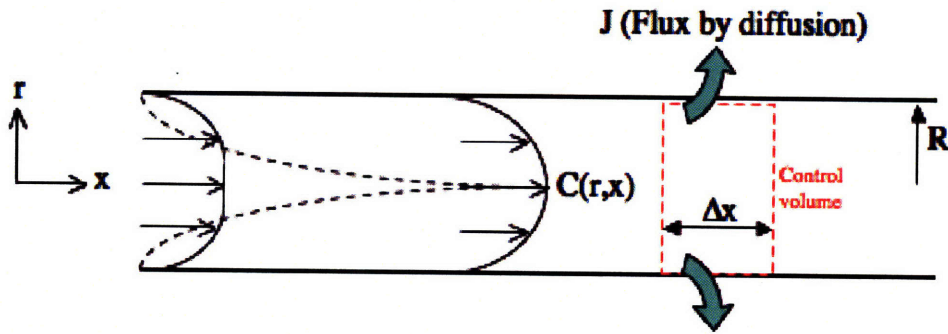


Figure 2-1: Definition of the control volume for the combustor volume design model

Over the control volume, the fuel concentration may be balanced as:

$$\int_0^R u(r, x)C(r, x)2\pi r dr - \int_0^R u(r, x + \Delta x)C(r, x + \Delta x)2\pi r dr = J \cdot 2\pi R \cdot \Delta x \quad (2.2)$$

where

R : radius of the tube [m]

$u(r, x)$: local velocity of fluid [m/sec]

$C(r, x)$: local concentration of fuel [mol/m³]

J : mole flux of the fuel species into wall [mol/m²sec]

A bulk concentration is defined as:

$$C_b(x) : \frac{\int_0^R u(r, x)C(r, x)2\pi r dr}{U(x)\pi R^2} \quad [mol/m^3] \quad (2.3)$$

where $U(x)$ is the flow velocity averaged across the cross-section at the axial location x . By plugging Equation (2.3) in Equation (2.2):

$$\frac{U(x + \Delta x)C_b(x + \Delta x) - U(x)C_b(x)}{\Delta x} = -\frac{2J}{R} \quad (2.4)$$

By taking $\Delta x \rightarrow 0$,

$$\frac{d(UC_b)}{dx} = -\frac{2J}{R} \quad (2.5)$$

Because we are solving for the time for the flow to reach a certain location, it is more convenient to write the equation in terms of the time variable, t , using the following correlation⁵:

$$\frac{d(UC_b)}{dx} = \frac{1}{U} \frac{d(UC_b)}{dt} \quad (2.6)$$

Substituting Equation (2.6) into Equation (2.5),

$$\frac{d(UC_b)}{dt} = -\frac{2J}{R}U \quad (2.7)$$

According to Mills [45], the mole flux, J , can be expressed as the following:

$$J = h_m C_b = \frac{Sh_D D_{ab}}{2R} C_b \quad (2.8)$$

Here, h_m is the mass transfer coefficient, which can be expressed as in Equation (2.8) by the analogy between heat transfer and mass transfer. The Sherwood number,

⁵From

$$\frac{d(UC_b)}{dt} = \frac{\partial(UC_b)}{\partial t} + (\vec{v} \cdot \nabla)(UC_b)$$

Because C_b was assumed to be steady and to vary only in the x -direction,

$$\frac{d(UC_b)}{dt} = U \frac{d(UC_b)}{dx}$$

Sh_D , is analogous to the Nusselt number in heat transfer, and the molecular diffusion coefficient, D_{ab} , can be given by the Fuller correlation [43]:

$$D_{ab} = \frac{1.013 \times 10^{-2} T^{1.75} \sqrt{1/M_a + 1/M_b}}{P (v_a^{1/3} + v_b^{1/3})^2} [m^2/s] \quad (2.9)$$

where

T : temperature [K]

P : pressure [Pa]

M_a, M_b : molecular weight of the species a and b

v_a, v_b : diffusion volume of the species a and b

Combining Equations (2.7) and (2.8),

$$\frac{d(UC_b)}{dt} = -\frac{Sh_D D_{ab}}{R^2} (UC_b) \quad (2.10)$$

And,

$$U(t) = \frac{\dot{m}}{\rho(t) \pi R^2} \propto T(t) \quad (2.11)$$

Thus, Equation (2.10) becomes:

$$\frac{d(TC_b)}{dt} = -\frac{Sh_D D_{ab}}{R^2} (TC_b) \quad (2.12)$$

To find a correlation between the temperature and the concentration, power balance in and out of the control volume can be written as:

$$(\pi R^2) \rho U \Delta(C_p T) = -(\pi R^2) h_f \Delta(UC_b) \quad (2.13)$$

Hence,

$$\frac{d(C_p T)}{dt} = -\frac{h_f}{\rho U} \frac{d(UC_b)}{dt} \quad (2.14)$$

$$T \frac{dC_p}{dT} \frac{dT}{dt} + C_p \frac{dT}{dt} = - \frac{h_f}{\rho U} \frac{d(UC_b)}{dt} \quad (2.15)$$

Using Equation (2.11),

$$T \frac{dC_p}{dT} \frac{dT}{dt} + C_p \frac{dT}{dt} = - \frac{h_f}{\rho T} \frac{d(TC_b)}{dt} \quad (2.16)$$

Finally,

$$\frac{dT}{dt} = \frac{-h_f/\rho}{C_p T + \frac{dC_p}{dT} T^2} \frac{d(TC_b)}{dt} \quad (2.17)$$

where

h_f : lower heating value of the fuel [J/mol]

ρ : local density (function of temperature and pressure) [kg/m^3]

C_p : constant pressure specific heat of air (function of temperature) [J/kgK]

The constant pressure specific heat of air is given by:

$$C_{p,N_2} = 39.060 - 512.79 \left(\frac{T}{100}\right)^{-1.5} + 1072.7 \left(\frac{T}{100}\right)^{-2} - 820.40 \left(\frac{T}{100}\right)^{-3} \quad (2.18)$$

$$C_{p,O_2} = 37.432 + 0.020102 \left(\frac{T}{100}\right)^{1.5} - 178.57 \left(\frac{T}{100}\right)^{-1.5} + 236.88 \left(\frac{T}{100}\right)^{-2} \quad (2.19)$$

$$\begin{aligned} C_p &= 0.79 C_{p,N_2} + 0.21 C_{p,O_2} \quad [kJ/kmolK] \\ &= (0.79 C_{p,N_2} + 0.21 C_{p,O_2}) \frac{1000}{28.97} \quad [J/kgK] \end{aligned} \quad (2.20)$$

This correlation is known to be good within a temperature range 300 to 3500 K.

Equations (2.12) and (2.17) constitute a set of coupled differential equations:

$$\frac{d(TC_b)}{dt} = -\frac{Sh_D D_{ab}}{R^2}(TC_b)$$

$$\frac{dT}{dt} = \frac{-h_f/\rho}{C_p T + \frac{dC_p}{dT} T^2} \frac{d(TC_b)}{dt}$$

Here, D_{ab} , C_p , and ρ should be evaluated for the corresponding temperatures using proper correlations such as Equation (2.9). In this set of equations, R and P are input parameters that a designer can set, and M_a , M_b , v_a , v_b , and h_f are the properties of fuel or air. Due to small scale in the micro-combustor, the flow is laminar and fully developed, so the Sherwood number, Sh_D , was chosen to be 3.66.

2.2.3 Results

This equation set was solved with appropriate initial conditions. Because the equations are coupled non-linear differential equations, solutions were obtained numerically. The fluid properties listed in Table 2.2 were used when solving the set of equations. Solutions for various conditions and design parameters are shown in Figures 2-2 through 2-4. A higher equivalence ratio results in a shorter diffusion time (Figure 2-2) because the diffusion rate is proportional to the concentration. Since the concentration gradient becomes larger when the tube diameter is smaller, increasing the diffusion rate, the diffusion time becomes shorter for a smaller tube diameter (Figure 2-3). And because the diffusion coefficient is inversely proportional to the pressure (Equation (2.9)), meaning that a higher pressure hinders diffusion, the diffusion time is shorter for a lower combustor pressure⁶ (Figure 2-4). This result is distinct from the reaction time-scale of gas-phase combustion, which tends to become shorter as the pressure increases.

⁶Due to the slow diffusion at high pressures, catalytic combustion becomes slower than gas-phase combustion above a certain pressure. For large-scale gas turbine systems with a pressure ratio over 10, a catalytic combustor is likely to be larger than a gas-phase combustor. In those cases, the main reason for catalytic combustion is to reduce NO_x emission, not to reduce the combustion time. [43]

For most cases, the solutions indicate that the fuel concentration falls below 10% of the initial concentration in less than 2.5 *ms*, so the flow residence time must be longer than this to make the Peclet number larger than one. For the design flow rate of 0.3 *g/sec* and the pressure of 2 *atm*, the corresponding combustor volume is 1400 *mm*³.

Nomenclature	Property	Value	Reference
Sh_D	Sherwood number	3.66	[45]
M_a	molecular weight of air	28.96 <i>g/mol</i>	[43]
M_b	molecular weight of JP8	179 <i>g/mol</i>	[43]
v_a	diffusion volume of air	20.1	[43]
v_b	diffusion volume of JP8	260.83	[43]
h_f	heating value of JP8	7.73×10^6 <i>J/mol</i>	[44]

Table 2.2: Fluid properties used for the solutions

Apart from the operating conditions and design parameters studied in Figures 2-2 through 2-4, the results depend on the properties listed in Table 2.2. As a consequence, uncertainties in these fluid properties may affect the result of the model. Table 2.3 summarizes the dependency of the model on those parameters. The baseline case for this survey is $\phi = 1.0$, $P = 2$ *atm*, and $D = 700$ μ *m*. The result shows that even with parameter variances as large as $\pm 30\%$, the reaction time-scales estimated by the model were within 2 *ms* for most cases.

Parameter	Reaction time-scales [<i>ms</i>] due to parameter variances by			
	-30%	-10%	+10%	+30%
Sh_D	2.18 (+41.6%)	1.72 (+11.7%)	1.37 (-11.0%)	1.18 (-23.4%)
M_a	1.28 (-16.9%)	1.45 (-5.8%)	1.63 (+5.8%)	1.72 (+11.7%)
M_b	1.46 (-5.2%)	1.54 (0.0%)	1.54 (0.0%)	1.55 (+0.6%)
v_a	1.45 (-5.8%)	1.46 (-5.2%)	1.55 (+0.6%)	1.63 (+5.8%)
v_b	1.28 (-16.9%)	1.45 (-5.8%)	1.63 (+5.8%)	1.73 (+12.3%)
h_f	2.18 (+41.6%)	1.72 (+11.7%)	1.37 (-11.0%)	1.18 (-23.4%)
C_p	1.09 (-29.2%)	1.36 (-11.7%)	1.64 (+6.5%)	1.95 (+26.6%)
ρ	1.09 (-29.2%)	1.36 (-11.7%)	1.64 (+6.5%)	1.95 (+26.6%)

Table 2.3: Variances in the estimated reaction times [*ms*] (and deviations from the baseline value, 1.54 *ms*) due to uncertainties in the fluid properties

Based on a combustor volume of 1400 mm^3 , the detailed dimensions were decided. In order to replicate the flow geometry of the microengine, the combustor is the shape of an annulus with the outer radius and the inner radius of 16.7 mm and 6.5 mm , respectively. The values were rather set by the fuel vaporizer design, which will be discussed in the next section. The height of the chamber must be 2 mm to make the combustor volume 1400 mm^3 . The resulting design is shown in Figure 2-5.

The combustion chamber layer has three thermocouple holes for temperature measurements. Two thermocouples are buried in the sapphire structure and measure structural temperatures near the inlet and the exit. Another thermocouple is exposed to the exhaust gas at the exit of the combustor and measures the exit gas temperature. The locations of the thermocouples are shown in Figure 2-6.

2.2.4 Summary of the combustor volume model

A reduced-order design model was developed to estimate the time-scale of catalytic JP8 combustion. The model can be used for the catalytic combustion of any slow-diffusing fuel if the diffusion time-scale is at least ten times longer than the reaction time-scale. Under this condition, the reaction time is negligibly short, and the combustion time can be approximated as the diffusion time. This approximation eliminates the need for a surface chemistry kinetics model which is not available for JP8 combustion. Based on the model results, the combustor volume was designed to be 1400 mm^3 , which is about seven times larger than the previous silicon micro-combustor burning gaseous fuels. Considering that the catalytic propane combustor had chemical efficiencies about 30%, and that the diffusion rate of JP8 is about half that of propane, a seven-fold increase in volume seems reasonable.

2.3 Fuel vaporizer

In conventional gas turbine engines, fuel is usually injected directly into the combustion chamber in the form of droplets. Then, the droplets evaporate as the combustion reactions take place. For the micro-combustor applications, however, the fuel needs to

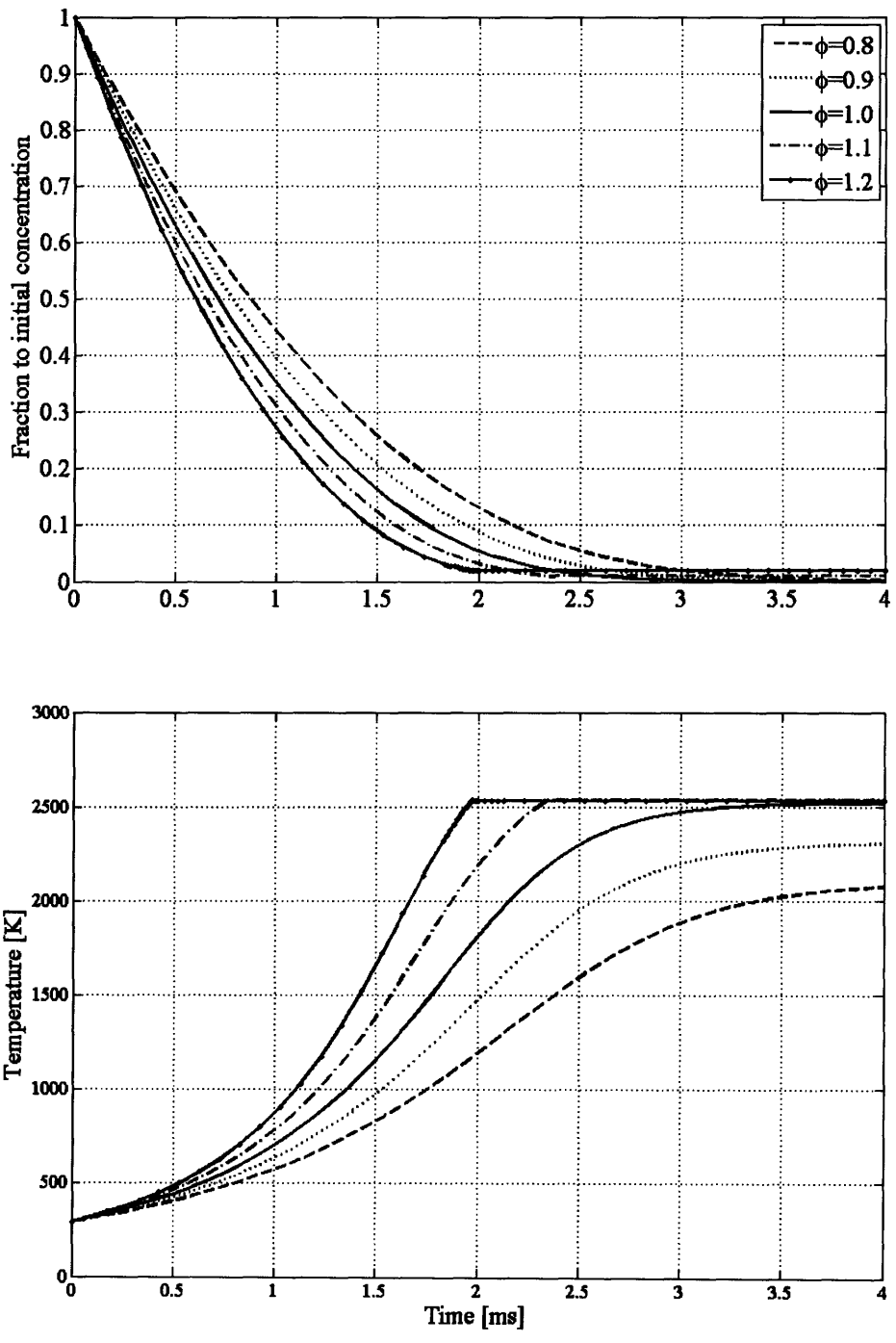


Figure 2-2: Results of the catalytic combustion model for various equivalence ratios (tube diameter = $700 \mu m$, $P = 2.0 atm$)

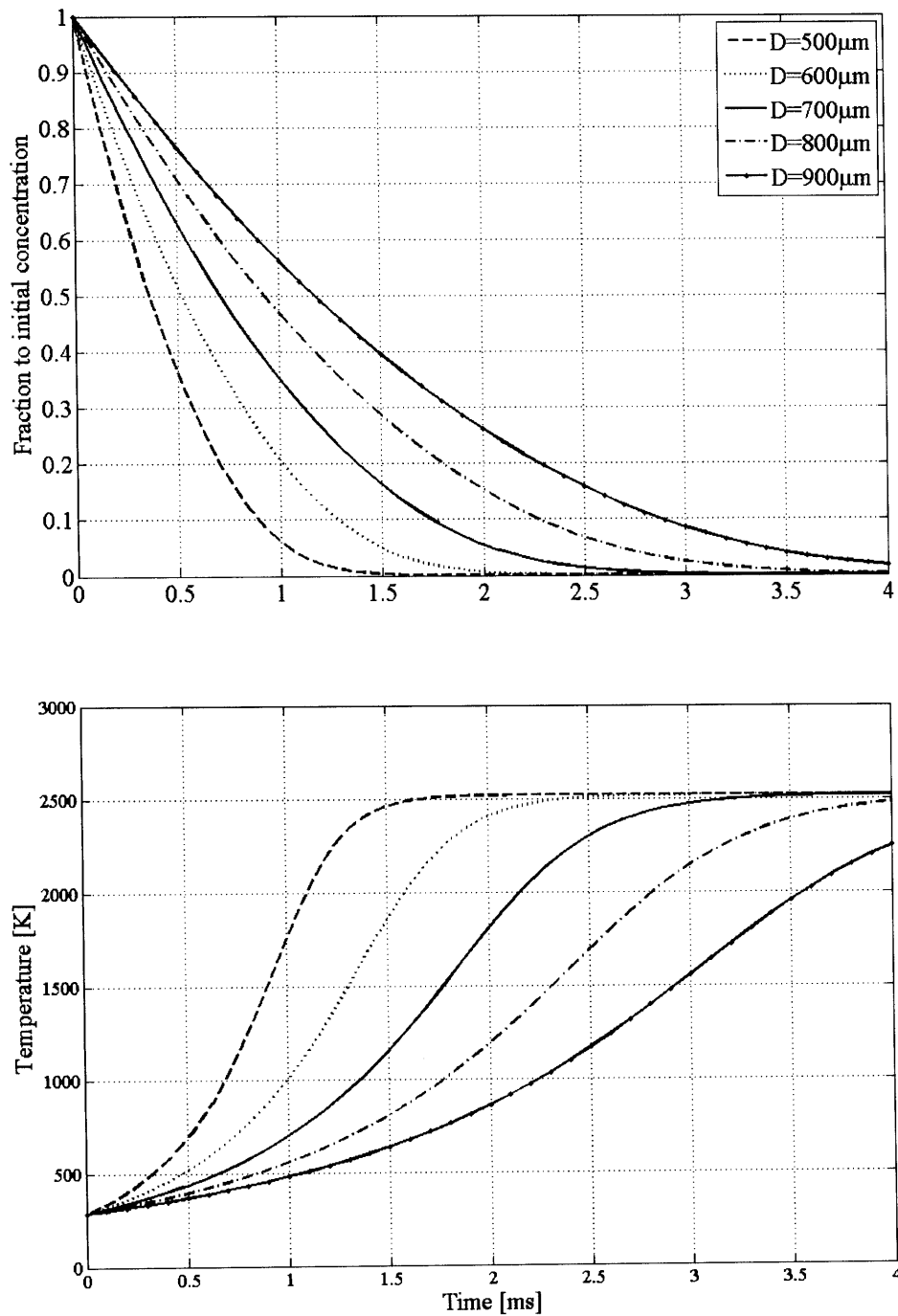


Figure 2-3: Results of the catalytic combustion model for various tube diameters ($\phi = 1.0$, $P = 2.0 \text{ atm}$)

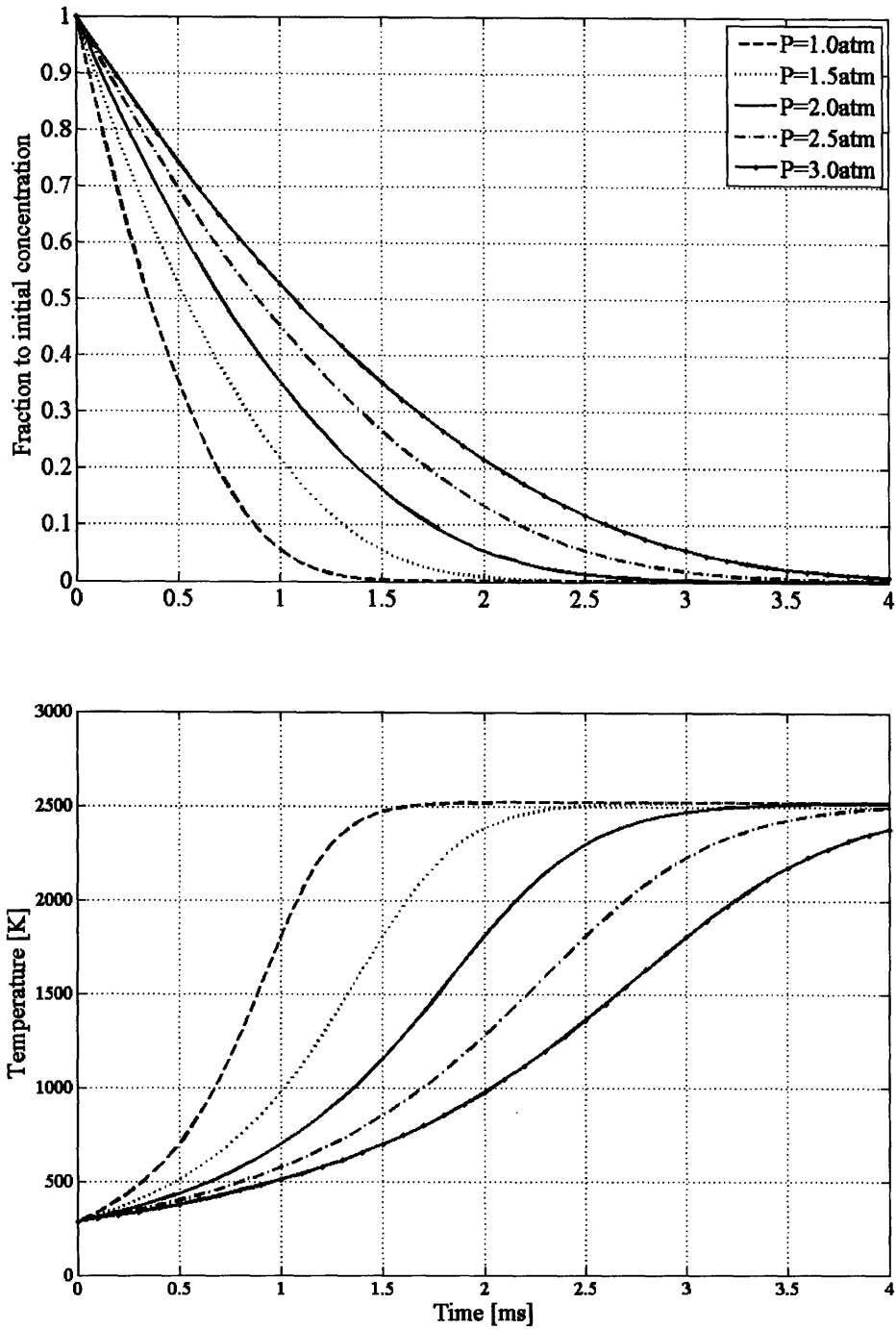


Figure 2-4: Results of the catalytic combustion model for various pressures ($\phi = 1.0$, tube diameter = $700 \mu m$)

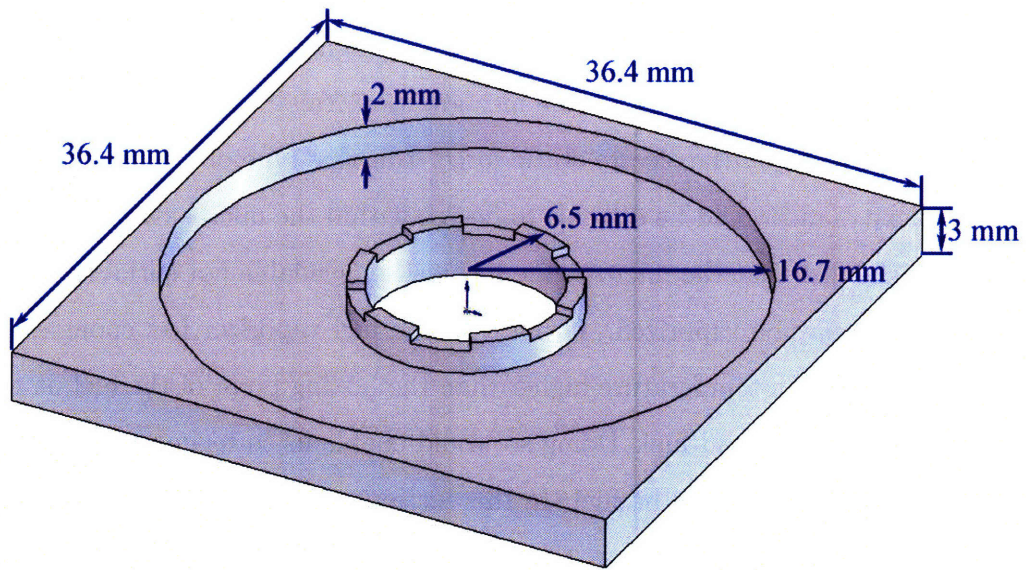


Figure 2-5: Final design of the combustion chamber layer

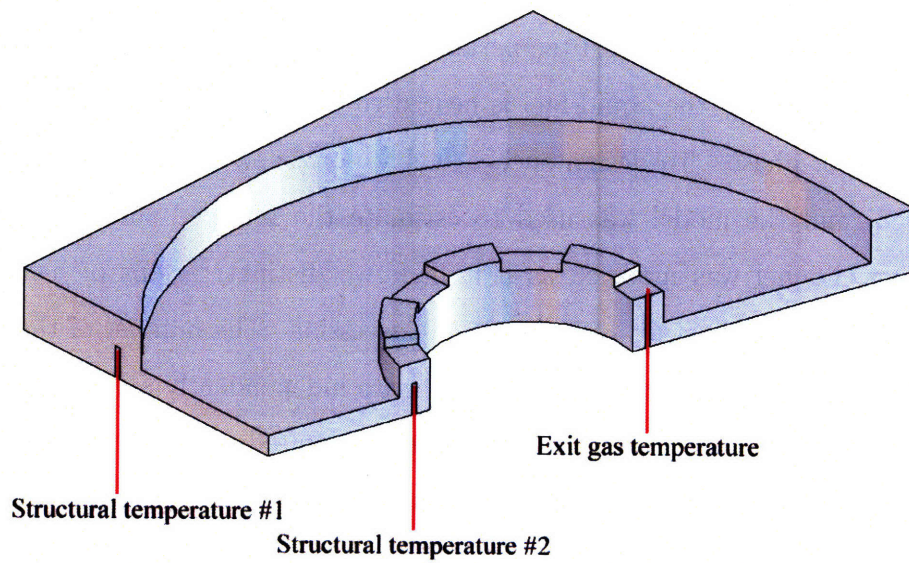


Figure 2-6: Thermocouple locations

be vaporized and mixed with air before entering the combustion chamber due to short flow residence time in it. Therefore, a component that is capable of converting the liquid-fuel into fuel vapor must be built in the microengine. There are many candidate concepts for the fuel vaporizer. The Gomez group at Yale University [34] invented a fuel atomizer driven by the electro-static force. But this type of fuel atomizer would add complexity, and would be difficult to design within the microengine. Instead, we focused on the fact that the microengine has readily available hot surfaces, on which the liquid-fuel may be vaporized. Given that the fuel vaporizer has enough surface area, and is kept at a temperature higher than the boiling point of the fuel, it will be able to vaporize the liquid-fuel. Doing so would enable us to recuperate some of the waste heat while vaporizing the fuel. In this section, a model used to design the fuel vaporizer will be discussed.

2.3.1 Two-region heat transfer model

One effective way to design a fuel vaporizer with a large surface area is to build an array of micro-channels in parallel. The liquid-fuel can be evenly distributed among the channels, whose wall temperature is kept above the boiling point of JP8 fuel. In each channel, the liquid-fuel is heated to the boiling point, then evaporates into the vapor-phase. To design such a fuel vaporizer, a heat transfer model was developed, and the model was used to estimate the required surface area. Each vaporizing channel was modeled as if it had two distinct regions of heat transfer modes: single-phase heating and boiling, in succession. The number of the channels and the hydraulic diameter of each channel were independently set as inputs to the model, then the minimum length of each channel required to completely vaporize the fuel was determined. The model was constructed using the following assumptions:

- The vaporizer is isothermal. This assumption is valid as long as the Biot number is small, so the heat convected into the structure is distributed across the structure rapidly by conduction. Mehra [19] reported that the microengine typically

has a Biot number as low as 0.01⁷.

- There is a clear-cut interface between the two heat transfer regions. Before the interface, heating of the fuel in the liquid-phase happens exclusively, and boiling prevails after the interface.
- The fuel flow is distributed evenly among all the channels. Once the number of the channels is set as an input, the total fuel flow rate is divided by the number of the channels, which gives the fuel flow rate for each channel.

Under these assumptions, the two-region heat transfer model can be depicted as in Figure 2-7. For each heat transfer region, how much heat must be transferred from the wall to the fluid can be calculated if the fuel flow rate is given. Equations (2.21) and (2.22) account for the required heat in the heat-up region and in the boiling region respectively.

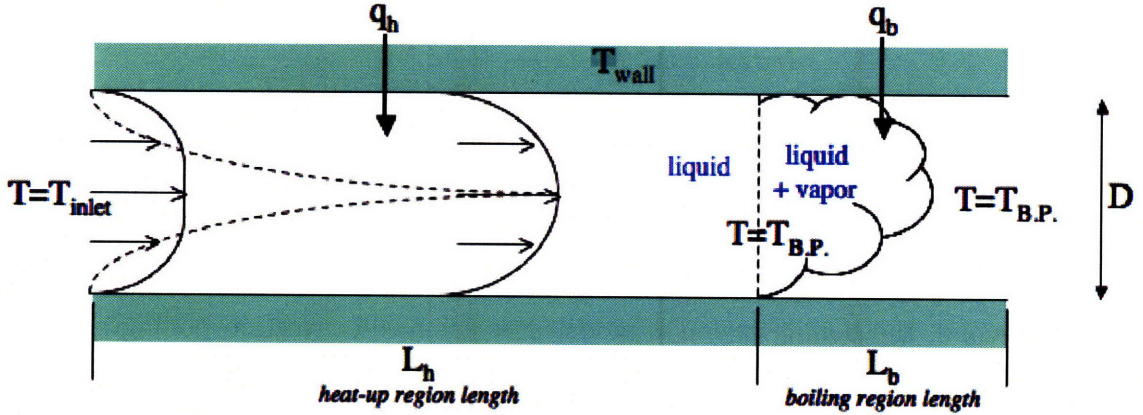


Figure 2-7: Illustrative description of the two-region heat-transfer model

$$q_h = \dot{m}_f C_p (T_{B.P.} - T_{inlet}) \quad [W] \quad (2.21)$$

$$q_b = \dot{m}_f h_{fg} \quad [W] \quad (2.22)$$

where \dot{m}_f is the fuel flow rate, h_{fg} the latent heat of evaporation of the fuel, $T_{B.P.}$ the boiling point of the fuel, and T_{inlet} the temperature of the fuel at the vaporizer

⁷ $Bi = \frac{hL}{k}$ [46]. In a typical microengine setting, it becomes about 10^{-2} ($h \sim 10^3$, $L \sim 10^{-3}$, and $k \sim 10^2$)

inlet. In Figure 2-7, T_{wall} is the temperature of the vaporizer wall, which is assumed to be constant along the channel, and D is the hydraulic diameter of the channel. In addition, L_h and L_b are the lengths of the heat-up region and the boiling region, respectively.

Meanwhile, available heat flux from the wall to the fluid can be estimated by applying appropriate heat transfer equations. First, the heat-up region is modeled as a forced internal flow. For typical operating conditions, the Reynolds number is less than 100, so the flow is considered laminar. The thermal entry length is on the order of a few millimeters, so the entrance region should not be neglected. According to Mills [47], the heat transfer in the laminar entrance region is

$$q_h'' = \frac{Nu_h k}{D} (T_{wall} - \bar{T}_{fluid}) \quad [W/m^2] \quad (2.23)$$

where,

$$Nu_h = 3.66 + \frac{0.065(D/L_h)Re_D Pr}{1 + \{0.04(D/L_h)Re_D Pr\}^{2/3}} \quad (2.24)$$

Note that the heat flux is averaged over the length of the tube by using the average temperature of the fluid, \bar{T}_{fluid} . And, k is the thermal conductivity of the channel wall, silicon in this case.

Second, the boiling region is modeled as a forced-convection boiling heat transfer. For the boiling heat transfer, several empirical correlations can be found in the literature, but the one proposed by Klimenko [48] has been selected because it is a good compromise between simplicity and accuracy [47]. For the microengine operating conditions, the dominant mode of boiling is nucleate boiling⁸. So the following equation can be used [47]:

$$q_b'' = \frac{Nu_b k_l}{L_c} (T_{wall} - T_{B.P.}) \quad [W/m^2] \quad (2.25)$$

⁸If $\Phi < 1.6 \times 10^4$, where $\Phi = \frac{Gh_{fg}}{q''} \left[1 + x \left(\frac{\rho_l}{\rho_v} - 1 \right) \right] \left(\frac{\rho_v}{\rho_l} \right)^{1/3}$, nucleate boiling is dominant over film evaporation [48]. For typical microengine conditions, $\Phi \sim 250$.

where

$$Nu_b = 7.4 \times 10^{-3} q^{*0.6} P^{*0.5} Pr_l^{-1/3} \left(\frac{k_{wall}}{k_l} \right)^{0.15} \quad (2.26)$$

$$q^* = \frac{q_b'' L_c}{h_{fg} \rho_v \alpha_l} \quad (2.27)$$

$$L_c = \left\{ \frac{\sigma}{g(\rho_l - \rho_v)} \right\}^{1/2} \quad (2.28)$$

$$P^* = \frac{PL_c}{\sigma} \quad (2.29)$$

The meaning and the value of all the symbols are listed in Table 2.4. Note that q_b'' also appears in Equation (2.27). Thus, Equations (2.25) through (2.29) need to be evaluated via an iterative manner.

Nomenclature	Property	Value	Unit	Reference
ρ_l	density of liquid	635	kg/m^3	[49]
ρ_v	density of vapor	2.96	kg/m^3	[49]
μ_l	viscosity of liquid	2.53×10^{-4}	Ns/m^2	[49]
σ	surface tension	0.017	N/m	[50]
C_p	specific heat	2640	J/kgK	[49]
k_l	thermal conductivity of liquid	0.1034	W/mK	[49]
h_{fg}	latent heat of evaporation	270	kJ/kg	[44]
$T_{B.P.}$	boiling point	590	K	[49, 51]

Table 2.4: Fluid properties of JP8

2.3.2 Results

Dividing Equation (2.21) by (2.23) gives the surface area needed to bring the fuel temperature to the boiling point. In the same manner, the surface area required to transform liquid-fuel into vapor can be determined by dividing Equation (2.22) by (2.25). For a design fuel flow rate of $0.04 g/sec$, a viable set of dimensions for the vaporizer is listed in Table 2.5. This result shows that the required length of each channel is about $5 mm$ for the listed design parameters. The result is influenced by the fluid properties listed in Table 2.4. To examine the sensitivity to uncertainties in each parameter, a Monte-Carlo simulation was conducted. Each parameter was

assumed to be normally-distributed with a mean value that is listed in Table 2.4 and a standard deviation that matches 10% of its mean value. The required channel length, is most significantly influenced by the difference between the boiling point of the fuel and the wall temperature of the vaporizer. As long as the wall temperature is higher than the boiling point of the fuel by 10 K, the required channel length was always less than 5 mm. According to the Monte-Carlo simulation, uncertainties in each of parameters had a combined effect of reducing the required length of the vaporizer channel. Therefore, a design based on the values in Table 2.4 would be considered as a safe and conservative approach. Details on the sensitivity analysis are included in Appendix C.

Group	Nomenclature	Property	Value	Unit
geometric parameters and operating conditions	\dot{m}_f	fuel flow rate	0.04	<i>g/sec</i>
	D	hydraulic diameter of the channel	500	μm
	N	number of the channels	49	
	P	vaporizer pressure	1	<i>atm</i>
	$T_{B.P.}$	boiling point of fuel	590	<i>K</i>
	T_{inlet}	temperature of fuel at inlet	298	<i>K</i>
required heat flow	T_{wall}	vaporizer wall temperature	600	<i>K</i>
	q_h	heating up to boiling point	30.84	<i>W</i>
	q_b	latent heat of evaporation	10.80	<i>W</i>
heat-up region	q_{total}	total required heat flow	41.64	<i>W</i>
	q_h''	available heat flux	133959	<i>W/m²</i>
	SA_h	surface area required	230	<i>mm²</i>
phase change region	L_h	length required	2.99	<i>mm</i>
	q_b''	available heat flux	71110	<i>W/m²</i>
	SA_b	surface area required	152	<i>mm²</i>
result	L_b	length required	1.97	<i>mm</i>
	L_{total}	total length required	4.96	<i>mm</i>

Table 2.5: List of the vaporizer design parameters and the dimensions set by the design model

Using the result shown in Table 2.5 as a baseline, some parametric variations were studied as well. Figure 2-8 shows the modeling results for different design cases. For most realistic cases, the required length of the vaporizer channels falls within 2 to 10 mm. Eventually, a case of 49 channels with a hydraulic diameter of 500 μm and a

length of 10 *mm* for each was chosen. Because the channels were to be oriented radially, they would taper toward the exit. So, a hydraulic diameter of 500 μm would be a lengthwise average in each channel. At the channel entrance, the hydraulic diameter would be 600 μm , and it would be 300 μm at the channel exit. The fuel vaporizer was designed correspondingly, and shown in Figure 2-9. Built in the fuel vaporizer layer are pressure measurement ports, which connect the combustion chamber to external pressure transducers.

2.3.3 Summary of the fuel vaporizer model

A two-region heat transfer model was developed to design the fuel vaporizer with an array of micro-channels. The model assumes that the fuel is heated in the liquid-phase to the boiling point, and then vaporized. The heat-up region was modeled as laminar entrance region heat transfer by forced internal flow. The nucleate boiling was the dominant boiling mode for the phase-change region. To supply the required amount of heat for fuel vaporization, the model predicted that 49 channels with an average hydraulic diameter of 500 μm and a length of 10 *mm* would be needed. The required length was strongly influenced by the difference between the structural temperature and the boiling point of the fuel. However, when the structure is kept at a temperature about 10 *K* above the boiling point, the required channel length was shorter than 5 *mm* for all the simulation cases. For a given number of the channels, larger hydraulic diameters require shorter lengths (Figure 2-8); although the heat transfer coefficient becomes higher for smaller channels, the channels with larger diameters have more surface area per unit length. This effect is more pronounced for the boiling heat transfer region, so wider channels require shorter lengths.

2.4 Fuel injection holes and mixing chamber

Once vaporized, the fuel enters a mixing chamber through an array of fuel injection holes at the end of each vaporizing channel. Figure 2-10 depicts these fuel injection holes. The size of each hole needs to be properly determined so that the streams of

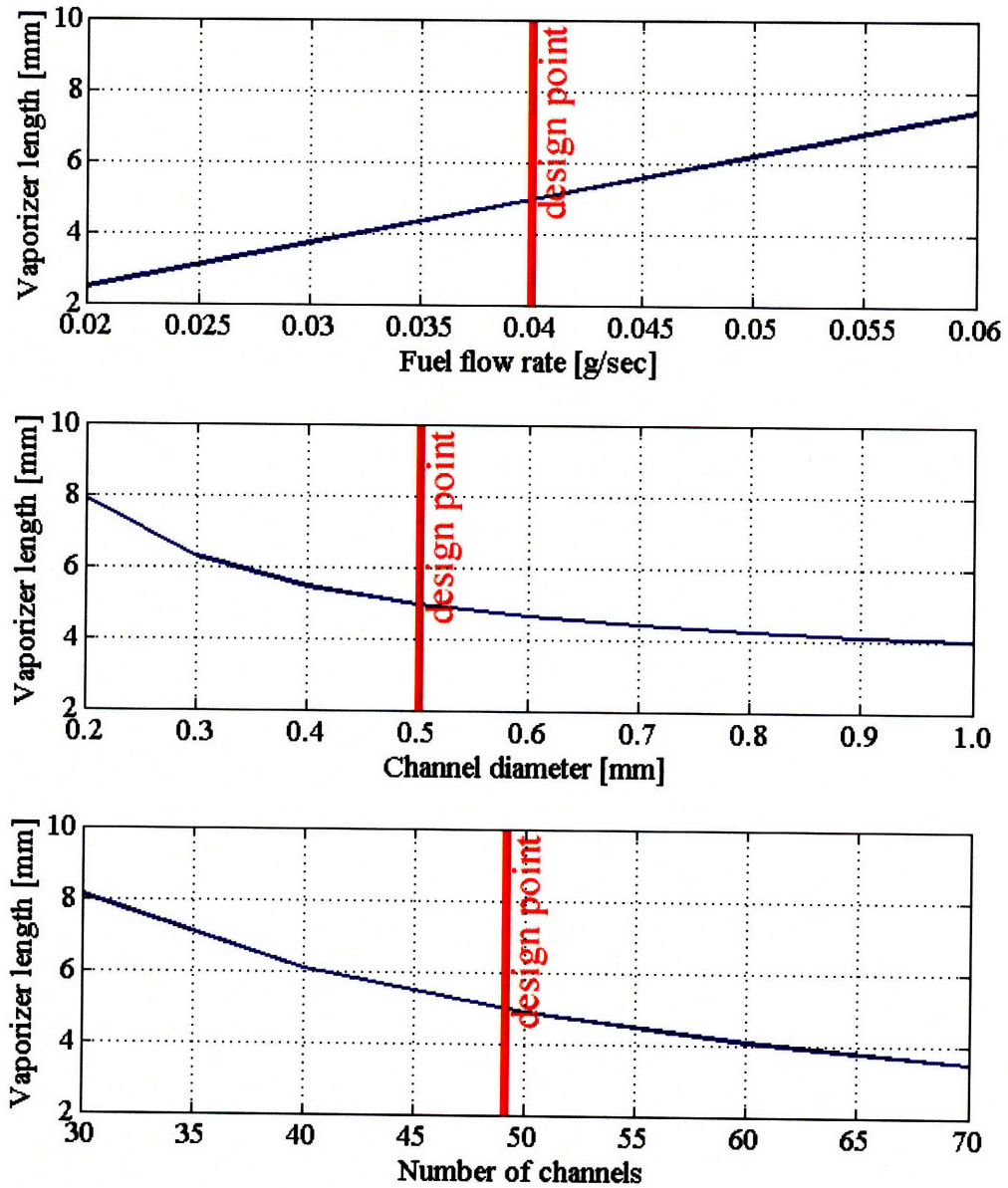
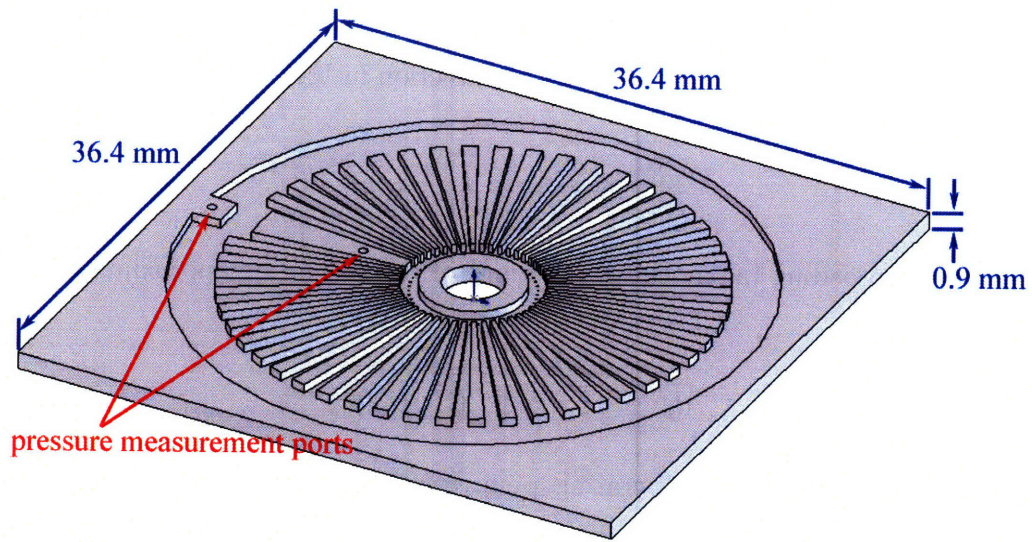
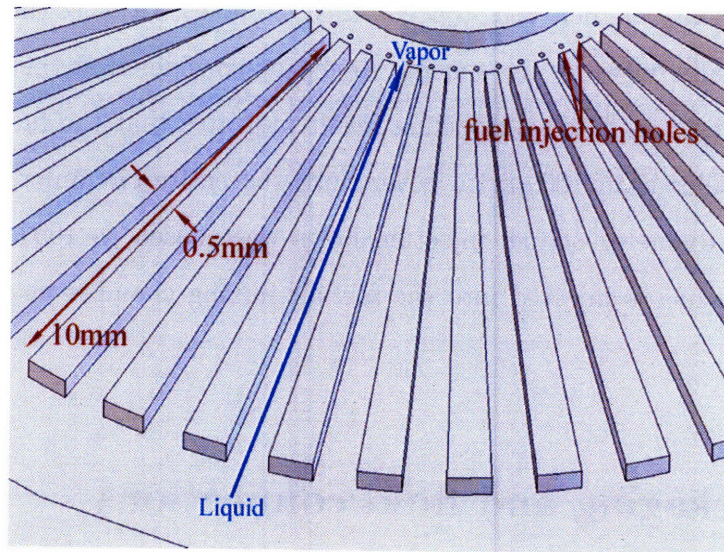


Figure 2-8: Modeling results for various design cases ($\dot{m}_f = 0.04 \text{ g/sec}$, $D = 500 \mu\text{m}$, and $N = 49$, unless otherwise noted)



(a)



(b)

Figure 2-9: Final design of the fuel vaporizer layer (a) and a zoom-in view (b)

fuel vapor injected through the holes spread and mix with the air flow. To simulate how a stream of injected fuel vapor interacts with the air flow, a semi-empirical model by Schetz [3] was used. This model can predict the vertical and lateral spreading of a jet transversely injected into cross-flowing air (Figure 2-11). According to Schetz's correlation, vertical spreading (along the y -direction in Figure 2-11) of the jet can be approximated by:

$$\frac{\delta_y}{d_j} = 0.92 \frac{U_j}{U_\infty} \left[\frac{x}{d_j(U_j/U_\infty)} \right]^{0.4} \quad (2.30)$$

And lateral spreading (along the z -direction) of the jet can be approximated by:

$$\frac{\delta_z}{d_j} = 1.25 \frac{U_j}{U_\infty} \left[\frac{x}{d_j(U_j/U_\infty)} \right]^{0.4} \quad (2.31)$$

With proper values at the operating point, we can calculate the coverage of the injected jet in the mixing chamber. Shown in Figure 2-12 is the normalized coverage in the y - and z -direction. The y -direction coverage was normalized by the height of the mixing chamber ($450 \mu m$), and the z -direction coverage was normalized by the circumferential spacing between adjacent injection holes. Because the flow area grows as it goes radially outward, the spacing should be considered at the outer periphery, which is about $2 mm$ ⁹. The modeling result indicates that the fuel injection holes should be smaller than $100 \mu m$ to cover both the entire circumference and height. Therefore, the diameter of fuel injection holes was chosen as $100 \mu m$. After being vaporized, the fuel is injected into the fuel-air mixing chamber as shown in Figure 2-13.

2.5 Packaging and fluid connections

To run the liquid-fueled micro-combustor, liquid-fuel and pressurized air need to be supplied. In the previous gaseous-fueled micro-combustors, metal tubes were attached directly on the silicon structure to make fluidic connections [19]. This process was

⁹The periphery is $2\pi(15.7 mm) = 98.6 mm$. Because there are 50 injection holes, the spacing becomes $98.6 mm \div 50 = 1.97 mm$.

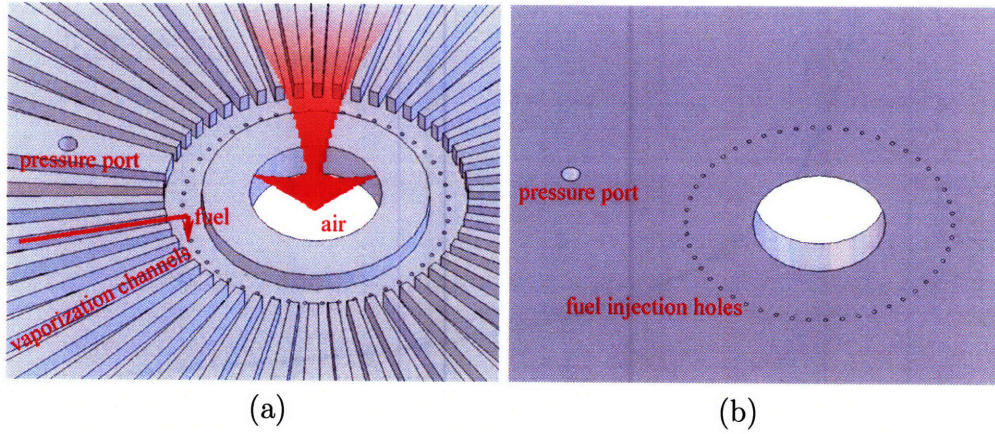


Figure 2-10: Fuel injection holes viewed from above (a) and below (b)

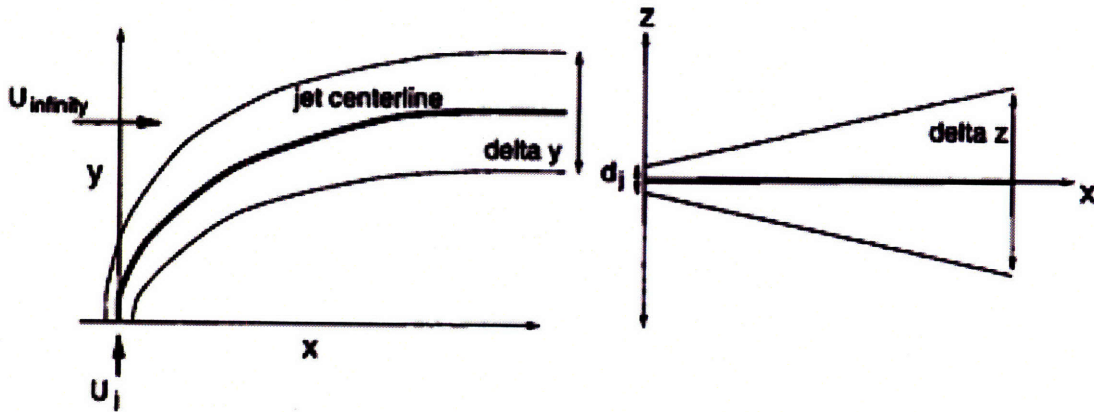


Figure 2-11: Penetration of a jet injected into a cross-flowing air [3]

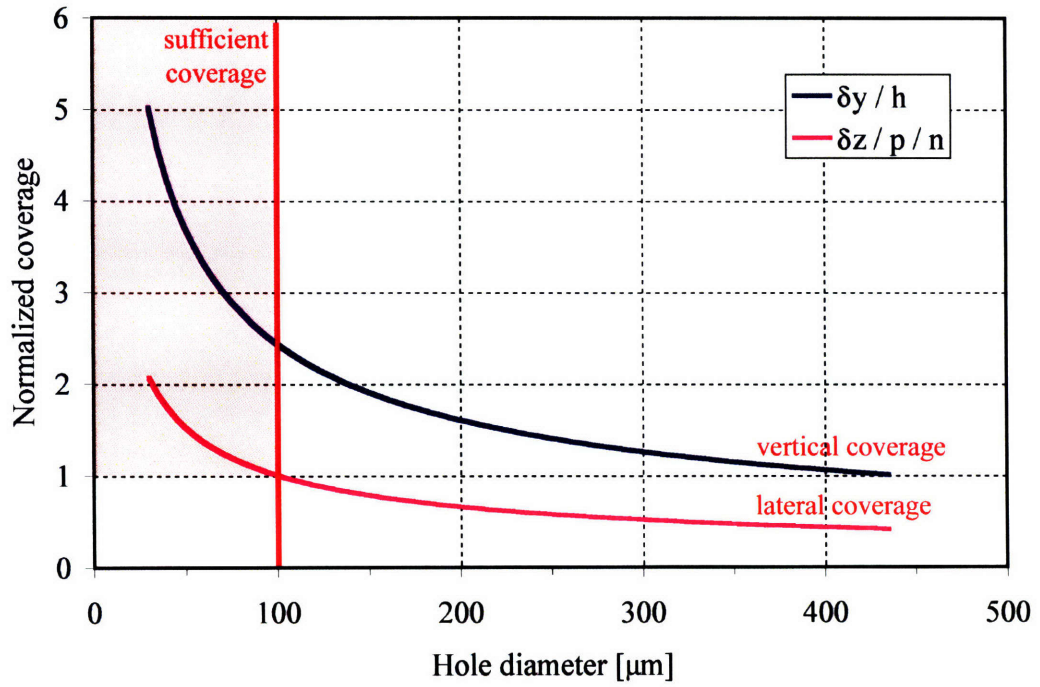


Figure 2-12: Normalized coverage of the injected fuel vapor as a function of the hole diameter

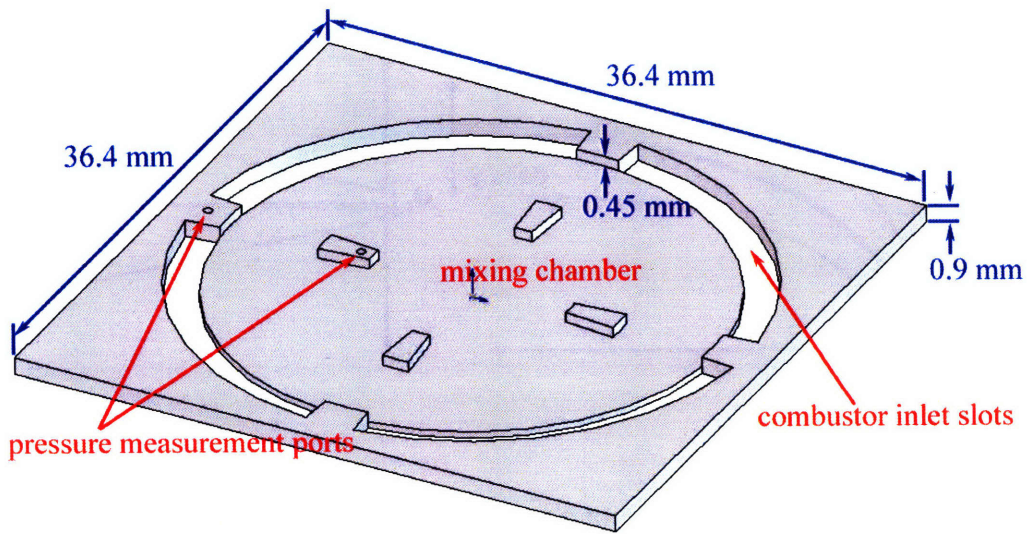


Figure 2-13: Fuel-air mixing chamber layer

done in a furnace environment using glass frits at the interface between the tubes and the silicon structure. However, the glass frit connections were found to be unreliable, and often failed. Rubber o-rings were not deemed useable for this application since even high temperature o-rings cannot tolerate the temperature that the liquid-fueled micro-combustor is designed to operate at, about 900 K. For this build of a micro-combustor, we modified the design to include a thermal isolation layer that would allow the use of o-rings. A glass layer is anodically bonded to the combustor, and extends past the combustor end. As shown in Figure 2-14, the extension block is made from SD-2 glass, a specialty glass that was designed to be anodically bonded to silicon. According to Hoya [52], the thermal expansion coefficient of SD-2 matches silicon over a wide range of temperature, and certain additives (Na^+) assist anodic bonding. In addition, because of its transparency, SD-2 glass can provide a window for visual observation of the fuel vaporizer. Its small thermal conductivity¹⁰ also helps in reducing the required length of the extension. Supplied via the packaging block are air and fuel. In addition, pressure ports for measuring the combustor inlet and exit pressure are built in the packaging block as well.

A finite element model, or FEM, was used to estimate how long the extension needs to be. The maximum allowable operating temperature of silicone o-rings is 500 K [53]. Assuming that the core structure is at 900 K, the model provided the length of the extension to make the packaging end below 500 K. The model is two-dimensional, and assumed natural convection boundary conditions. On the upper surface, the heat-transfer coefficient was assumed to be $10 \text{ W/m}^2\text{K}$. On the lower surface, $5 \text{ W/m}^2\text{K}$ was used. Shown in Figure 2-15 is the FEM result. It shows that if the extension is 30 mm, the temperature of the packaging end would be about 360 K, which is below the temperature silicone o-rings can safely operate. Therefore, with about 10% of safety margin, 33.6 mm was selected as the length of the extension.

¹⁰ $k_{SD-2} = 1.1 \text{ W/mK}$ [52] as opposed to $k_{silicon} = 150 \text{ W/mK}$

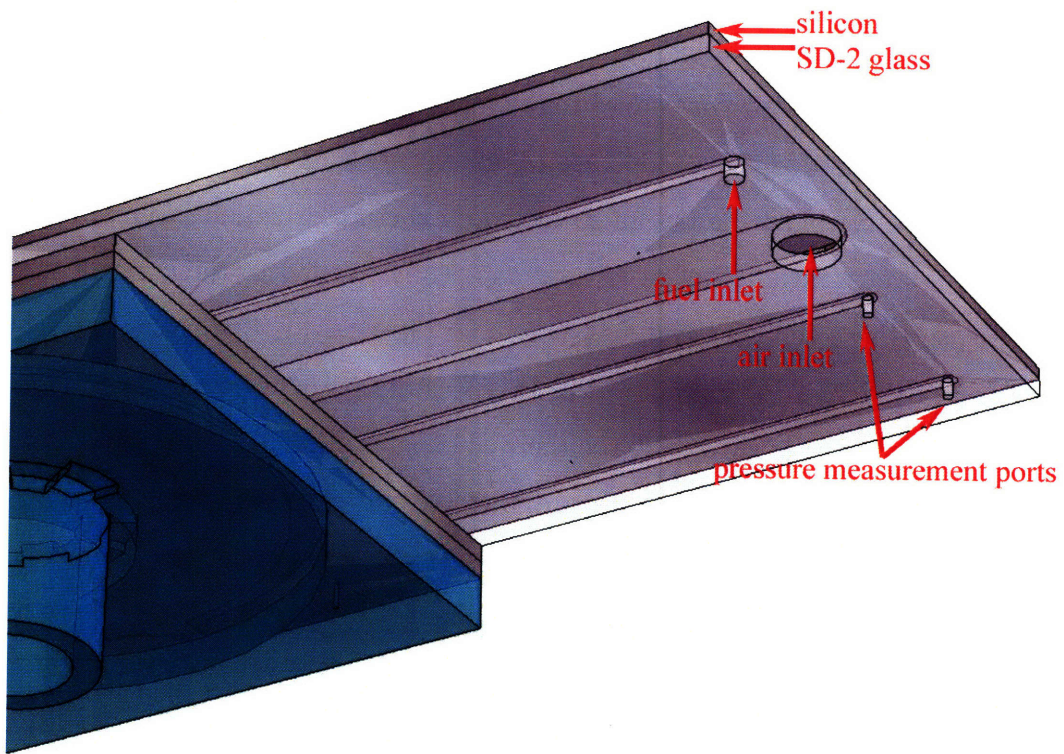


Figure 2-14: Extended packaging block

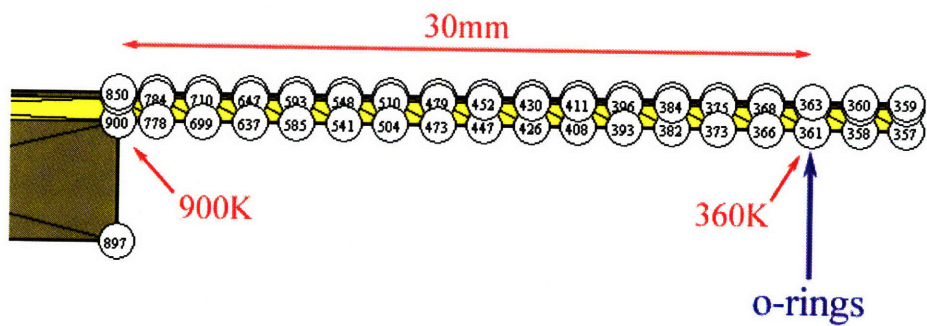


Figure 2-15: Finite element model of the extended packaging

2.6 Clamps

As stated in Section 2.1, the silicon parts and the sapphire parts cannot be permanently bonded, so they were mechanically clamped instead. By opting for mechanical clamps, the parts could be easily taken apart, and the catalytic insert could be examined or replaced as needed. The clamping blocks must exert enough clamping force to prevent leakage, but not too much force to destroy the parts. After reviewing several design candidates, the one as shown in Figure 2-16 was chosen. To securely clamp the parts together, three of them were used on each side and the front (Figure 2-20). Each one was fastened with a spring-loaded bolt, so that it can apply the required clamping force. The clamps were made out of Macor, a machinable glass ceramic, due to its high temperature capability and ease of machining. Between the combustor structure and the clamps, pliant graphite pads were placed for thermal isolation as well as for better traction.

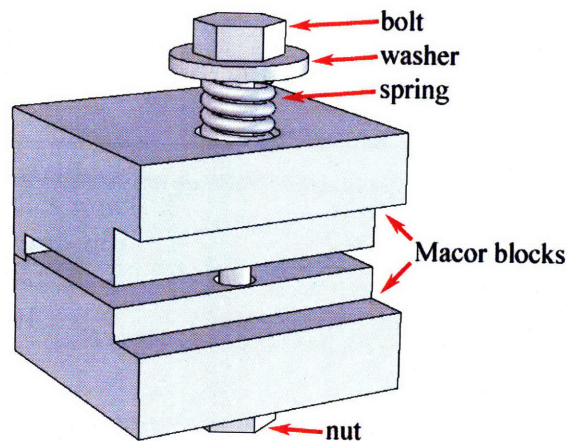


Figure 2-16: Schematic of a spring-laoded clamp that holds the parts together

2.7 Final design

Using the design models described in the previous sections, the geometry and the dimensions of the liquid-fueled micro-combustor were finalized. Key dimensions of the apparatus are listed in Table 2.6. The experimental apparatus consists of six parts

that are either bonded or clamped as shown in Figure 2-17. Explained in Figure 2-18 are fluid flow paths in the device. Air and fuel are supplied through the holes near the edge (a) and (b) in Layer 2, go down along the channels in Layer 1, and enter the device through the holes on the opposite end (c) and (d) of Layer 2. The air goes directly into the mixing chamber, and the fuel enters the vaporizer from the outer diameter. Then, the fuel gets vaporized in the vaporizer channels, and injected into the mixing chamber. The fuel and air are mixed flowing radially outward, then go into the combustion chamber through the inlet slots (e). The fuel and air mixture gets catalytically combusted in the combustion chamber flowing radially inward. Finally, the combustion product exits the device through the exit nozzle. When all the parts are put together, it would look as Figure 2-19. Shown in Figure 2-20 is the final test bed with all the clamps and packaging blocks in place. Note that the assembly in Figure 2-19 is placed upside down when put in the test bed to prevent hot exhaust gas from damaging the test stand.

Group	Parameter	Value
overall	overall die size	$36.4\text{ mm} \times 36.4\text{ mm} \times 6.5\text{ mm}$
	packaging block	$36.4\text{ mm} \times 70.0\text{ mm}$
combustion chamber	volume	1487 mm^3
	outer radius	16.7 mm
	inner radius	6.5 mm
	height	2 mm
	flow area at the exit	$0.77\text{ mm}^2 - 17.3\text{ mm}^2$ (variable)
vaporizer	number of channels	49
	length of each channel	10 mm
	inlet hydraulic diameter	$595\text{ }\mu\text{m}$
	outlet hydraulic diameter	$320\text{ }\mu\text{m}$
fuel injection holes	number of holes	50
	diameter of the holes	$100\text{ }\mu\text{m}$

Table 2.6: Key dimensions of the experimental apparatus

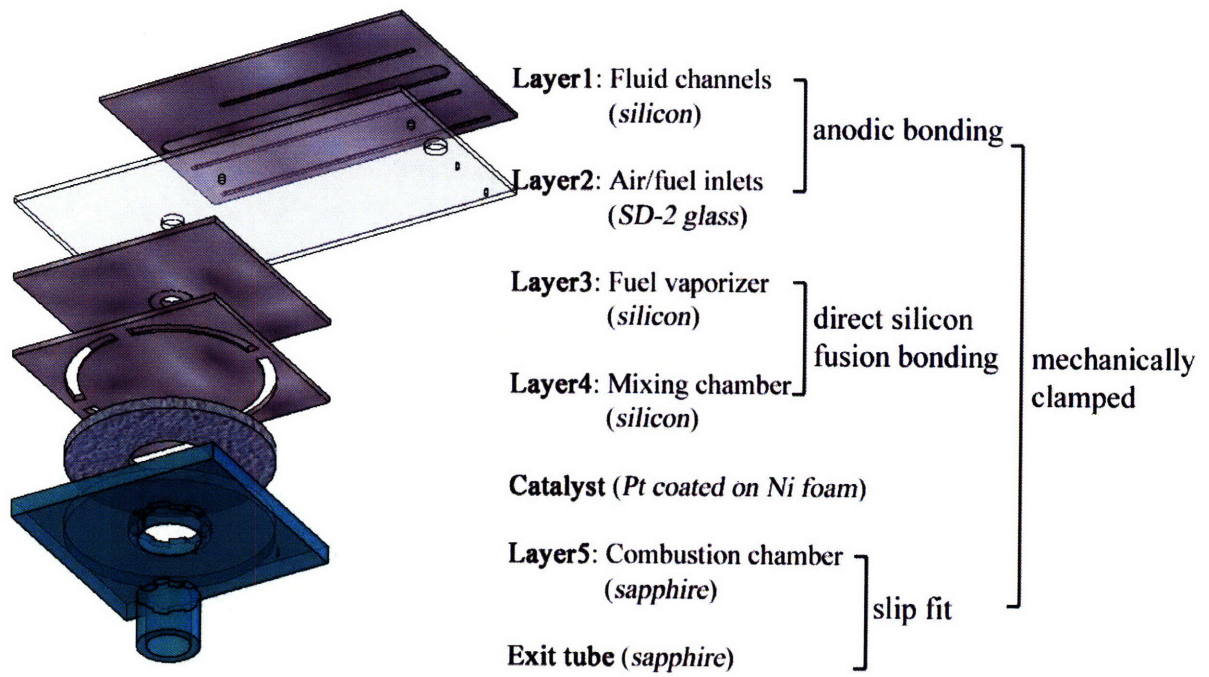


Figure 2-17: Exploded view of the experimental apparatus

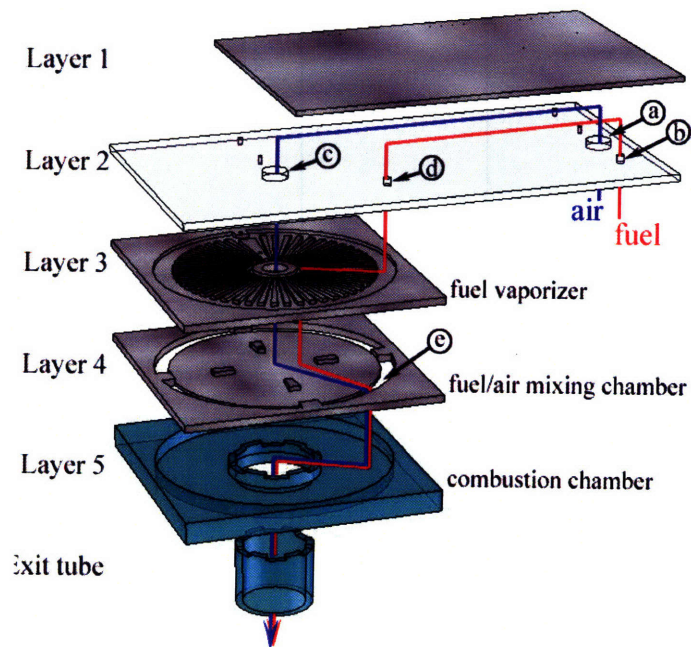


Figure 2-18: Flow paths in the experimental apparatus

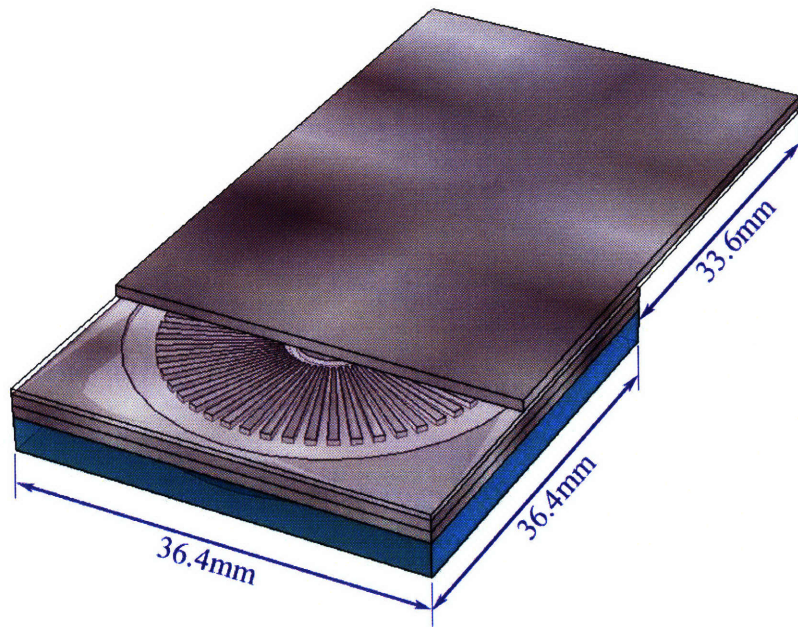


Figure 2-19: Schematic of the experimental apparatus assembly

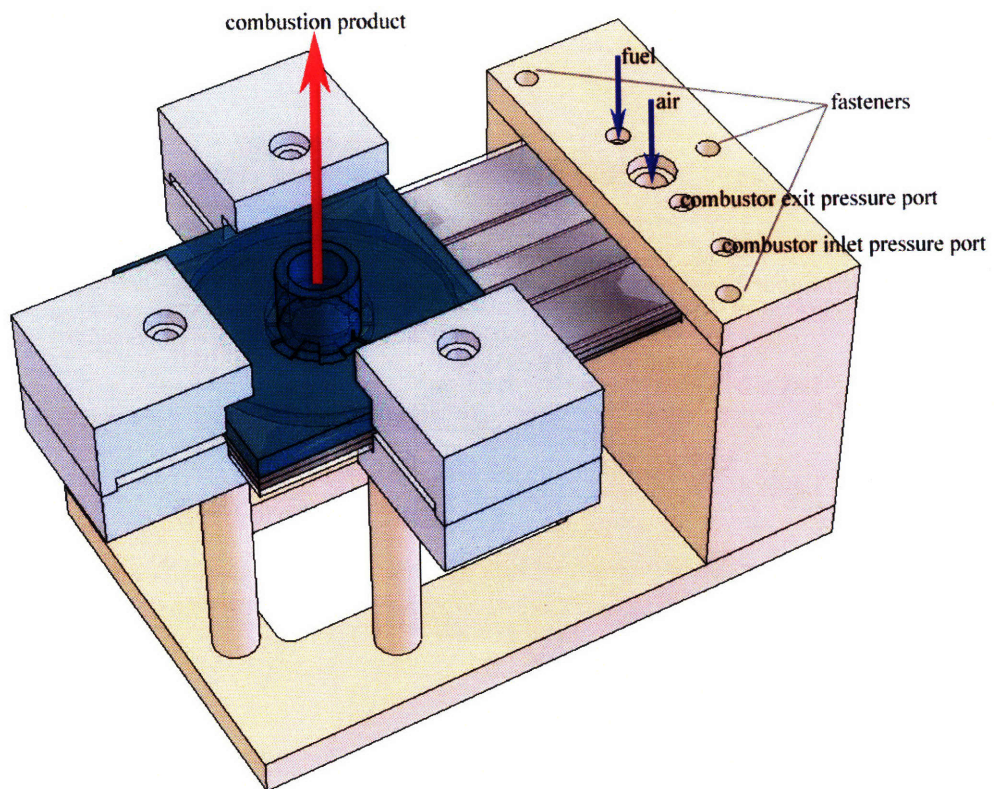


Figure 2-20: Schematic of the fully packaged test bed

2.8 Chapter summary

In this chapter, an experimental apparatus was designed to explore the concept of the liquid-fueled micro-combustor. During the design procedure, various design models were developed and used. Among those design models, the most important is the catalytic combustion model. It can be more generally applied when designing catalytic combustors of similar configurations. Using the model, the reaction time-scale of the catalytic combustion of JP8 was estimated, and the combustion chamber was designed to have the mass flow rate capability of the design requirement. The fuel vaporizer has been methodically designed as well. Utilizing hot structures in the microengine, a fuel vaporizer with a compact size was designed. Fuel-air mixing chamber was sized carefully, too. Finally, an experimental test rig with an overall dimension of $36.4\text{ mm} \times 36.4\text{ mm} \times 6.5\text{ mm}$ and a combustion chamber volume of 1.4 cc was designed. The next chapter will discuss the fabrication of the liquid-fueled micro-combustor.

Chapter 3

Apparatus Fabrication and Experimental Setup

Chapter 2 discussed how the experimental apparatus was designed. This chapter describes how it was built. The experimental apparatus is a hybrid structure consisting of three different materials: silicon, sapphire, and SD-2 glass. Each material was machined with different methods. Figure 3-1 shows an exploded view of the apparatus as well as the label, material, features, and the fabrication method for each part. The sapphire combustion chamber (Layer 5), exit tube, and SD-2 packaging glass (Layer 2) were fabricated with ultrasonic machining by Bullen Ultrasonics. The three silicon layers were micro-machined in the Micro Technology Laboratory (MTL) at MIT. The catalytic inserts were cut in the MIT machine shop, and coated with platinum in MIT's Technology Laboratory for Advanced Materials and Structures (TELAMS). Key fabrication steps will be explained in the subsequent sections in the chapter.

3.1 Silicon micro-fabrication

3.1.1 Overview

Layers 1, 3, and 4 (see Figure 3-1) were fabricated with silicon micro-machining techniques. Layer 1, containing four channels for fuel supply, air supply, and two

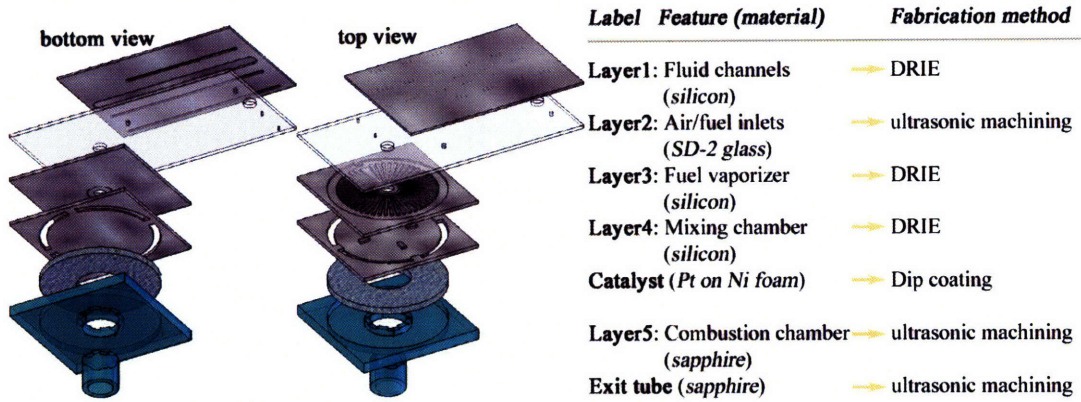


Figure 3-1: Label, material, features, and fabrication method for each part

pressure taps, involved Deep Reactive Ion Etching (DRIE) on one side of a silicon wafer. Layer 3, the fuel vaporizer, involved DRIE from the both sides of a wafer; half-way through from the front-side to define the vaporizer channels, and half-way through from the opposite side to make through holes (fuel injectors and pressure ports). Layer 4 was prepared in a similar manner; half-way from the front-side to make the mixing chamber and half-way from the back-side to make the combustor inlet slots as well as the pressure ports. In this micro-fabrication procedure of three wafers, seven photomasks were used. Brief descriptions of each photomask are listed in Table 3.1. A complete set of the photomask drawings is included in Appendix A.

Photomask	Layer	Major features
Mask #1	Layer 1	alignment marks / die-saw lines
Mask #2	Layer 1	fluid connection channels
Mask #3	Layers 3 & 4	alignment marks / die-saw lines
Mask #4	Layer 3 front-side	vaporizer channels / pressure ports
Mask #5	Layer 3 back-side	fuel injection holes / pressure ports
Mask #6	Layer 4 front-side	air/fuel mixing chamber / pressure ports
Mask #7	Layer 4 back-side	combustor inlet slots / pressure ports

Table 3.1: Description of each photomask

Figure 3-2 schematically summarizes the micro-fabrication procedure used for Layers 3 and 4. Beginning with a $900\ \mu\text{m}$ -thick double-side-polished wafer, approximately $3000\ \text{\AA}$ of field oxide was grown to protect the bonding surfaces. After that, alignment marks and die-saw lines were etched on the front-side by shallow DRIE ($0.5\ \mu\text{m}$). For

double-sided DRIE, both the front and the back side of the wafer were covered with photoresist, and the patterns were transferred on both sides. Prior to etching, the field oxide on the pattern areas was removed by Buffered Oxide Etch (BOE). When one side of the wafer is being etched with DRIE in a vacuum chamber, the other side is cooled with helium. To prevent helium leakage into the vacuum chamber, through holes should not be present on a wafer during DRIE. Thus, the front-side was etched $450\ \mu\text{m}$ deep, and the wafer was mounted on a blank wafer using photoresist as an adhesive. Then, the back-side etch was performed. Layer 1 was prepared with a similar procedure excluding the back-side etch. Layers 3 and 4 were then bonded at the wafer level with aligned fusion bonding, which was followed by die-sawing. On the other hand, Layer 1 was die-sawed first, and then anodically bonded to Layer 2 (SD-2 glass) at the die level.

3.1.2 Photolithography

Photolithography is a process used in micro-fabrication to define patterns on a thin polymer film (photoresist) deposited on a silicon substrate. The patterns on the photoresist are used later as an etch mask during the silicon etch process. The fabrication of the liquid-fueled micro-combustor exclusively used dark-field photomasks and positive photoresists. Two-dimensional features that would be removed from the silicon substrate are defined as transparent areas on the photomask. The photomask is aligned with the wafer coated with the photoresist, and the pair is exposed to ultra-violet rays. During the development after the exposure, the photoresist on the areas that were exposed to the ultra-violet rays dissolves away revealing bare silicon, or silicon oxide if the substrate has a field oxide. The silicon oxide can be removed by Buffered Oxide Etch (BOE) before the silicon etch process.

Depending on the etch depths, two types of photoresists were used in the fabrication of the liquid-fueled micro-combustor. For the shallow etch ($0.5\ \mu\text{m}$) of the alignment marks and the die-saw lines, $1\ \mu\text{m}$ -thick OCG 825-20 photoresist was used. This thin photoresist can be stripped off in an acidic etchant called Piranha ($\text{H}_2\text{O}_2:\text{H}_2\text{SO}_4$ 4:1) after the etch is done. For DRIE ($450\ \mu\text{m}$), $10\ \mu\text{m}$ -thick AZ P4620 photoresist

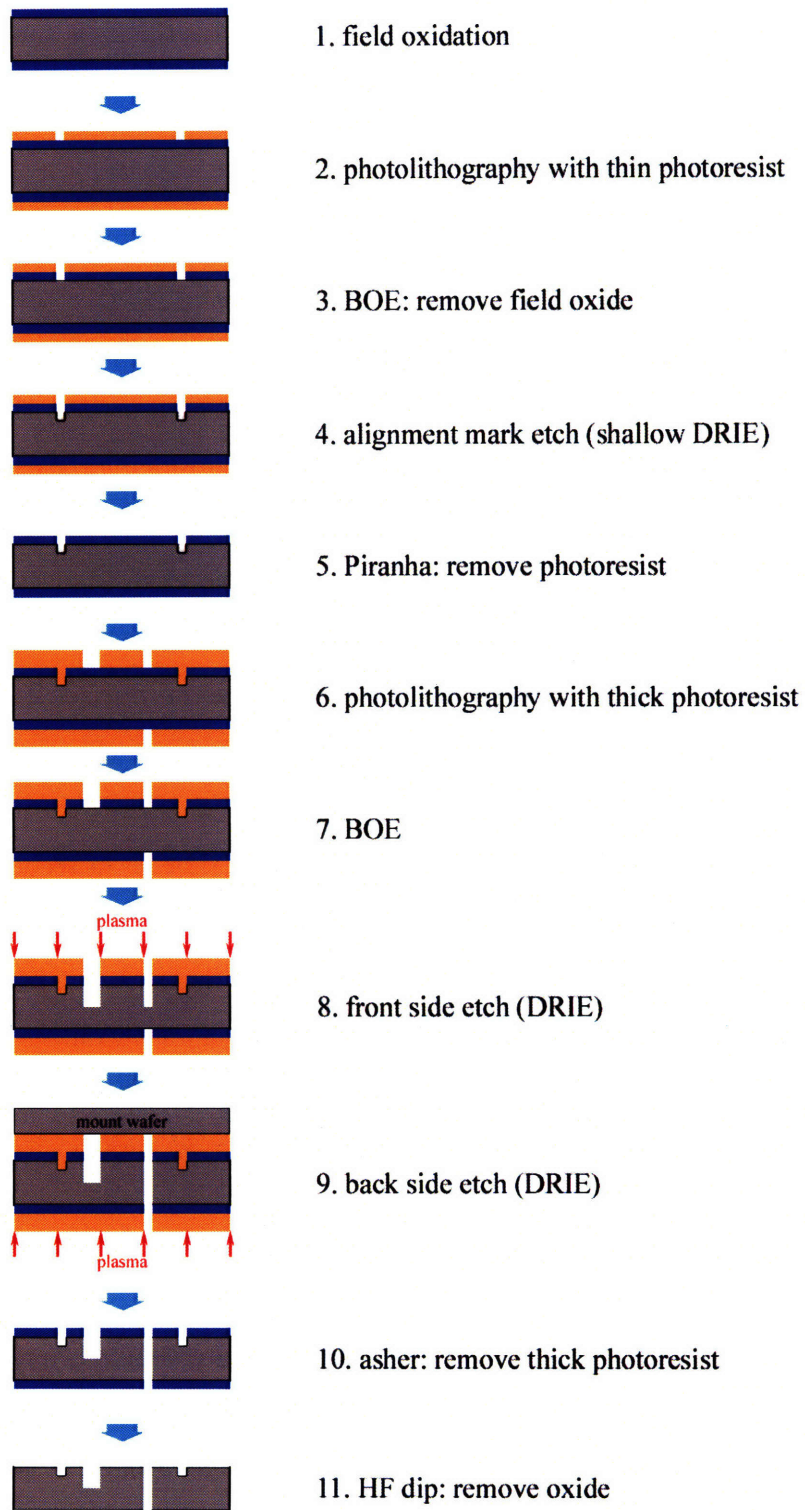


Figure 3-2: Schematic description of the micro-fabrication procedure (not to scale)

was used. Due to the thickness, the ultra-violet exposure had to be two times, 9 seconds each, separated by an interval of 15 seconds. This thick photoresist is usually removed by plasma ashing after DRIE.

3.1.3 Deep Reactive Ion Etching

Deep Reactive Ion Etching (DRIE) was performed using Bosch's proprietary technology, Time-Multiplexed Deep Etching (TMDE). This is an enabling technology for many power-MEMS applications. It is a dual-mode etching process that uses sulfur hexafluoride (SF_6) plasma for removing silicon, and deposits fluorocarbon (C_4F_8) for sidewall protection. The continual switching between the etch mode (SF_6) and the passivation mode (C_4F_8) results in a highly anisotropic etch. Aspect ratios of 30:1 can be typically achieved, and etch rates of $3 \mu\text{m}/\text{min}$ are considered standard [54].

For the fabrication of the liquid-fueled micro-combustor, Surface Technology Systems's (STS) Inductively Coupled Plasma (ICP) etching machine was used. The recipe was optimized by previous MIT researchers. For each cycle, the etch (SF_6) time was set to 15 seconds, and the passivation (C_4F_8) time to 11 seconds. When the etch time is too long, the sidewalls become wavy. When the etch time is too short, the overall etch rate of the DRIE process is too slow or even non-existent because the wall passivating polymer should first be removed before silicon is etched per each cycle. The MIT recipe offers a good compromise between the sidewall smoothness and the etch rate. Figure 3-3 shows a picture of the Layer 1 wafer after DRIE.

3.1.4 Silicon fusion bonding

Two silicon wafers can be bonded directly without an intervening layer or applying an electric field. This is called silicon fusion bonding. Although the bonding mechanism is not fully understood, a chemical reaction between OH groups in the oxide layers is believed to be the cause [55]. Layers 3 and 4 were bonded at the wafer level with silicon fusion bonding. In order for the wafers to be bonded, it is extremely important that no particles are present on the bonding surfaces as they will cause a bonding

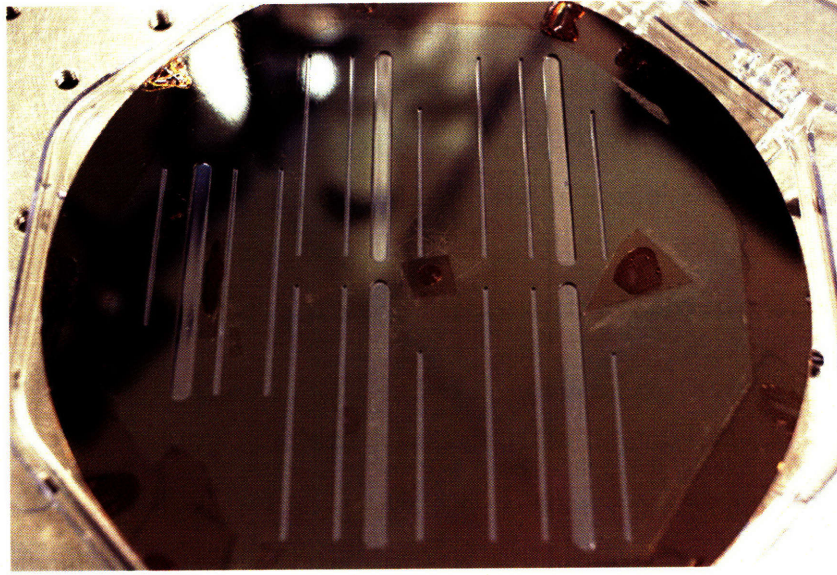


Figure 3-3: Layer 1 after Deep Reactive Ion Etching

imperfection, and possibly a leakage flow in the device. Thus, the wafers were first cleaned with a rigorous procedure prior to the bonding:

1. Plasma ashing for 120 minutes to remove photoresist and C_4F_8 residues from the DRIE process
2. Piranha for 10 minutes to remove organic contaminants
3. Hydrogen fluoride (HF) dip for 10 minutes to strip off the field oxides
4. RCA cleaning with the HF dip step omitted

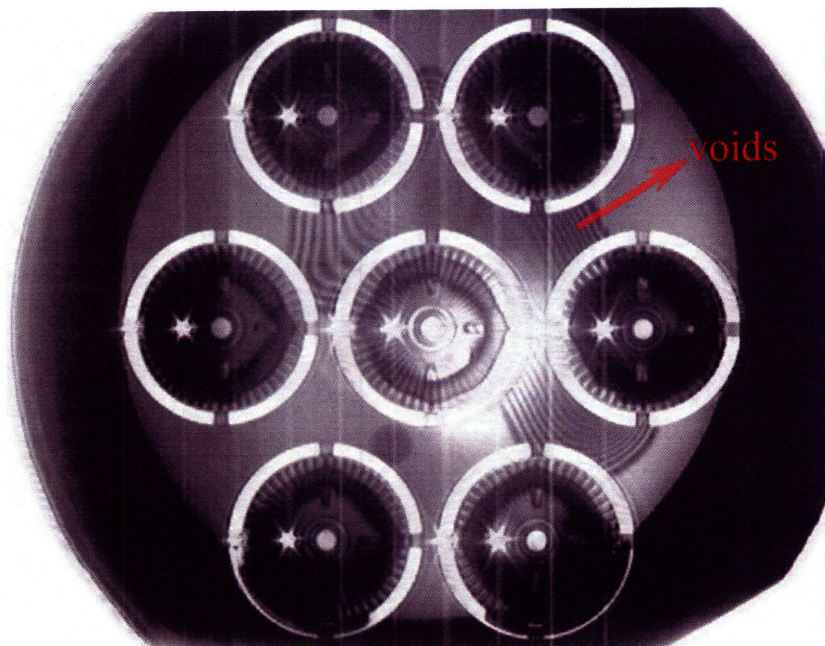
After this cleaning procedure, the Layers 3 and 4 wafers were immediately brought into contact. Alignment marks on the two wafers were precisely lined up using Electronic Visions's wafer aligner, EV510. When the wafers were put into contact, some fringes were visible under an infrared camera (Figure 3-4 (a)). The fringes indicate that there are voids between the wafers, perhaps due to particles or blemishes on the wafers. The bonded wafer pair was pressed down around the fringes with a plastic tweezer, and they became noticeably smaller as shown in Figure 3-4 (b). Then, the bonded wafers were annealed for an hour in a furnace at $1000^\circ C$, and most of the voids disappeared (Figure 3-4 (c)). Figure 3-5 is a photograph after the silicon fusion

bonding of the Layer 3 and 4 wafers. Following the silicon fusion bonding, the bonded wafer pair was die-sawed. Figures 3-6 and 3-7 show the front and the back side of the completed part, respectively. In Figure 3-6, microscopic images of the vaporizer channels and the fuel injection holes are also shown.

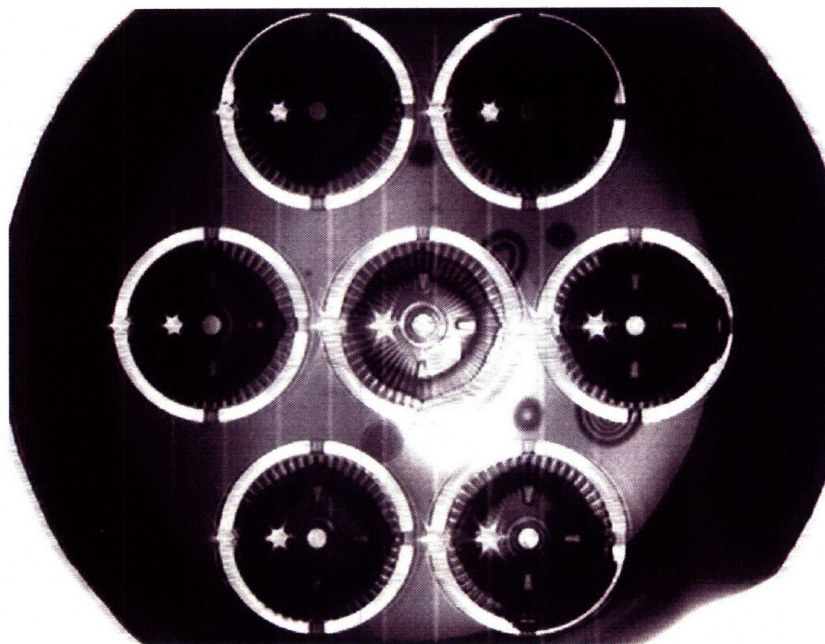
3.1.5 Silicon-to-glass anodic bonding

Anodic bonding is a commonly used technique for establishing a bond between silicon and glass. For anodic bonding, silicon and glass are put into contact, and a high voltage is applied across the two while keeping them at an elevated temperature, typically 350 to 400 °C. Borosilicate glass is generally used for an anodic bonding to silicon. However, the thermal expansion coefficients of silicon and borosilicate glass differ at the bonding temperatures. Hence, when the pair is cooled down to room temperatures, residual stress is formed, causing distortion in the device. To alleviate this issue, the liquid-fueled micro-combustor used a specialty glass substrate, SD-2, manufactured by Hoya. SD-2 is a glass substrate designed to match the thermal expansion coefficient of silicon throughout a wide range of temperature. It also contains Na⁺ ions, which boost bond strength. Figure 3-8 illustrates the scheme of silicon-to-glass anodic bonding. The silicon piece is connected to the anode, and the SD-2 glass to the cathode. When the voltage is removed, an electrostatic force is permanently formed and holds the two pieces together. Layers 1 and 2 were anodically bonded at the die level. First, Layer 1 was die-sawed and cleaned with the following procedure:

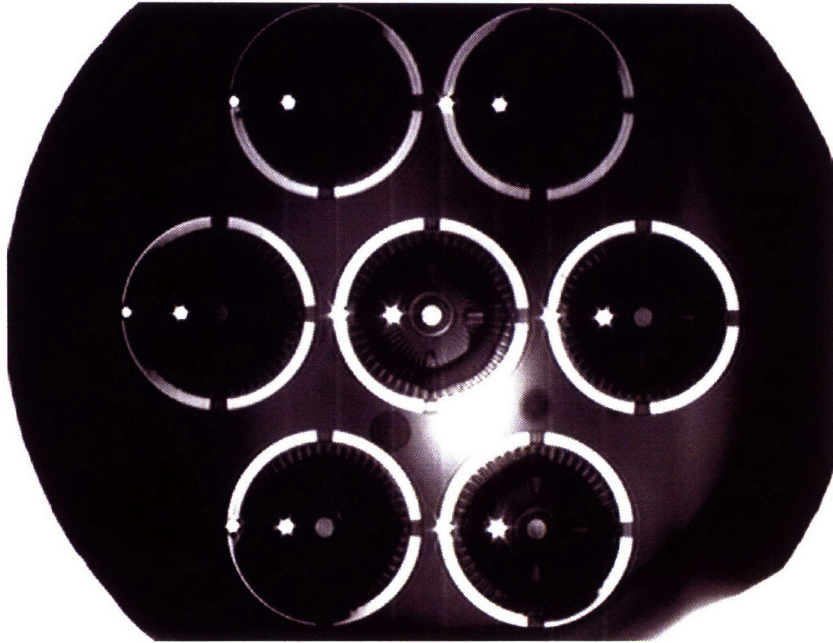
1. Acetone dip for 12 minutes with ultrasound agitation
2. Rinse with methanol
3. Rinse with isopropanol
4. Dry with a nitrogen blower
5. Plasma ashing for 60 minutes to remove C₄F₈ residues and photoresist
6. Piranha for 10 minutes to remove remaining organic contaminants



(a)



(b)



(c)

Figure 3-4: Infrared images taken during the silicon direct bonding: immediately after contact (a), after the voids were pressed down (b), and after annealing for an hour (c)

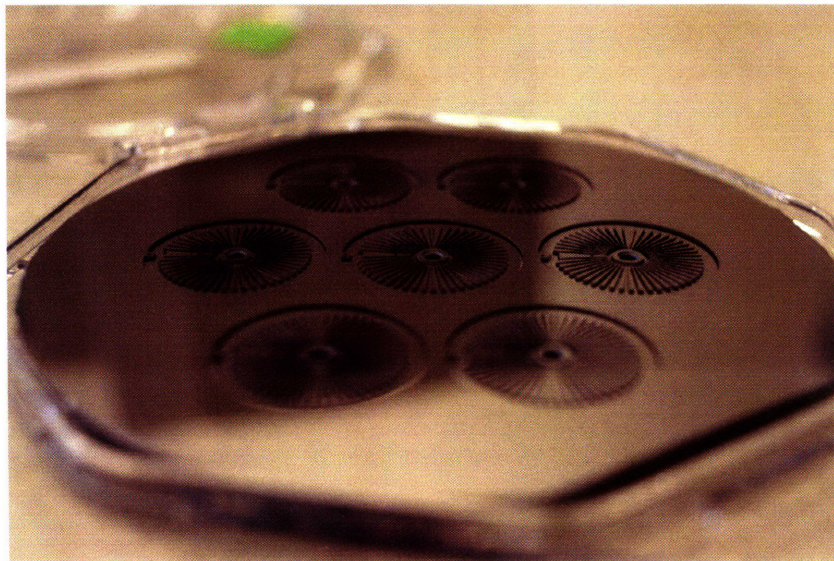


Figure 3-5: Picture of the bonded wafers for Layers 3 and 4

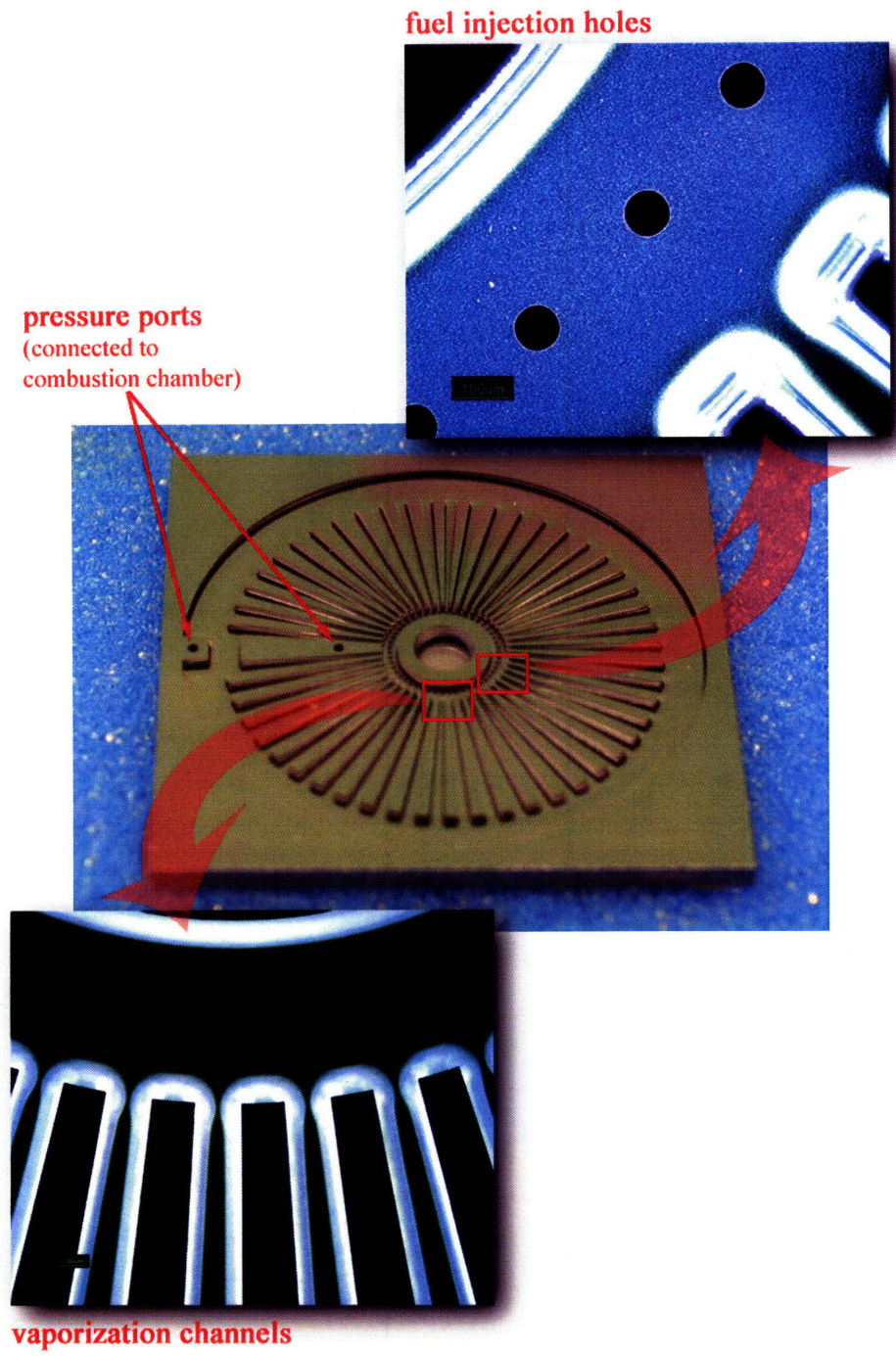


Figure 3-6: Front side of the completed silicon piece (showing the front side of Layer 3)

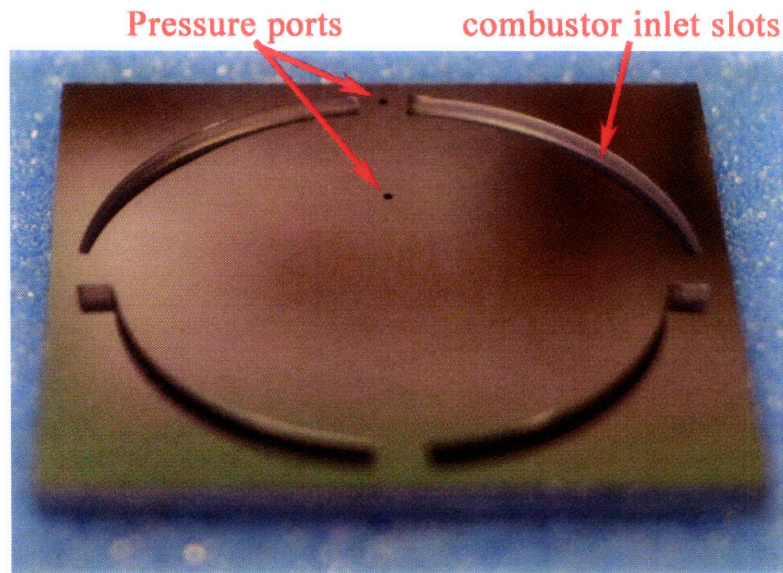


Figure 3-7: Back side of the completed silicon piece (showing the back side of Layer 4)

7. HF dip for 10 minutes to strip the oxide
8. Rinse with de-ionized water and dry with a nitrogen blower

Layer 2, which was ultrasonically machined by an outside vendor, was cleaned in the Piranha solution for 10 minutes, followed by a rinse and dry.

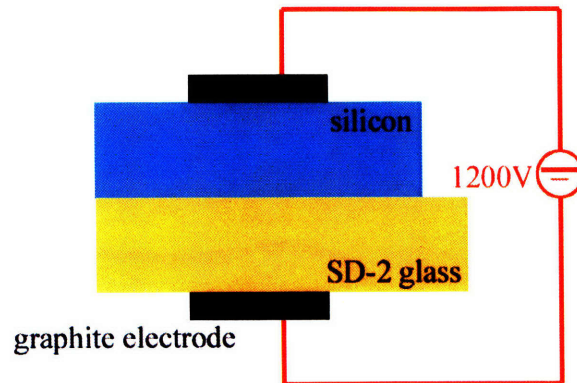


Figure 3-8: Schematic of anodic bonding between silicon and SD-2 glass

After the cleaning procedure, the two pieces were put together and mounted on an anodic bonding chuck as shown in Figure 3-9. The edges of the two pieces were

carefully placed against the chuck, providing an alignment good enough to preserve the flow paths. Then, the chuck was put in an oven set to 350°C . An electric potential of 1200 V (DC) was applied across the silicon and the SD-2, which resulted in an electric current of 4.7 mA . The current gradually decreased, dropping below 10% of the initial value within 10 minutes. Figure 3-10 shows the current trace versus time. The voltage was removed after an hour, and the chuck was taken out of the oven. Figure 3-11 shows the finally bonded pair of Layers 1 and 2.

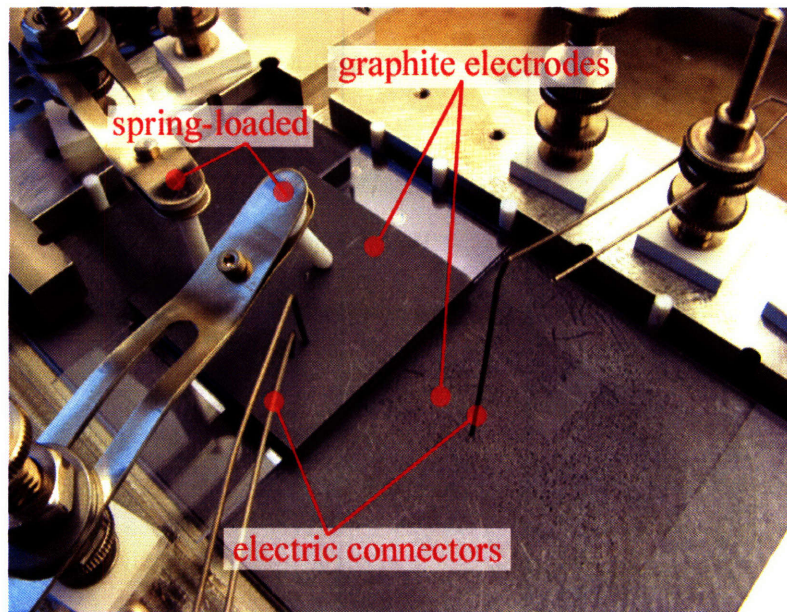


Figure 3-9: SD-2 glass and silicon pieces mounted in an anodic bonding chuck

3.2 Ultrasonic machining

Ultrasonic machining is a fabrication technique that utilizes a tool vibrating at a high frequency, typically 20 to 40 kHz. This ultrasonic vibration is acoustically transmitted to abrasive slurry flowing through a narrow gap between the tool and the workpiece, leading to microscale abrasion and material removal from the workpiece. This is an effective way to machine a brittle material at a very small scale. Layer 2 (SD-2 glass), Layer 5 (sapphire), and the exit tube (sapphire) were built using ultrasonic machining techniques by Bullen Ultrasonics, Inc.. A complete set of mechanical drawings for

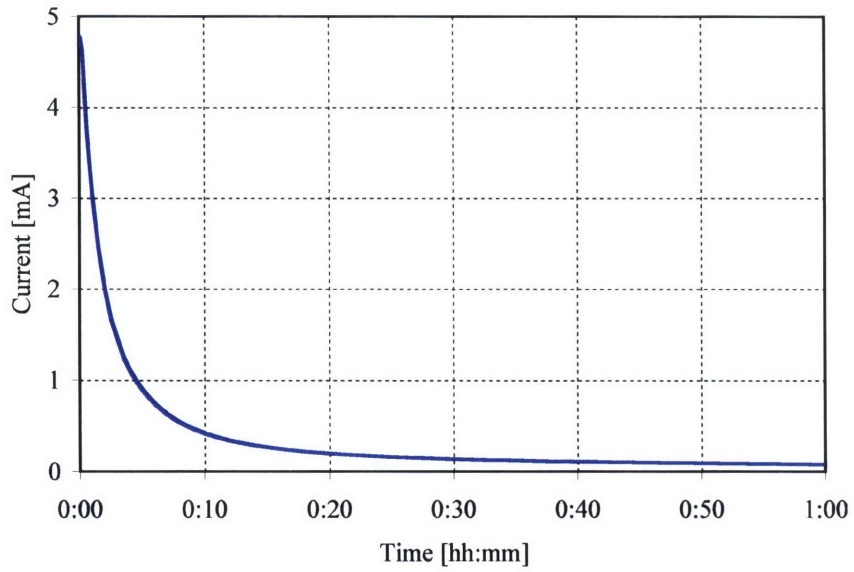


Figure 3-10: Electric current across the silicon-SD2 interface during anodic bonding under 1200 V

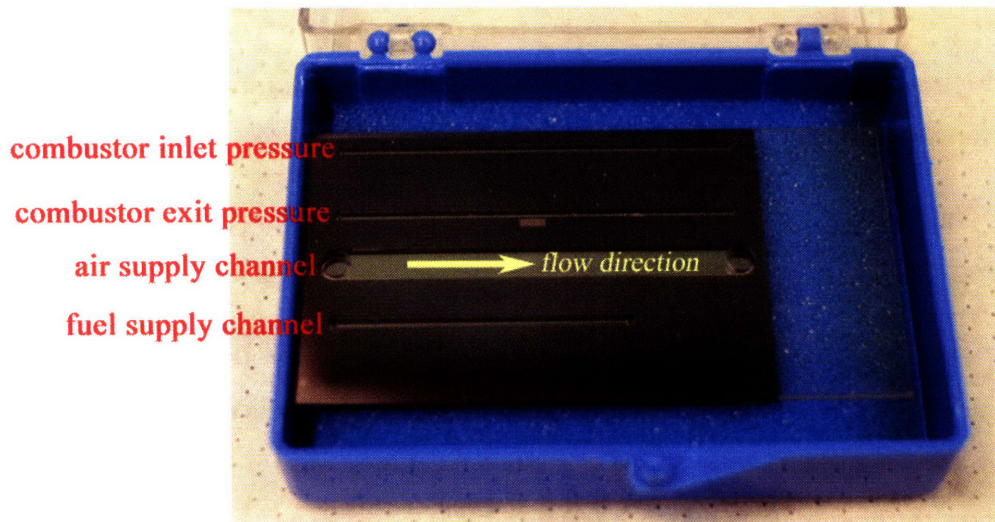


Figure 3-11: Layers 1 and 2 anodically bonded

these parts is included in Appendix B. The smallest features machined with this technique were the thermocouple holes in Layer 5, which had a diameter of $250\ \mu\text{m}$. Although the general tolerance for the ultrasonic machining was quoted as $127\ \mu\text{m}$, all the dimensions were measured within $10\ \mu\text{m}$. Figures 3-12, 3-13, and 3-14 show the pictures of Layer 2, Layer 5, and the exit tube, respectively. Layer 2 was anodically bonded to Layer 1 (refer to Figure 3-11 again), and the exit tube was slip-fitted with Layer 5.

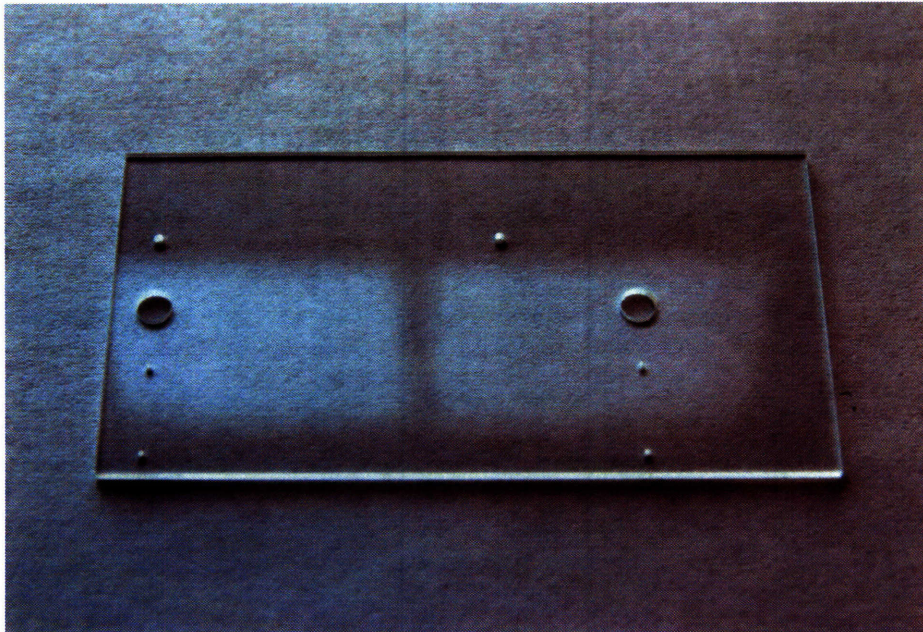


Figure 3-12: Picture of ultrasonically machined Layer 2 (SD-2 glass)

3.3 Preparation of the catalytic inserts

The catalytic inserts were prepared by plating platinum on nickel foams. The nickel foam was purchased from Goodfellow Corporation, and came as a form of $1\ \text{mm}$ -thick sheet that is 94% porous by volume. The foam was cut in the MIT machine shop into a shape of the combustion chamber. To fill the $2\ \text{mm}$ -high combustion chamber, two pieces were stacked together.

The nickel foams were coated with platinum in the MIT Technology Laboratory for Advanced Materials and Structures (TELAMS) following the procedure that was

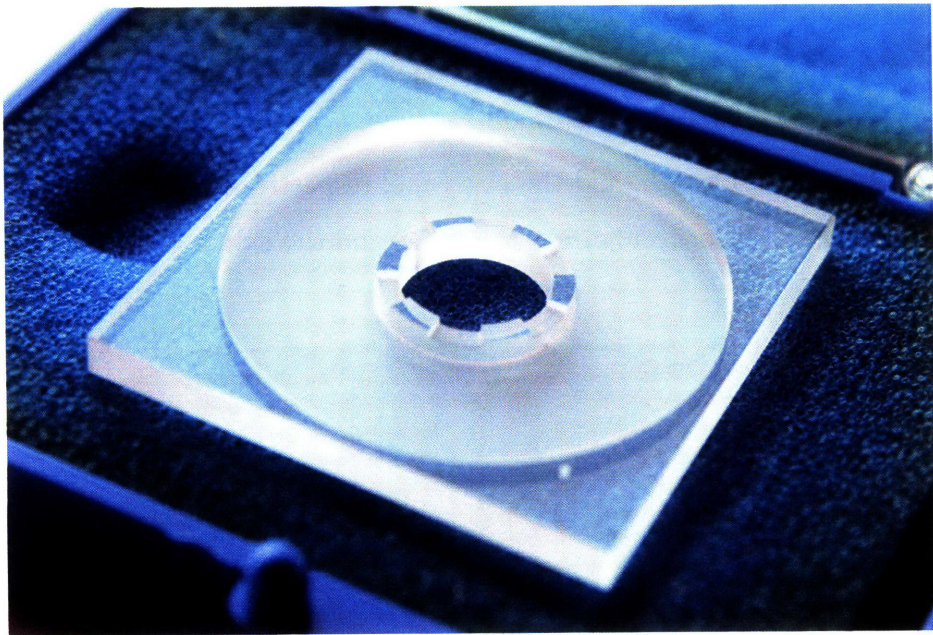


Figure 3-13: Picture of ultrasonically machined Layer 5 (sapphire)



Figure 3-14: Picture of ultrasonically machined exit tube (sapphire)

previously established by Spadaccini [2, 23]:

1. Clean the nickel substrates ultrasonically.
 - Put the nickel substrates in a zipper-top bag filled with soapy water, and put the bag in a ultrasonic bath filled with water.
 - Run the ultrasonic bath for about two hours.
 - Put the substrates in a bag filled with clean de-ionized water, and run for another two hours to rinse.
 - Take out the substrates, and dry them over-night.
2. Dissolve 2.5 g of dihydrogen hexachloroplatinate(IV) salt ($\text{H}_2\text{PtCl}_6 - 6\text{H}_2\text{O}$) into 20 mL of de-ionized water. This makes 12.5% platinate solution.
3. Dip the nickel substrates in the solution for 10 minutes.
4. Dry the substrates in a furnace with reducing environment.
 - Run N_2 at 100°C for 2 hours to remove water.
 - Run H_2 at 300°C for 2 hours to remove Cl.

The catalytic inserts prepared using this procedure are shown in Figure 3-15.

3.4 Experimental setup and diagnostics

Figure 3-16 shows the test stand built to support and provide fluidic connections to the micro-combustor. The micro-machined parts were held together with three spring-loaded ceramic clamps, and the assembly was mounted on the test stand as in Figure 3-17. There are four fluid connections into the experimental apparatus: air (premixed with hydrogen for ignition), fuel, combustor inlet pressure, and combustor exit pressure, each of which is sealed to the test stand with a silicone o-ring.

Three temperature measurements were taken in the locations shown in Figure 2-6 using 0.010 in sheathed type-K thermocouples. Pressures were measured near the

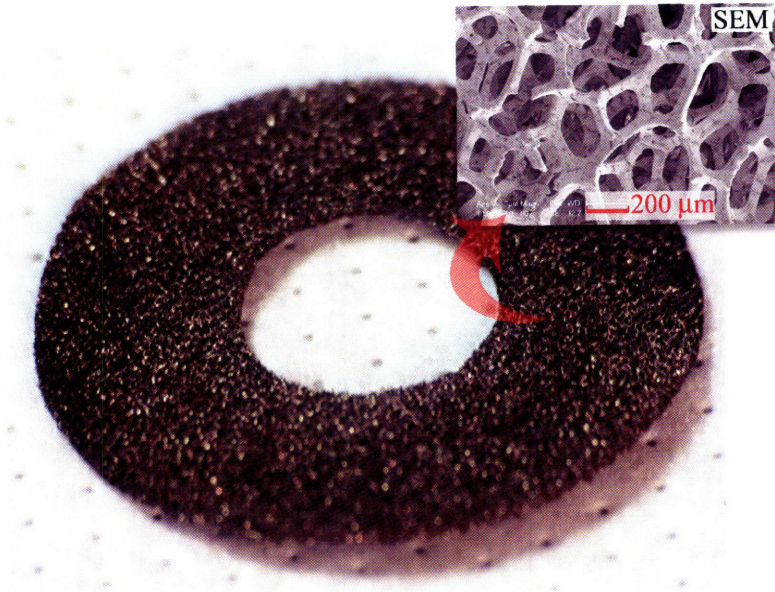


Figure 3-15: Prepared catalytic insert

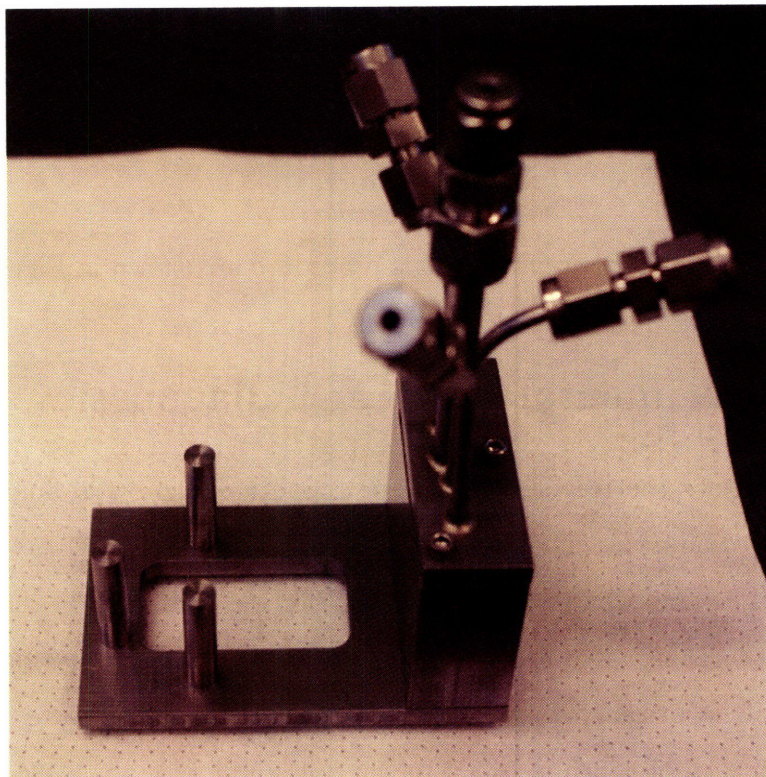


Figure 3-16: Test stand assembly built out of steel

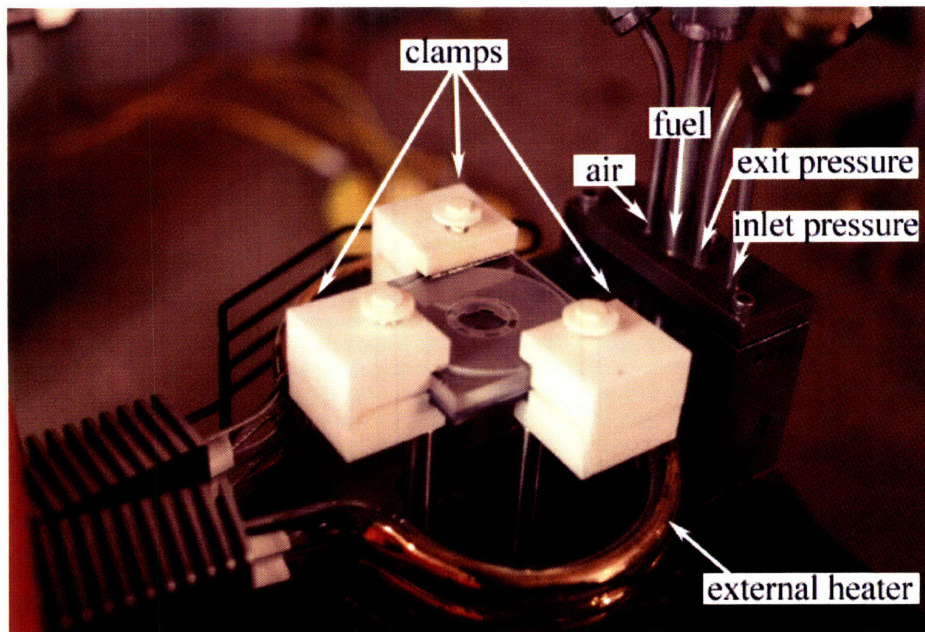


Figure 3-17: Complete test rig

inlet and the exit of the combustion chamber with digital pressure transducers that can measure up to 100 *psi* with a 0.5% accuracy at full-scale. Two MKS 1359C flow controllers were used to control the air and the hydrogen flow. They were calibrated with air and hydrogen, respectively, and had a full-scale accuracy of 0.5%. For JP8 flow control, Porter's liquid flow controller was used. The JP8 flow controller was calibrated with kerosene at the factory, and had the maximum range up to 0.04 *g/sec*. All these data acquisition components were connected to a data acquisition box, NI-SC2345, which eventually transfers the data to a computer. A thermal infrared imaging camera was also used to assist the structural temperature measurement. Figure 3-18 shows a schematic of the test facility. Specifications of each flow controller and diagnostic equipment are listed in Table 3.2.

3.5 Chapter summary

This chapter summarized the fabrication of the liquid-fueled micro-combustor. First, silicon micro-fabrication procedures were described. Photolithography, DRIE, and bonding techniques were discussed. In addition, the ultrasonic machining technique

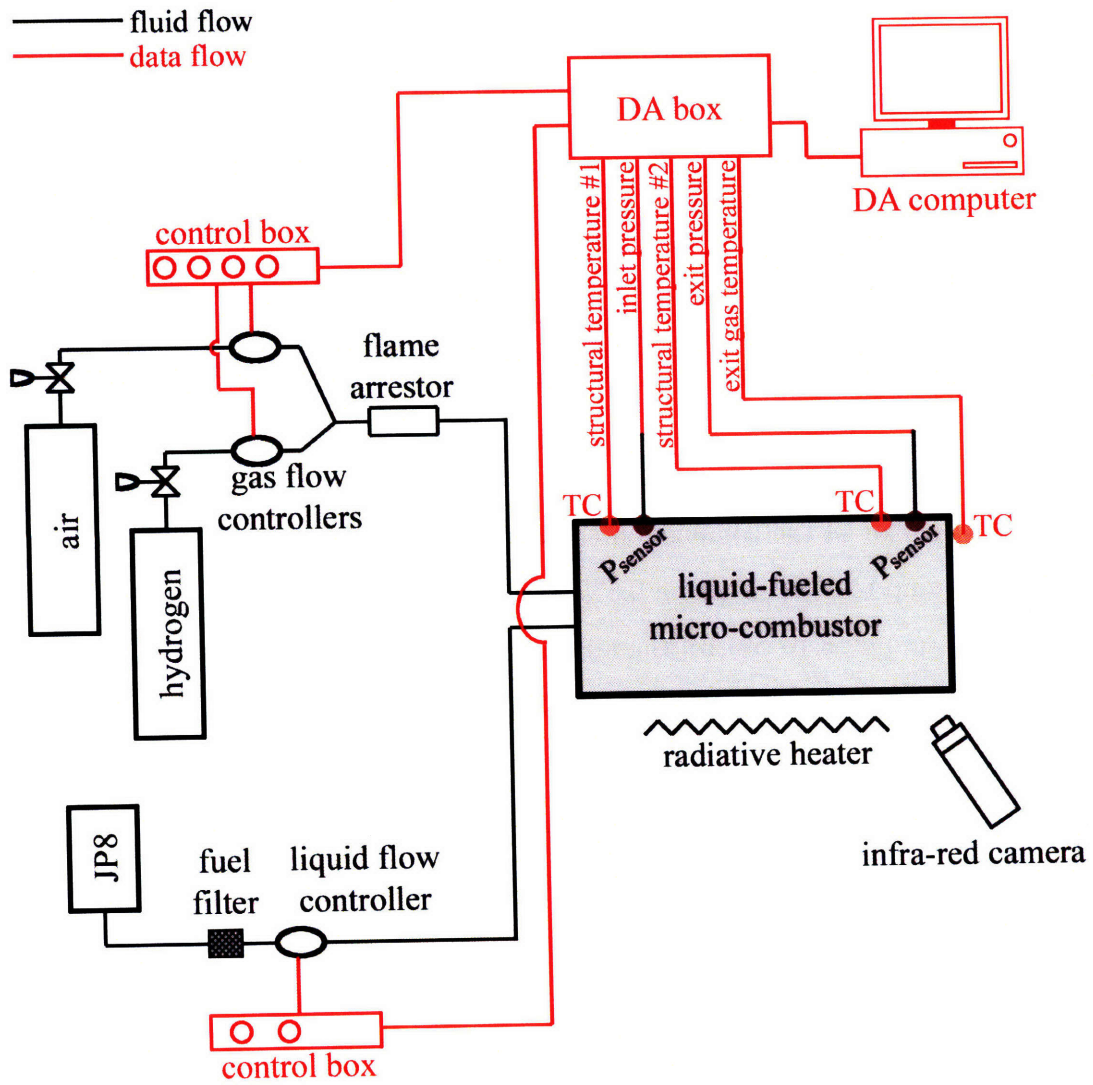


Figure 3-18: Schematic of the experimental facility

Equipment	Model	Specification
air controller	MKS 1359C	10,000 sccm
H ₂ controller	MKS 1359C	2,000 sccm
gas flow control box	MKS Type 247	4-channel
JP8 controller	Porter Liqui-Flow HCB-05-4-C-2	0.04 <i>g/sec</i>
JP8 flow control box	Porter	2-channel
pressure transducer	Omega PX139-100D4V	up to 100 <i>psi</i>
thermocouple	Omega 0.010in type-K	up to 1600 <i>K</i>
thermal infrared camera	inframetrics ThermaCam	
data acquisition box	National Instruments SC-2345	15-channel

Table 3.2: List of equipments in the experimental facility

and the parts fabricated with it were explained. Silicon-to-glass anodic bonding was also reviewed. Preparation of the catalytic inserts by coating nickel substrates with platinum was introduced. Finally, the assembly of the parts and mounting for testing were presented. Experimental setup and diagnostics were explained as well. Experimental characterization of the device will follow in the next chapter.

Chapter 4

Experimental Characterization

Chapters 2 and 3 discussed the design and fabrication of the liquid-fueled micro-combustor, respectively. In this chapter, experimental characterization of the device and the interpretation thereof are presented. Catalytic combustion of JP8 was successfully stabilized in the device, and experimental data were collected under various equivalence ratios and mass flow rates. Two different configurations were tested in the apparatus: one with the entire combustion chamber filled with a catalyst, and the other with just two thirds of the chamber loaded with a catalyst. Temperature and efficiency behaviors for each configuration are presented and compared. The data taken from the test rig were used to construct a non-dimensional operating map. An uncertainty analysis was performed, and 95%-confidence error bars are included in the plots. Details of the uncertainty analysis can be found in Appendix E.

4.1 Ignition procedure of catalytic combustion

To initiate catalytic combustion, the catalyst must be activated first [43]. It is known that platinum becomes activated for hydrocarbon combustion when it is heated to temperatures above 600 K . To achieve this level of preheating, hydrogen is burned in the device prior to switching over to hydrocarbon fuel. For these experiments, the same procedure that was used to initiate earlier catalytic propane combustion experiments [2, 23] was adopted. A typical procedure would be:

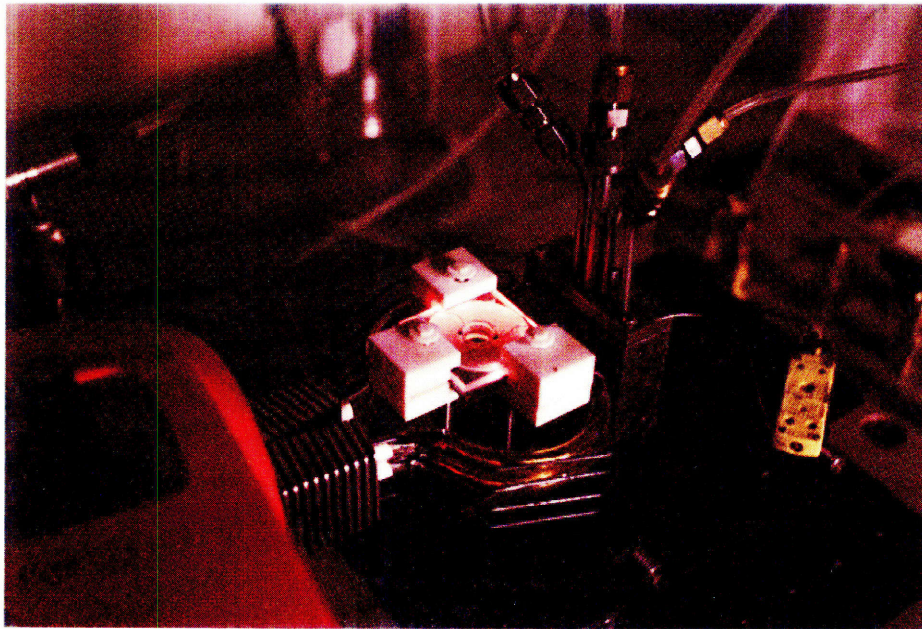
1. Heat the combustor rig with an external heater up to about 450 K .
2. Supply premixed air-H₂ mixture through the air supply channel in the test rig usually at $\dot{m} = 0.02\text{ g/sec}$ and $\phi = 0.7$.
 - The mixture lights off on the platinum surface.
3. When the temperature reaches about 600 K , start the liquid fuel.
 - Temperature rises by about 50 K .
4. Slowly turn H₂ and the heater down and eventually off.

4.2 Catalytic JP8 combustion

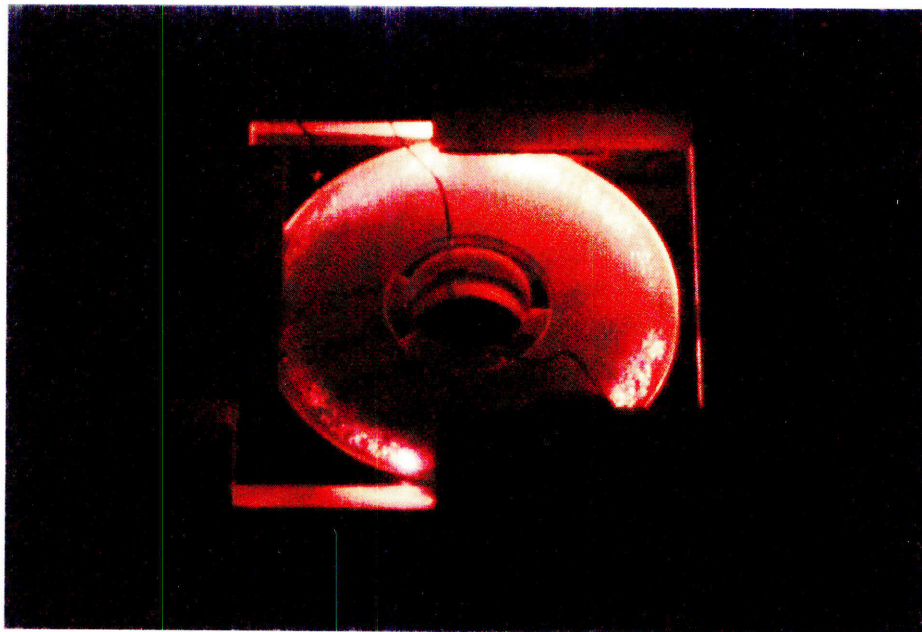
Following the ignition procedure explained in Section 4.1, JP8 fuel was combusted successfully in the experimental apparatus. Catalytic combustion can be characterized by bright glowing of the catalytic insert in orange color as shown in Figure 4-1. Figure 4-2 was taken by a thermal infrared imaging camera, and illustrates the temperature profile of the combustor. It shows that the hottest part of the device is around the inlet of the combustion chamber. The thermal infrared imaging camera measurement depends on a complicated calibration, which was not available, so its use was limited to showing qualitative trends.

4.2.1 Temperature response

The temperature response of catalytic JP8 combustion is plotted in Figures 4-3 and 4-4. Temperature measurements are obtained by using *10-mil* unsheathed type-K thermocouples. As shown in Figure 2-6, the exit gas temperature is measured at the exit nozzle, and the structural temperatures are measured around both the outer rim and the exit of the combustion chamber. The two structural temperature measurements differed by less than 10 K , which is within the 95%-confidence uncertainty range. As included in each figure, 95%-confidence uncertainty for the exit gas temperature measurements is $\pm 32\text{ K}$, and $\pm 12\text{ K}$ for the structural temperature.



(a)



(b)

Figure 4-1: Photograph of the JP8 combustor in operation (a) and a zoomed view (b)

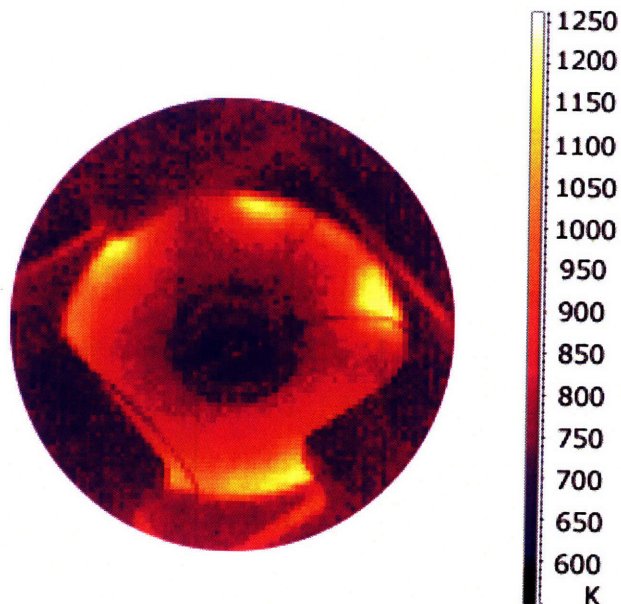


Figure 4-2: Thermal infrared image of the liquid-fueled micro-combustor during JP8 combustion ($\phi = 1.1$, $\dot{m} = 0.1 \text{ g/sec}$)

Figure 4-3 shows the exit gas temperature as a function of the equivalence ratio for each mass flow rate setting. Although measured data lie within the uncertainty bands of one another, a higher mass flow rate generally resulted in a higher temperature at the same equivalence ratio. Catalytic JP8 combustion was stabilized at equivalence ratios as low as 0.7 and as high as 1.4. Whereas there is normally a peak around the equivalence ratio of 1.0 for gas-phase combustion, no peak was observed in this experiment. This is because fuel conversion efficiency is low, and the combustion is limited by the diffusion of the fuel. The higher the concentration of the fuel molecules is, the higher the diffusion rate becomes, and more fuel can be burned, producing higher temperature.

Figure 4-4 shows the exit gas temperature and the structural temperature as functions of the mass flow rate. The structural temperature plotted is an average between the two structural temperature measurements. JP8 combustion was stabilized at a mass flow rate as high as 0.1 g/sec (Figure 4-4), and the corresponding exit gas temperature was 780 K ($\phi = 1.1$). In general, the temperatures increase with the mass flow rates, which indicates that the performance of the combustor is not limited by

chemical efficiencies in this range, showing a potential to allow a higher mass flow rate. However, the design mass flow rate of 0.3 g/sec was not achieved because of a structure failure, which is believed to be due to excessive thermal stresses in the sapphire. There is little difference between the exit gas temperatures and the structural temperatures, which is typical for catalytic combustion [43]. This is because the chemical reactions occur on the catalytic surfaces, and the heat is transferred to the bulk gas via convection (heat transfer by radiation becomes significant when the catalyst temperature exceeds 800 K). Due to the existence of short conduction paths with relatively small thermal resistance between the catalytic insert and the sapphire structure, the heat tends to readily flow from the catalyst to the structure, resulting in high structural temperatures.

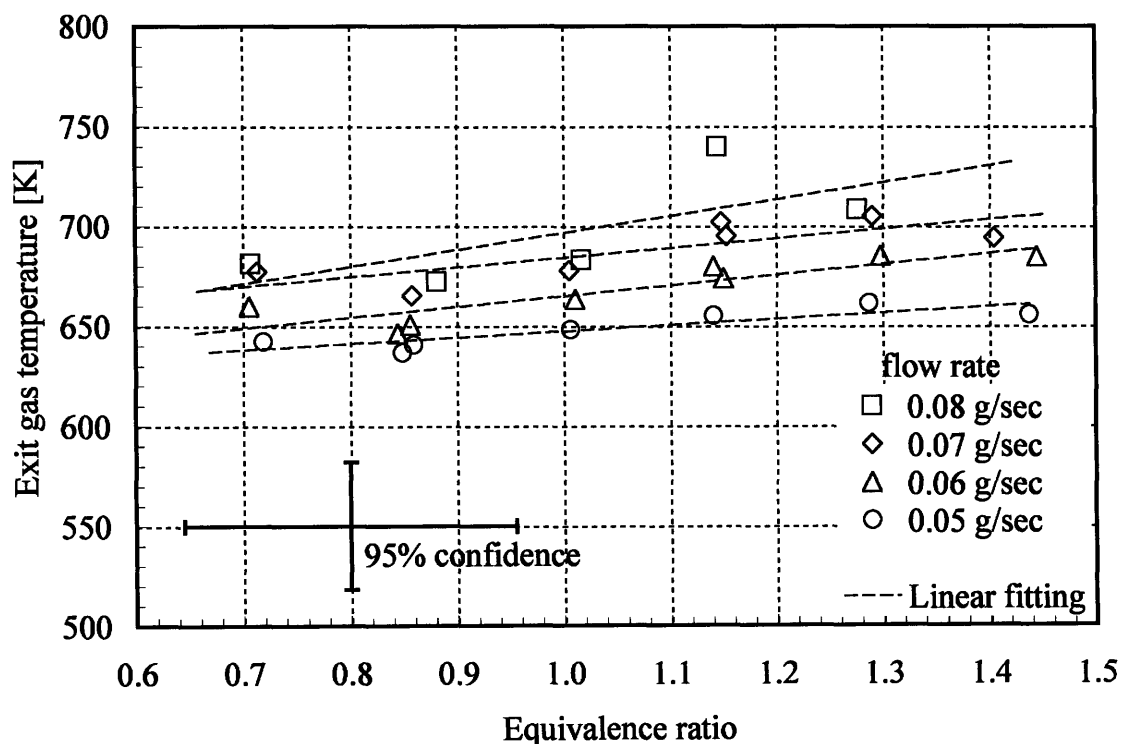
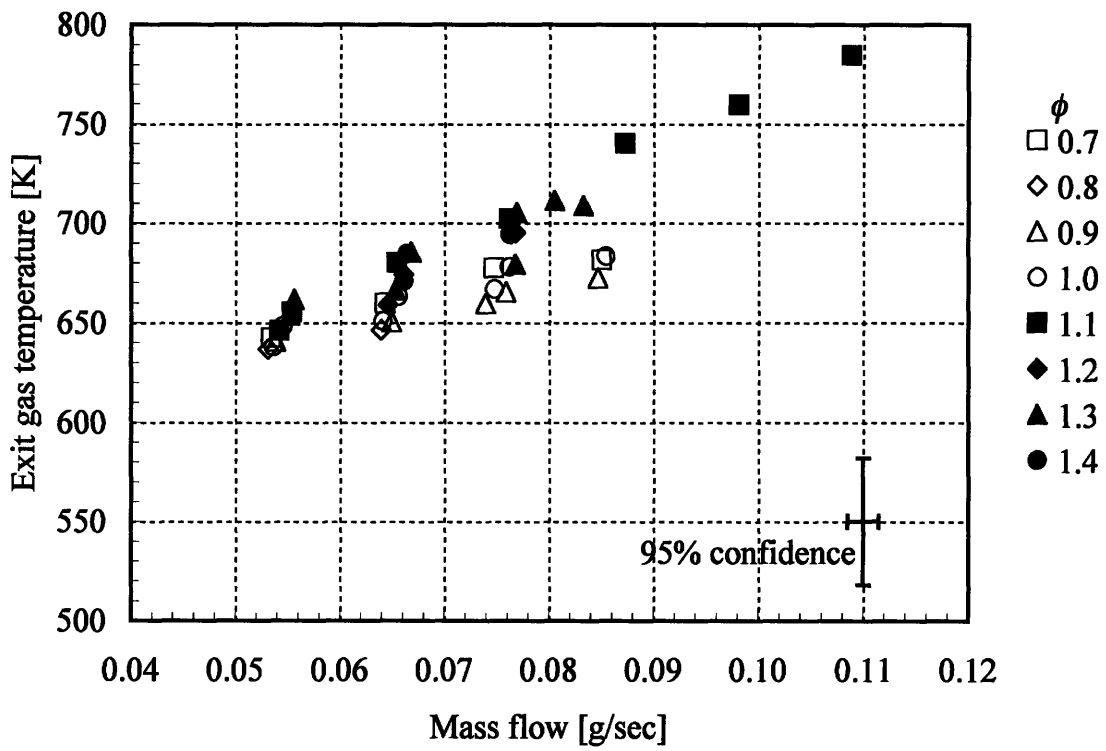
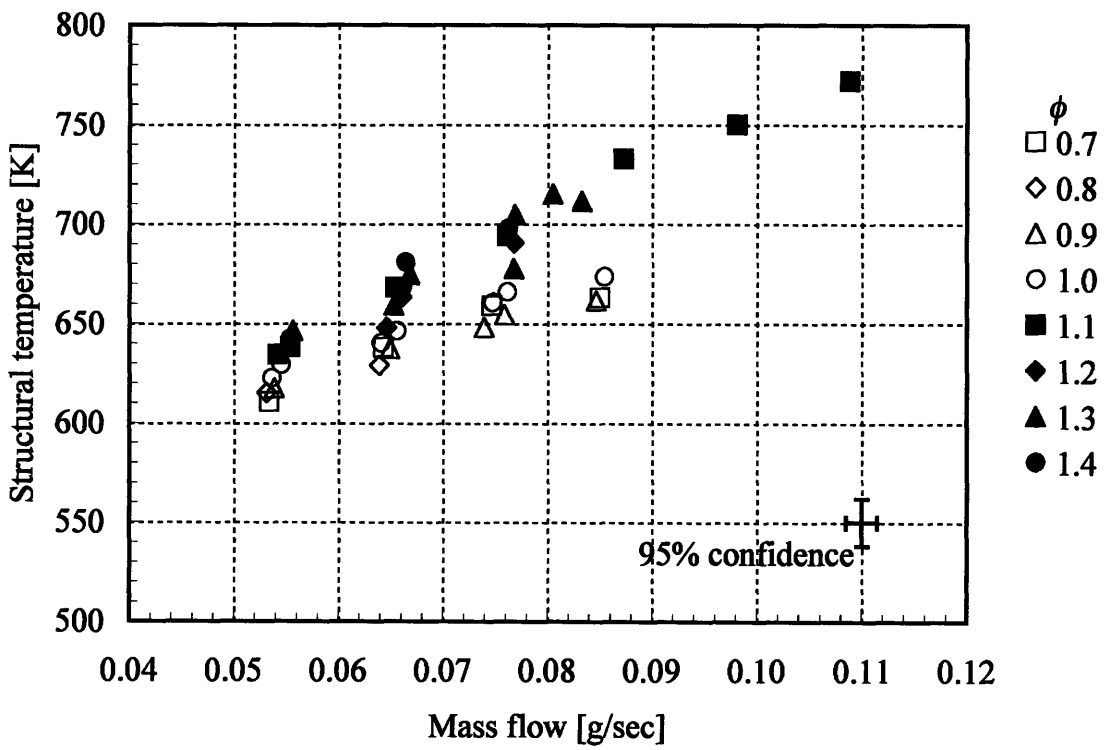


Figure 4-3: JP8 combustion result: exit gas temperature vs. equivalence ratio for different mass flow rates



(a)



(b)

Figure 4-4: JP8 combustion result: exit gas temperature (a) and structural temperature (b) vs. mass flow rate for different equivalence ratios

Based on the temperature data, the power density can be calculated by:

$$\begin{aligned} \text{Power density} &= \frac{\text{fluid power}}{\text{combustor volume}} \\ &= \frac{(\dot{m}_a + \dot{m}_f)h_{exit} - \dot{m}_a h_{inlet}}{V} \end{aligned} \quad (4.1)$$

In the device, the mass flow rate was limited to 0.1 g/sec , due to a structure failure, and the corresponding exit gas temperature was 780 K . Therefore, the maximum power density achieved was somewhat low at 43 MW/m^3 .

4.2.2 Efficiency breakdown

From the experimental measurements, the overall combustor efficiency can be calculated by dividing the enthalpy gain of the fluid by the maximum possible fuel power that may be released [56]:

$$\eta_{overall} = \frac{(\dot{m}_a + \dot{m}_f)h_{exit} - \dot{m}_a h_{inlet}}{\dot{m}_f h_f} \quad (4.2)$$

where \dot{m}_a and \dot{m}_f are the mass flow rates of air and fuel respectively, h_{inlet} and h_{exit} are the specific enthalpies¹ at the inlet and the exit, and h_f the lower heating value of JP8. Using the structural temperature data, it can be estimated how much heat is lost through the device (more details on the heat loss estimation can be found in Appendix D). Adding the heat loss to the enthalpy gain of the fluid gives the total amount of heat that has been released from the fuel. Dividing the total heat release by the maximum fuel power that could have been released yields the chemical efficiency:

$$\eta_{chemical} = \frac{[(\dot{m}_a + \dot{m}_f)h_{exit} - \dot{m}_a h_{inlet}] + q_{loss}}{\dot{m}_f h_f} \quad (4.3)$$

¹ $dh = C_p dT$. For ease of computation, values of C_p were evaluated as if the working fluid is pure air, which is obviously not the case. This assumption generally under-predicts C_p by about 15% compared to the more rigorously estimated C_p of the combustion reactants and products. So, there are uncertainties in the efficiency calculations associated with this simplification. Detailed uncertainty analysis is included in Appendix E.

Dividing the overall combustor efficiency by the chemical efficiency, it can be estimated how much heat is retained in the fluid as opposed to how much heat has been released from the fuel. This is defined as the thermal efficiency:

$$\eta_{thermal} = \frac{(\dot{m}_a + \dot{m}_f)h_{exit} - \dot{m}_a h_{inlet}}{[(\dot{m}_a + \dot{m}_f)h_{exit} - \dot{m}_a h_{inlet}] + q_{loss}} \quad (4.4)$$

These efficiency components are plotted in Figure 4-5 for the equivalence ratio of 1.1. As seen in Figure 4-4 (a), the exit gas temperature keeps rising with the mass flow rate until the structural failure; more fluid power is generated as the mass flow rate goes up. Therefore, the overall combustor efficiency increases with the mass flow rate. In Figure 4-4 (b), likewise, higher mass flow rates lead to higher structural temperatures and thus more heat losses. Hence, the chemical efficiency increases with the mass flow rate as well. This implies that the device is not chemically-limited in this mass flow rate range, showing that it could potentially be operated at higher mass flow rates if the structure bears the thermal load. Shorter residence time caused by the increased mass flow rate is still sufficient for combustion, and the high combustion temperature leads to faster diffusion of the fuel species, augmenting the chemical efficiency. The thermal efficiency increasing with the mass flow rate is a common trend in the micro-combustor.

4.2.3 Non-dimensional operating map

It is critical in catalytic combustion to ensure that the fuel-air mixture stays in the combustion chamber longer than it takes for the fuel molecules to diffuse through the boundary layer and onto the catalytic surfaces, on which they react with oxygen. Therefore, it is informative to analyze the performance of the liquid-fueled micro-combustor using the Peclet number. The Peclet number is a non-dimensional parameter defined as the ratio between the characteristic flow residence time and the characteristic diffusion time of fuel molecules:

$$Pe = \frac{\tau_{res}}{\tau_{dif}} \quad (4.5)$$

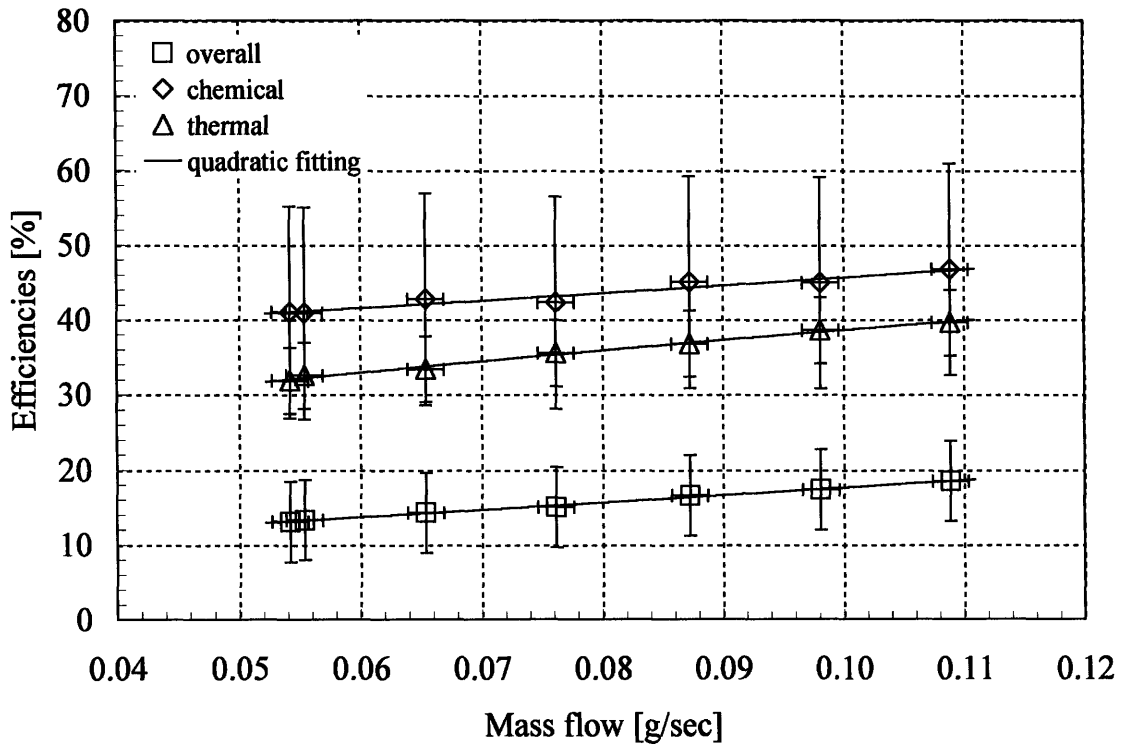


Figure 4-5: JP8 combustion result: efficiency breakdown for $\phi = 1.1$

A large Peclet number means the residence time-scale is sufficiently long compared to the fuel diffusion time. At low mass flow rates, large Peclet numbers are typical. As the flow rate is increased, however, the flow residence time becomes smaller; the Peclet number goes down unless the fluid temperature increases appreciably to augment diffusion and thus reduce the diffusion time-scale.

To evaluate the Peclet number, the flow residence time-scale is first calculated with a density based on the average temperature²:

$$\begin{aligned}
 \tau_{res} &= \frac{\rho V}{\dot{m}} \\
 &= \frac{PV}{\dot{m}R\bar{T}}
 \end{aligned}
 \tag{4.6}$$

where P is the combustor pressure, V the combustor volume, \dot{m} the total mass flow rate, R the gas constant for air, and \bar{T} the average temperature in the combustion

² $\bar{T} = \frac{T_{inlet} + T_{exit}}{2}$. The validity of using this average was demonstrated by Mehra [1]

chamber. Recalling Equation (2.12) in Chapter 2,

$$\frac{d(TC_b)}{dt} = -\frac{Sh_D D_{ab}}{R^2} (TC_b)$$

Upon using the average temperature and molecular diffusion coefficient, which is evaluated based on the average temperature, Equation (2.12) integrates to:

$$\frac{C_b(t)}{C_b(0)} = e^{-\frac{Sh_D \bar{D}_{ab}}{R^2} t} \quad (4.7)$$

Since the diffusion time-scale is defined as the time that the fuel concentration becomes 10% of the initial concentration:

$$e^{-\frac{Sh_D \bar{D}_{ab}}{R^2} \tau_{dif}} = 0.1 \quad (4.8)$$

Thus,

$$\begin{aligned} \tau_{dif} &= -\frac{R^2 \ln(0.1)}{Sh_D \bar{D}_{ab}} \\ &= \frac{2.30 R^2}{Sh_D \bar{D}_{ab}} \end{aligned} \quad (4.9)$$

Substituting \bar{D}_{ab} by the Fuller correlation (Equation (2.9)):

$$\tau_{dif} = \left(\frac{2.30 R^2 (v_a^{1/3} + v_b^{1/3})^2}{1.013 \times 10^{-2} Sh_D \sqrt{1/M_a + 1/M_b}} \right) \frac{P}{\bar{T}^{1.75}} \quad (4.10)$$

Using the temperature and the mass flow rate measurements for each experimental data point, the corresponding Peclet number can be computed by dividing Equation (4.6) by Equation (4.10):

$$Pe = \left(\frac{1.013 \times 10^{-2} V Sh_D \sqrt{1/M_a + 1/M_b}}{2.30 R R^2 (v_a^{1/3} + v_b^{1/3})^2} \right) \frac{\bar{T}^{0.75}}{\dot{m}} \quad (4.11)$$

The Peclet numbers, evaluated based on the experimental measurements including

\bar{T} and \dot{m} , are plotted versus the mass flow rate in Figure 4-6. As stated earlier, the Peclet number decreases with the mass flow rate mainly due to the reduction in the flow residence time. Its dependency on temperature is weak relative to mass flow rate, so the Peclet number is only a weak function of equivalence ratio in the liquid-fueled micro-combustor.

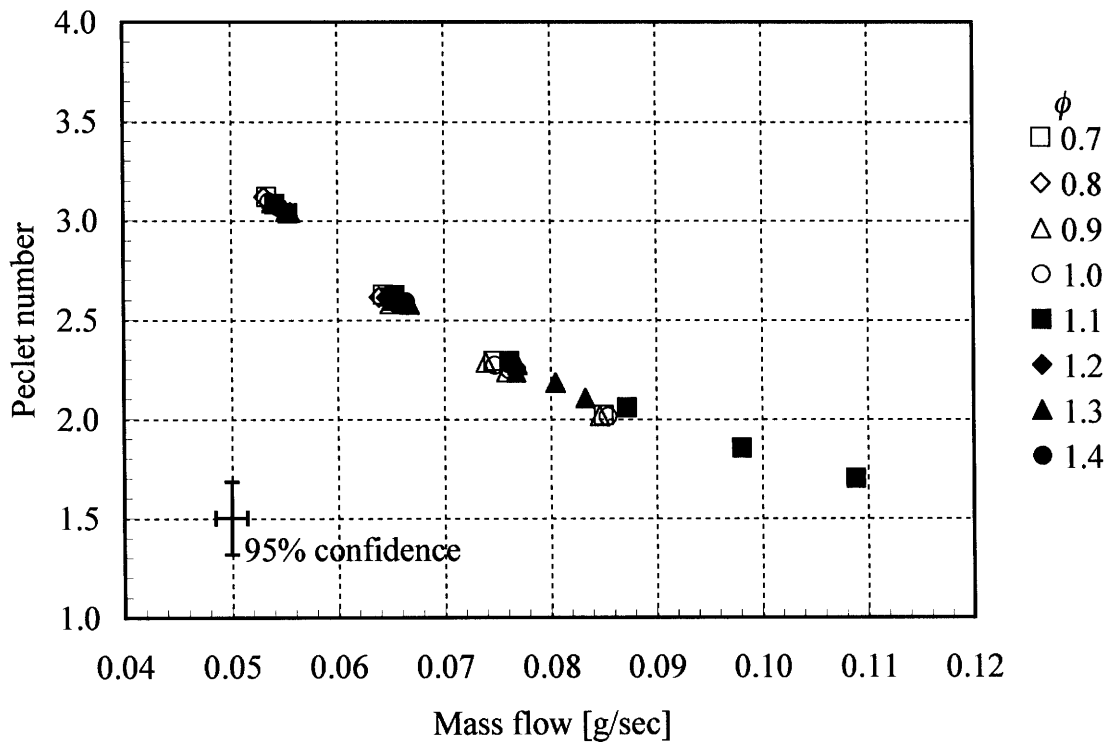


Figure 4-6: JP8 combustion result: Peclet number vs. mass flow rate

These experiment-based Peclet numbers are mapped out on a non-dimensional space in Figure 4-7. The vertical axis represents the chemical efficiency, and the horizontal axis represents the thermal efficiency. The product of the two is the overall efficiency and is represented by the curvilinear axis in the plot area. All the experimental data are plotted in the chemical efficiency-thermal efficiency plane, and each data point has a corresponding Peclet number although the exact value is not marked in the plot for the sake of legibility. Instead, shown in Figure 4-7 are the lines of constant Peclet numbers, which were generated by fitting the experiment-based Peclet

numbers with the least square method³. The average error⁴ of the least square fitting was 12.4%.

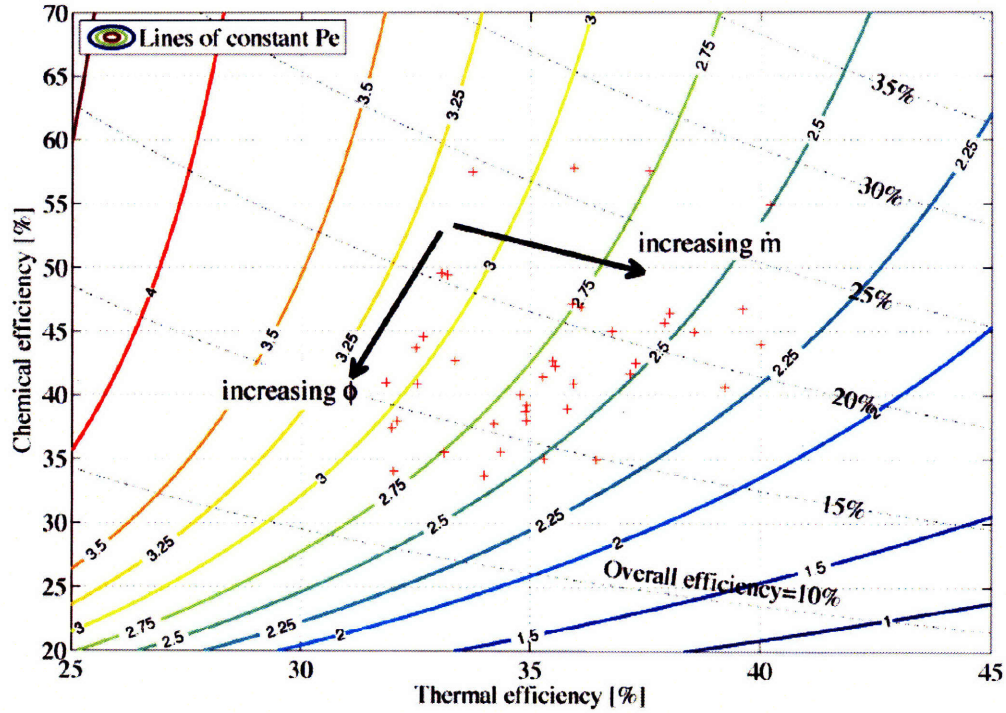


Figure 4-7: JP8 combustion result: lines of constant Peclet numbers on a chemical efficiency and thermal efficiency plane

To better understand the non-dimensional operating map, the chemical efficiency and the thermal efficiency were plotted as functions of the Peclet number in Figure 4-8. Although there are broad uncertainty bands, Figure 4-8 displays a few general trends. First, high Peclet numbers generally result in low thermal efficiencies. This is because high Peclet numbers represent low mass flow rates (Figure 4-6), and the thermal efficiencies have a tendency to increase with the mass flow rate as shown in Figure 4-5. The impact of the Peclet number on chemical efficiencies is rather unclear in this plot. However, it can be said that low Peclet numbers do not significantly reduce the

³After inspecting the trend of the Peclet number distribution, a form of $Pe = \frac{a}{\eta_{thermal}} + \frac{b}{\eta_{chemical}}$ was used, then coefficients a and b were determined by the least square method.

$${}^4Err = \sqrt{\frac{1}{n} \sum_{k=1}^n \left[\frac{Pe_k - \left(\frac{a}{\eta_{thermal,k}} + \frac{b}{\eta_{chemical,k}} \right)}{Pe_k} \right]^2}$$

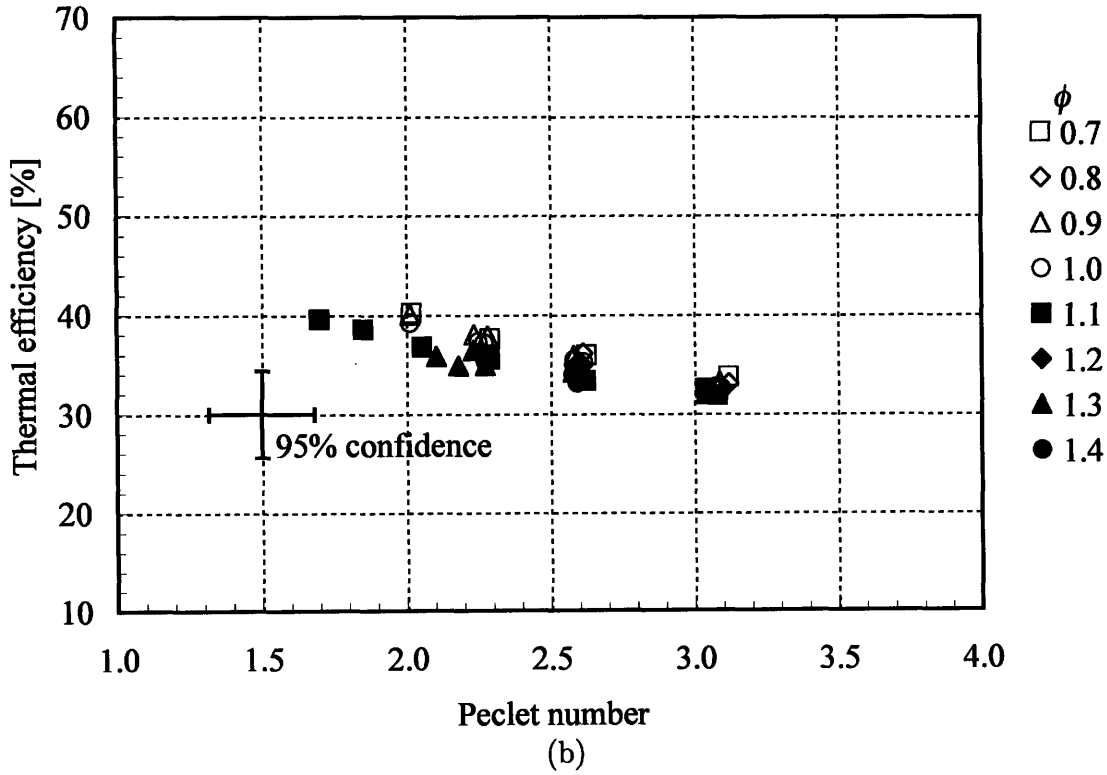
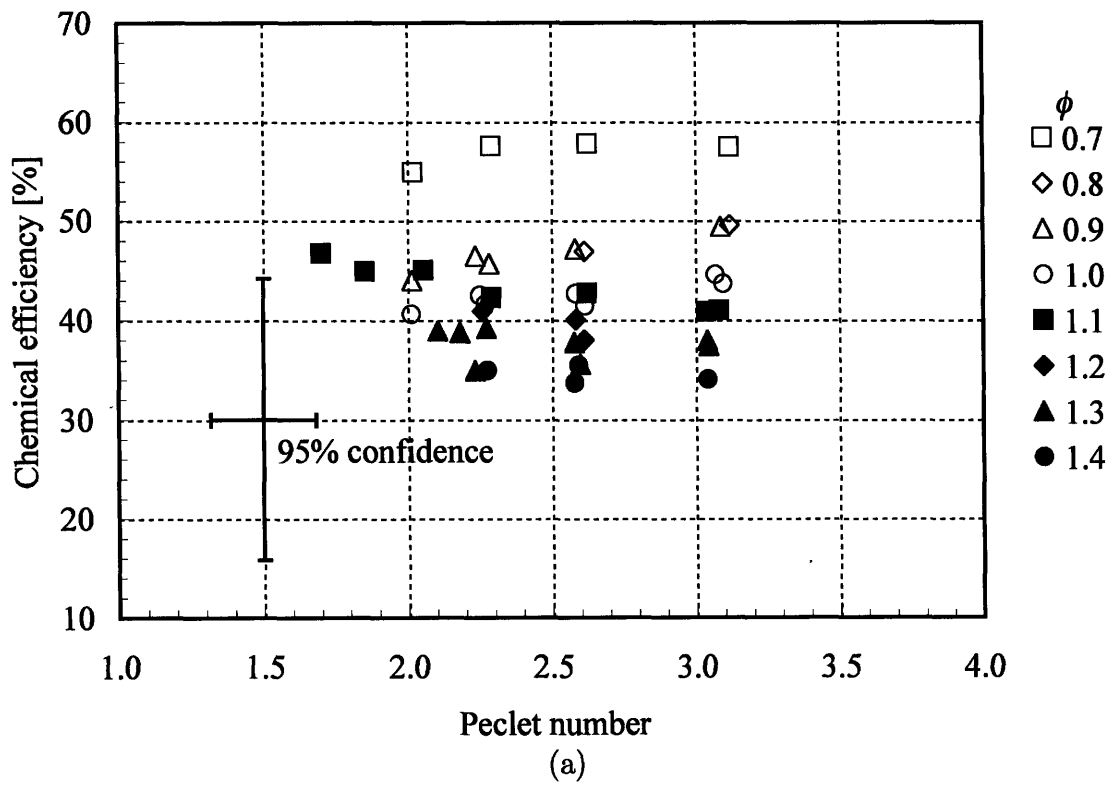


Figure 4-8: JP8 combustion result: chemical efficiency (a) and thermal efficiency (b) vs. Peclet number

chemical efficiency, which suggests that the device is not chemically-limited in this mass flow rate range, i.e. the device has enough catalyst in the combustion chamber.

Second, chemical efficiencies appear to go down as the equivalence ratio is increased, whereas thermal efficiencies are not influenced by the equivalence ratio. This is likely because the thermal efficiency represents the heat transfer characteristics of the device, and no chemistry is associated with it. On the other hand, the chemical efficiency renders how effectively the combustor can convert the fuel, so properties such as the fuel concentration (equivalence ratio) are important. Other parameters that may impact the efficiencies, e.g. catalyst geometry, fuel's diffusion characteristics, pressure, temperature, and mass flow rate, are lumped in the Peclet number. Figure 4-9 diagrammatically explains how all the relevant parameters can be grouped into non-dimensional parameters. The chemical efficiency is a function of the Peclet number and the equivalence ratio, and the thermal efficiency is a function of the Peclet number and the thermal boundary conditions (fluid-structure interaction characteristics) of the specific device. Therefore, this non-dimensional operating map is device-specific. However, unless the thermal boundary conditions are altered drastically, the map can also be used to predict the performance of a catalytic micro-combustor with different fuel or volume to some limited extent, making it possible to use the map as a design tool. Section 4.5 will discuss this in more detail.

It is these tendencies that make Figure 4-7 look as it does. Increase in the equivalence ratio moves the operating point to the bottom of the map. As seen in Figure 4-6, the Peclet number is inversely proportional to the mass flow rate, so increasing the mass flow rate pushes the operating point mainly to the right and slightly to the bottom.

4.3 Catalytically-anchored gas-phase combustion

Although the use of a catalytic insert extends the mass flow rate capability, exit gas temperatures tend to be lower than for gas-phase combustion. Moreover, the exit gas temperature requirement of 1300 K is so close to platinum's melting point that the

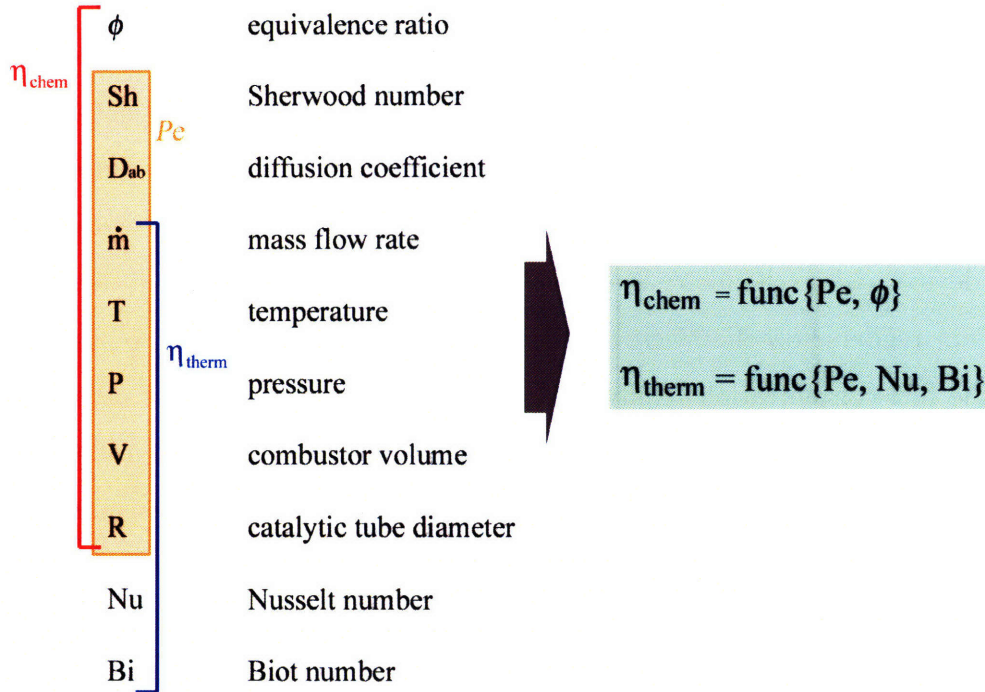


Figure 4-9: Relevant parameters divided into non-dimensional parameters

structural integrity of the catalytic insert becomes an issue for the catalytic micro-combustor. Therefore, a concept of catalytically-anchored gas-phase combustion, or hybrid combustion, was suggested [2]. This concept has been adopted in many conventional gas turbine combustors, especially in ground-based power generators, due to advantages in ignition, stability, and emissions [57, 58, 59, 60, 61]. Because the flammability limit of hydrocarbon fuels is rather narrow around the stoichiometric equivalence ratio, conventional gas-phase combustors have a fuel-rich primary zone followed by a diluted secondary zone, which cools down the combustion product with dilution air to a safe operating temperature of the turbine. Due to elevated combustion temperatures, the primary zone produces much NO_x emissions. Unlike conventional applications, however, the concept of catalytically-anchored gas-phase combustion was proposed for the liquid-fueled micro-combustor to achieve both high reaction rates and high exit gas temperature without jeopardizing the catalyst. To test this configuration, only the front two thirds of the combustor volume, instead of the entire combustor, was filled with a catalytic insert.

4.3.1 Temperature response

JP8 combustion was stabilized in the device at a mass flow rate as high as 0.2 g/sec , at which point the combustion blew out. Figure 4-10 shows the temperature response from the experiment. Unlike the fully-loaded catalytic combustor results, there is a fairly large discrepancy between the exit gas temperature and the structural temperature, suggesting that this configuration can provide better thermal isolation of the combustion chamber and, thus higher thermal efficiencies. The efficiency breakdown will be discussed in the next section. The maximum exit gas temperature obtained was 723 K ($\dot{m} = 0.07\text{ g/sec}$), and due to extended mass flow rate, the maximum power density was 54 MW/m^3 ($\dot{m} = 0.2\text{ g/sec}$), the best achieved in the device. However, the operational requirement of 1300 K was still not met. It appears that the combustion has not transitioned to gas-phase combustion even though the fuel-air mixture was at a temperature higher than the gas-phase autoignition temperature (typically 520 K at 1 atm). This inhibition of gas-phase ignition has been reported by other researchers, including Dupont [62] and Griffiths [63]. Using methane, Dupont *et al.* found that heterogeneous catalytic combustion prevailed up to 1400 K . The inhibition of gas-phase ignition was attributed to the depletion of fuel species in the gas. Griffiths *et al.* explained the inhibition to be also associated with water vapor desorbed from the catalytic surfaces. The large amount of water vapor prevents favorable conditions for gas-phase ignition by catalyzing reaction paths that consume the free radicals H and CH_3 , and form more stable species such as HO_2 and C_2H_6 .

4.3.2 Efficiency breakdown

Figure 4-11 shows the overall, chemical, and thermal efficiencies as functions of the mass flow rate for an equivalence ratio of 0.9. The large difference between the exit gas temperature and the structural temperature, as noted in the previous section, results in enhanced thermal efficiency. Since conductive heat transfer from the catalytic insert to the structure is reduced due to smaller contact area, heat can be retained in the fluid better. However, due to inhibition of gas-phase ignition, the non-catalytic portion of

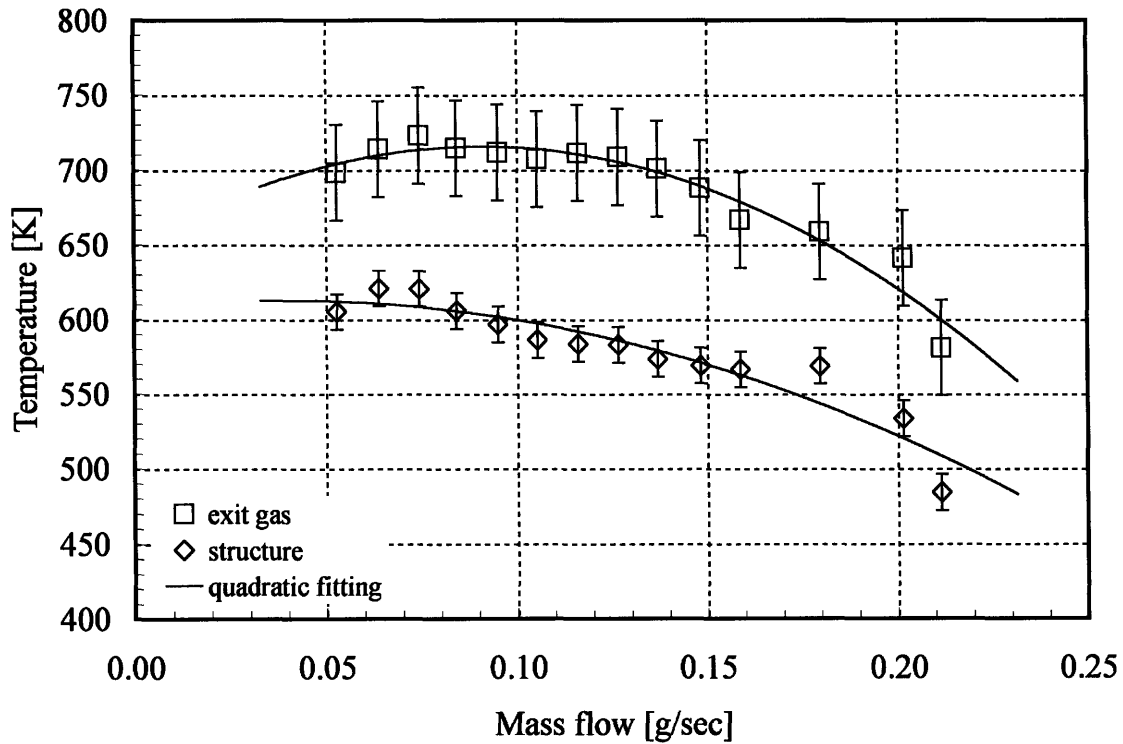


Figure 4-10: Partially-loaded catalytic micro-combustor result: temperatures vs. mass flow rate for $\phi = 0.9$

the combustion chamber cannot be actively used, which results in the reduction of the effective volume of the catalytic combustor. Therefore, the performance of the combustor is chemically-limited at high mass flow rates, i.e. the chemical efficiency declines with the mass flow rate, and eventually the reactions are blown out. This will be discussed in more detail using non-dimensional parameters in the next section.

4.4 Device comparison

In this section, the results from the partially-loaded catalytic combustor are compared with the fully-loaded catalytic combustor results. As discussed in the previous section, the partially-loaded catalytic combustor has relatively high exit gas temperatures and low structural temperatures. Figure 4-12 depicts these trends. This result is attributed to different components of the efficiencies. As seen in Figure 4-13, the

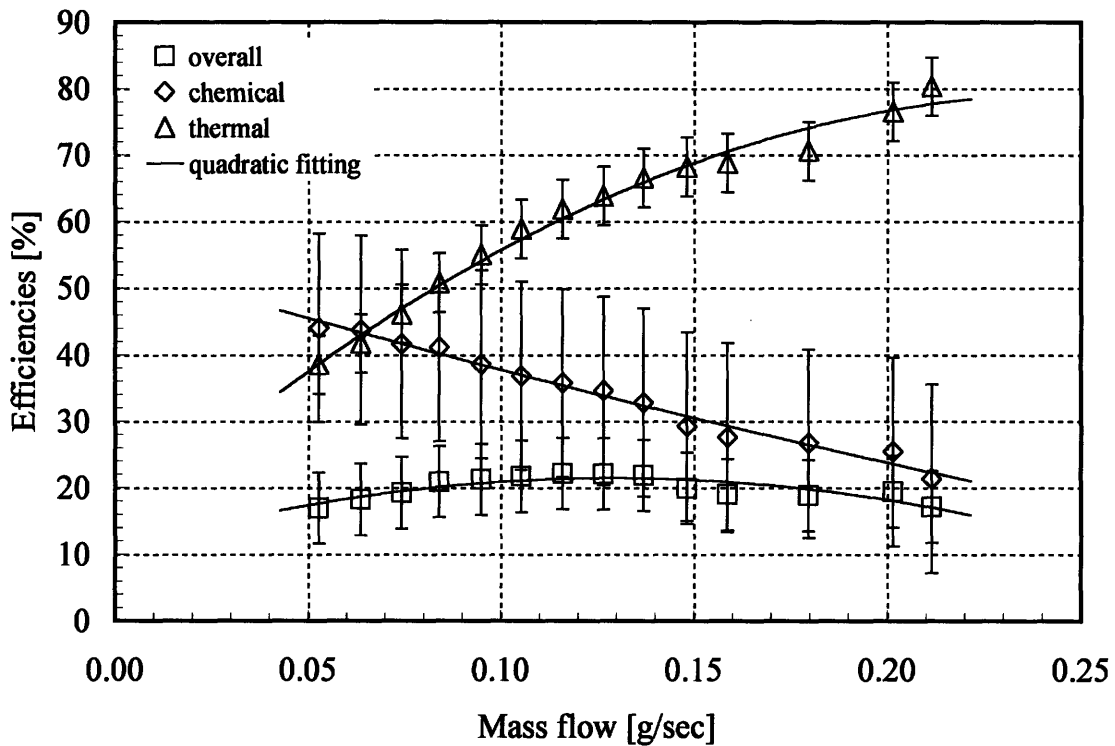
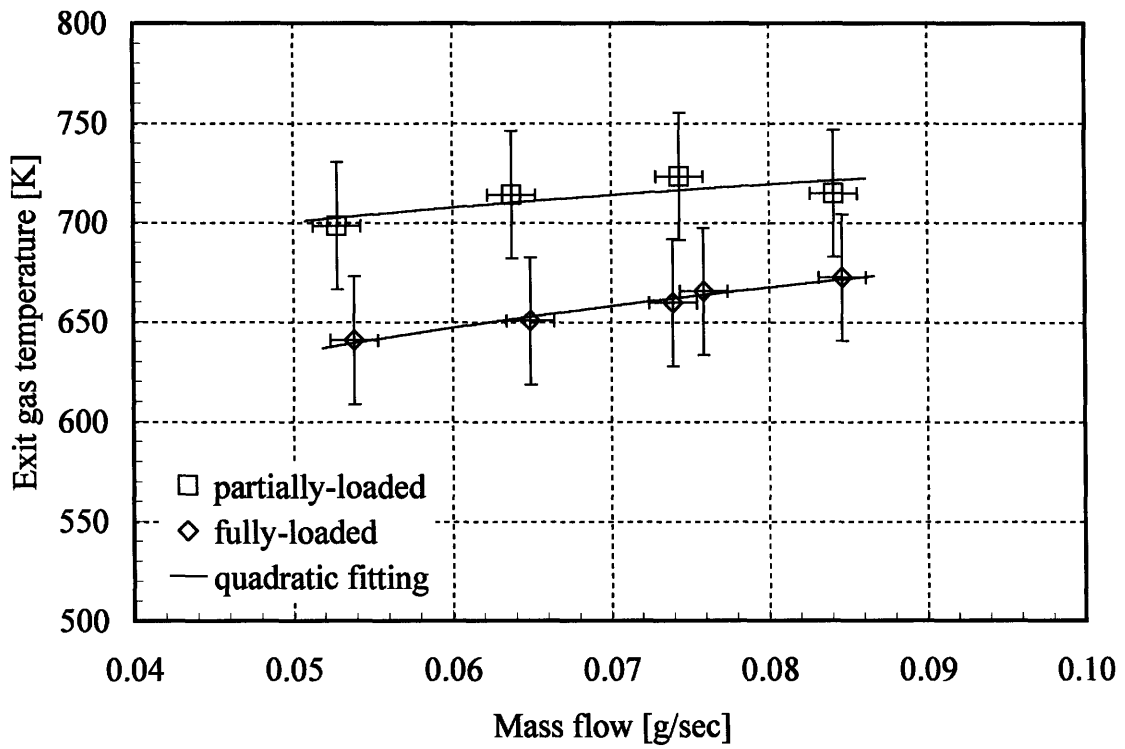


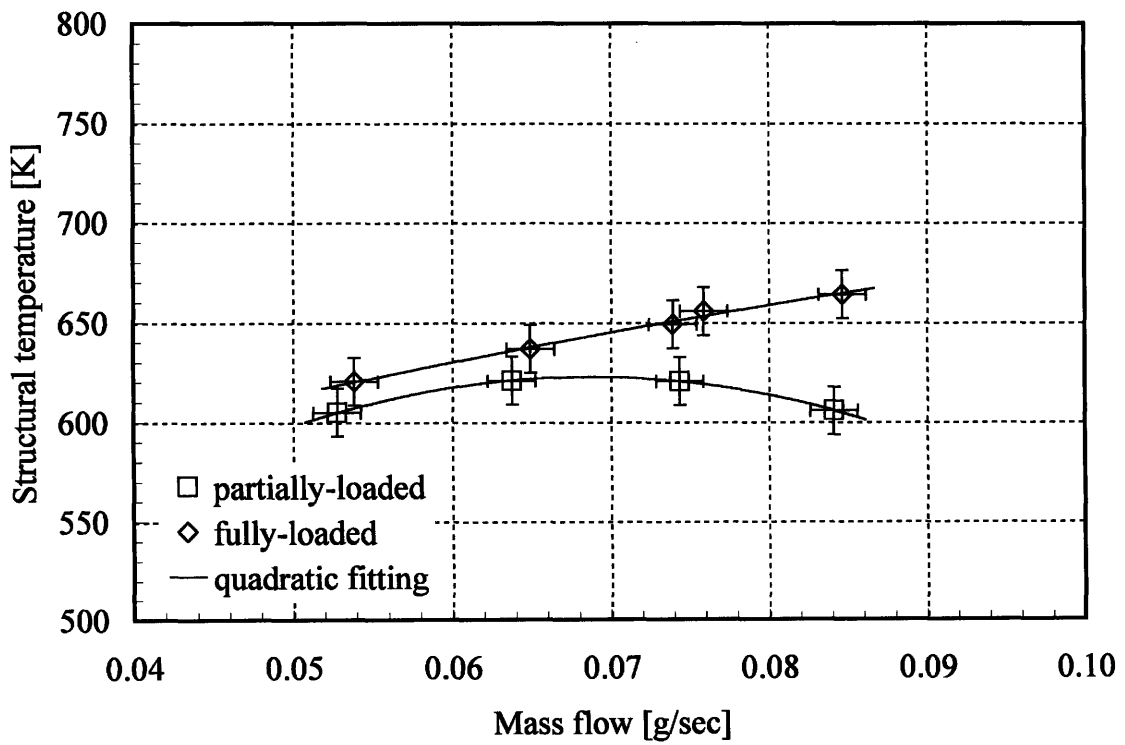
Figure 4-11: Partially-loaded catalytic micro-combustor result: efficiencies vs. mass flow rate for $\phi = 0.9$

fully-loaded catalytic device has lower overall efficiencies even though it has higher chemical efficiencies. This is due to much lower thermal efficiencies. In other words, the fully-loaded catalytic device has more catalyst in it, so it can combust more fuel. However, due to the presence of a large contact area between the catalyst and the sapphire structure, it loses more heat, and the overall efficiency becomes low.

To view this from a different perspective, Figure 4-14 was generated. It shows the chemical efficiencies of the fully-loaded catalytic device and the partially-loaded device for the equivalence ratio of 0.9. Besides the two solid curves for each device, a new curve was generated, and is shown in a broken line. This additional curve plots the chemical efficiency of the partially-loaded device against the Peclet number, but the Peclet number was recalculated based on a volume that is occupied by the catalyst (1 cc), not the entire combustion chamber (1.4 cc). Then, the new curve fits quite well with the fully-loaded device. This appears to indicate that the reduction of the catalyst caused the effective combustor volume to decrease.



(a)



(b)

Figure 4-12: Device comparison: exit gas temperatures (a) and structural temperatures (b) vs. mass flow rate for $\phi = 0.9$

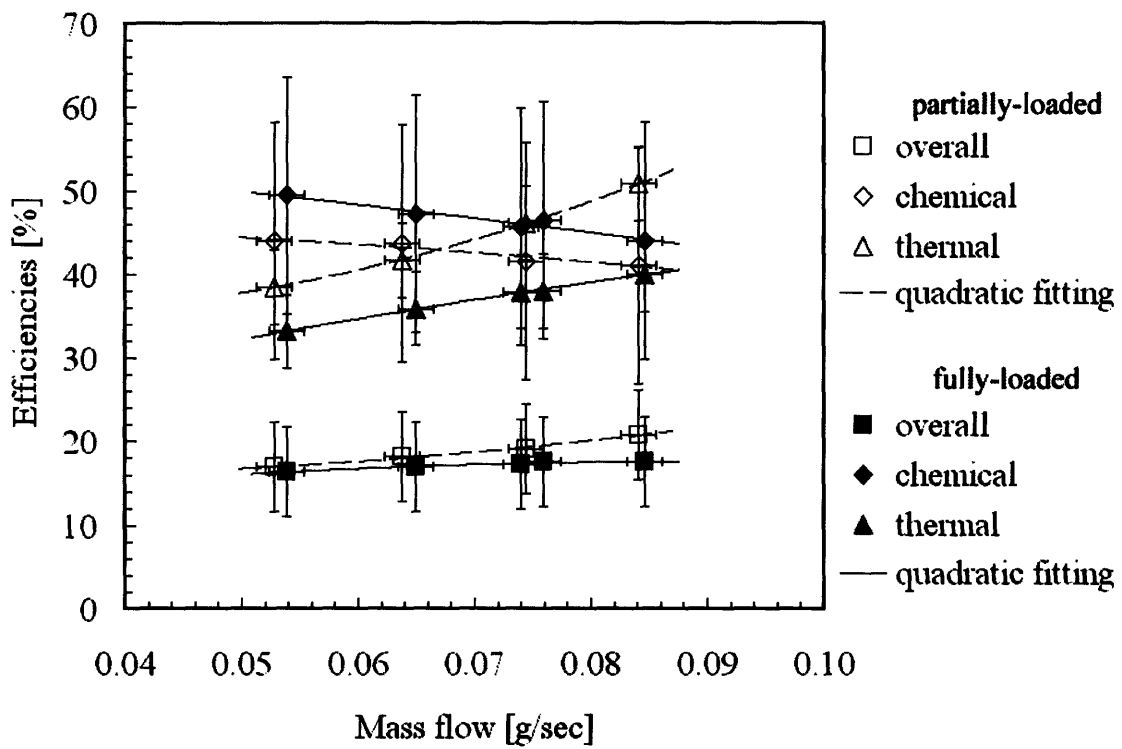


Figure 4-13: Efficiency breakdown comparison between the fully-loaded and the partially-loaded catalytic combustors ($\phi = 0.9$)

The two devices can also be analyzed on the non-dimensional operating map. On Figure 4-15 are listed two data points: one representing the fully-loaded catalytic combustor and the other representing the partially-loaded one. They are both for a mass flow rate of 0.08 g/sec and an equivalence ratio of 0.9. With these same operating conditions, the Peclet number (based on the actual catalyst volume, not the whole combustor volume) for the partially-loaded device is smaller due to a shorter residence time-scale. And because there is less catalyst, the chemical efficiency is also reduced. However, increased thermal efficiency wins over the reduction in the chemical efficiency, and the overall efficiency is higher.

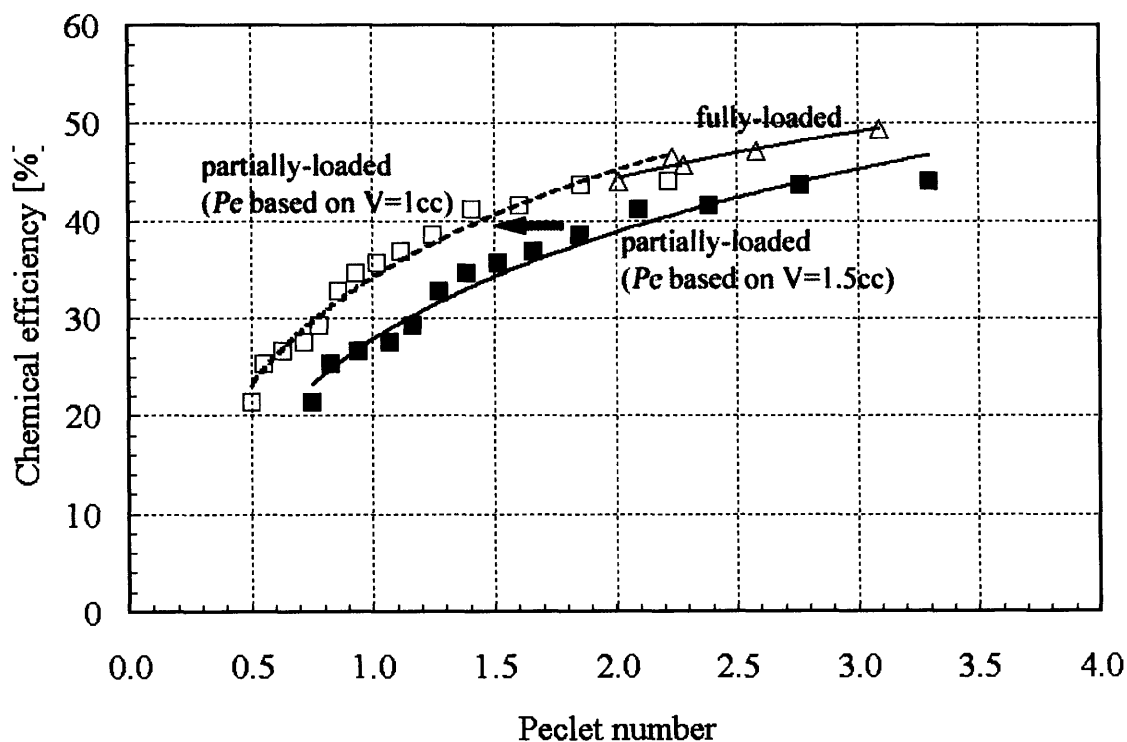


Figure 4-14: Comparison of chemical efficiencies vs. Peclet number between the fully-loaded and the partially-loaded (with corrected Peclet number) catalytic combustors

4.5 Catalytic combustor design case studies

Figure 4-16 shows all the experimental results obtained from the liquid-fueled catalytic combustor. Each experimental point was mapped out on a non-dimensional space;

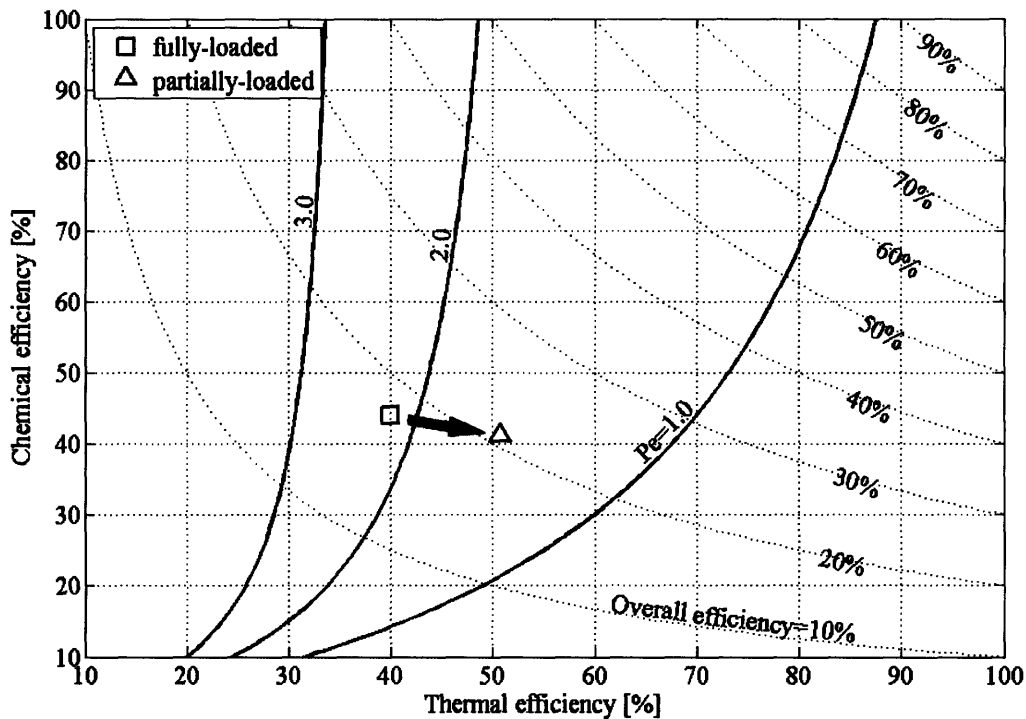


Figure 4-15: Device comparison on a non-dimensional operating space

the vertical axis represents the chemical efficiency, and the horizontal axis the thermal efficiency. The product of the two is the overall efficiency, which is represented by the curvilinear axis in the plot area. On top of the efficiencies, lines of constant Peclet numbers are included. These lines were generated by fitting the experiment-based Peclet numbers with the least square method. The average error of the least square fitting was 12.4%.

This non-dimensional map can serve as a preliminary design tool when designing a JP8-fueled catalytic micro-combustor as long as the thermal boundary conditions are similar to those of the current device. For example, once design specifications such as mass flow rate, equivalence ratio, and exit gas temperature are determined, the required overall efficiency can be computed based on those specifications per Equation (4.2). For a catalytic combustor, it is known that the structural temperature is similar or slightly below the exit gas temperature, so the structural temperature can be estimated with reasonable accuracy. Then, by taking a proper value for the surface area, the total heat loss can be estimated by using a method similar to the one

introduced in Appendix D. Then, the thermal efficiency as well as the chemical efficiency are calculated, and the operating point can be located on the non-dimensional operating map, allowing the designer to read the corresponding Peclet number on the map. This is the Peclet number required for the catalytic combustor to be operated at these conditions. Using this Peclet number, as well as the design specifications including the mass flow rate and the exit gas temperature, the combustor volume can be eventually decided based on Equation (4.11). A couple of design cases will be studied here.

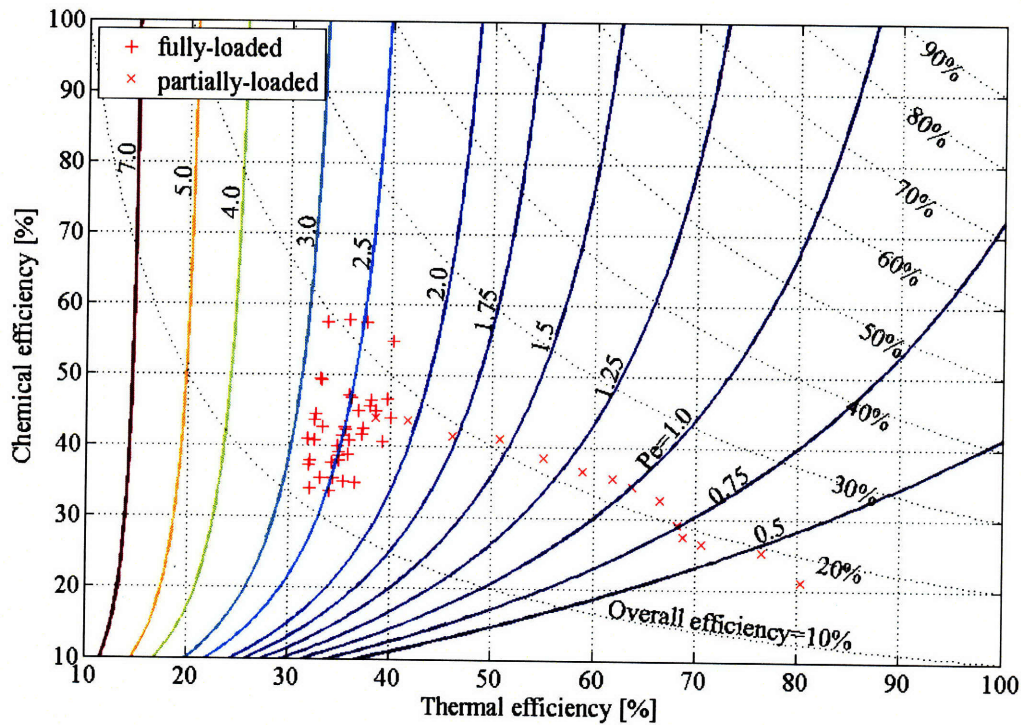


Figure 4-16: Non-dimensional operating map of liquid-fueled micro-combustor

4.5.1 Case #1: Liquid-fueled micro-combustor revisited

The current design of the liquid-fueled micro-combustor could not satisfy the operational requirements. In particular, the exit gas temperature was too low. The device can be characterized via the non-dimensional operating map (Figure 4-16), and a suggestion on future micro-combustor design can also be made.

The design mass flow rate of the liquid-fueled micro-combustor is 0.3 g/sec . From Figure 4-17, which plots the Peclet number versus the mass flow rate for all the data acquired in the device, it can be noted that the corresponding Peclet number would have been about 0.55 if the design flow rate were achieved in the fully-loaded configuration. At this Peclet number, the thermal efficiency is about 76% according to Figure 4-18. If this operation point is located on Figure 4-16, it gives an overall efficiency of approximately 20%, corresponding to an exit gas temperature of 900 K . This implies that the current liquid-fueled micro-combustor would not have achieved the required exit gas temperature of 1300 K at the design mass flow rate even if the structure did not fail.

If the goal is to achieve the required exit gas temperature without increasing the device volume, there may be two paths to be considered; one is to increase the chemical efficiency, and the other is to increase the thermal efficiency. Increasing the chemical efficiency without enlarging the combustor volume can be done by using a denser catalyst [2]. Larger surface area of a denser catalytic foam will enhance the diffusion rates and thus, increase the Peclet number for the given mass flow rate. This movement will increase the chemical efficiency, but because the denser catalyst will lead to more heat loss, the thermal efficiency will diminish. This was shown by the fully-loaded catalyst configuration test; it had more catalytic surfaces in the combustion chamber, but its overall efficiency was lower than that of the partially-loaded configuration at the same mass flow rate. Therefore, using a denser catalyst is not an effective way to improve combustor efficiency for the current liquid-fueled micro-combustor.

To see the effect of a better thermal isolation scheme, another non-dimensional operating map was generated for the silicon micro-combustor developed by Spadaccini [2, 26]. Figure 4-19 shows this map. Compared with the operating map of the liquid-fueled micro-combustor, for a given Peclet number and an overall efficiency, the thermal efficiency is higher, confirming that this device has a better thermal isolation of the combustion chamber. This is due to the existence of a recirculation jacket, which is a wrap-around flow path thermally-isolating the combustion chamber

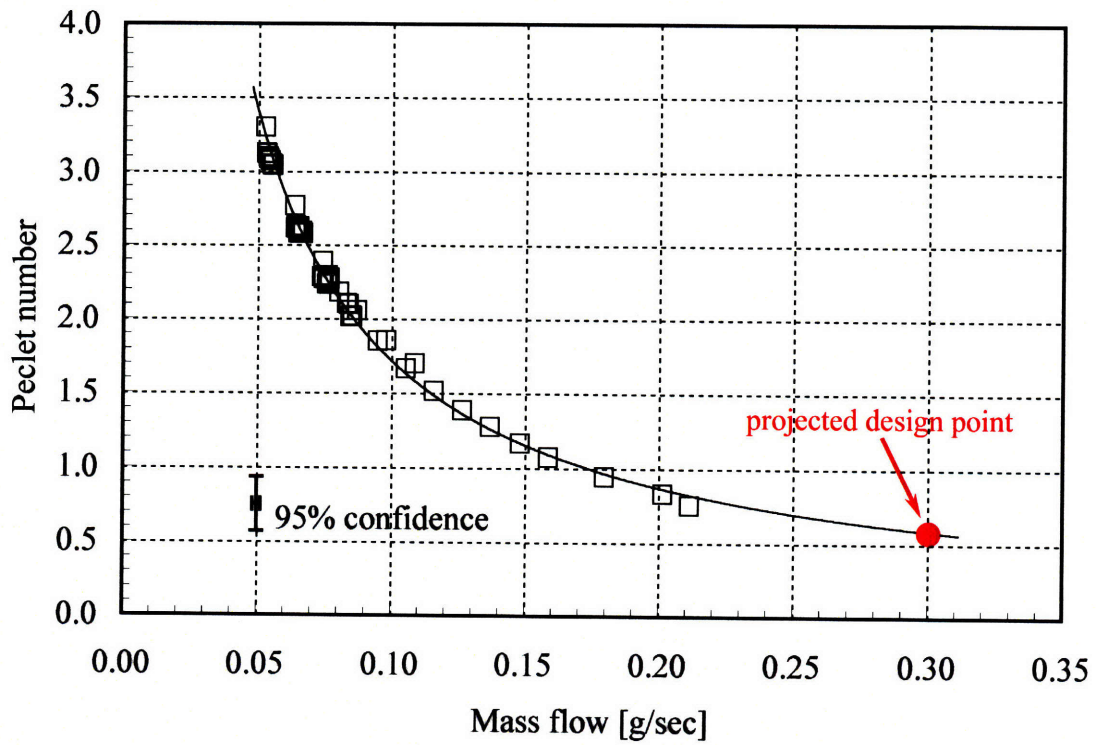


Figure 4-17: Peclet number vs. mass flow rate for all data acquired in the liquid-fueled micro-combustor

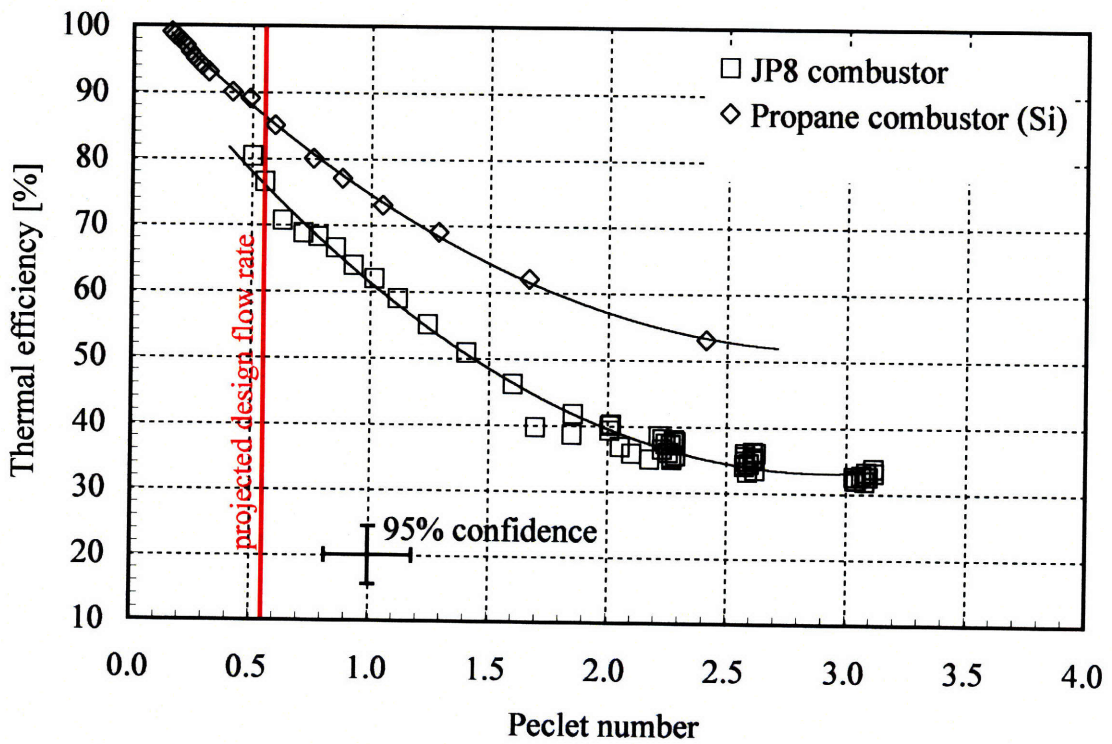


Figure 4-18: Thermal efficiencies vs. Peclet number for the liquid-fueled micro-combustor and the silicon micro-combustor based on catalytic propane combustion

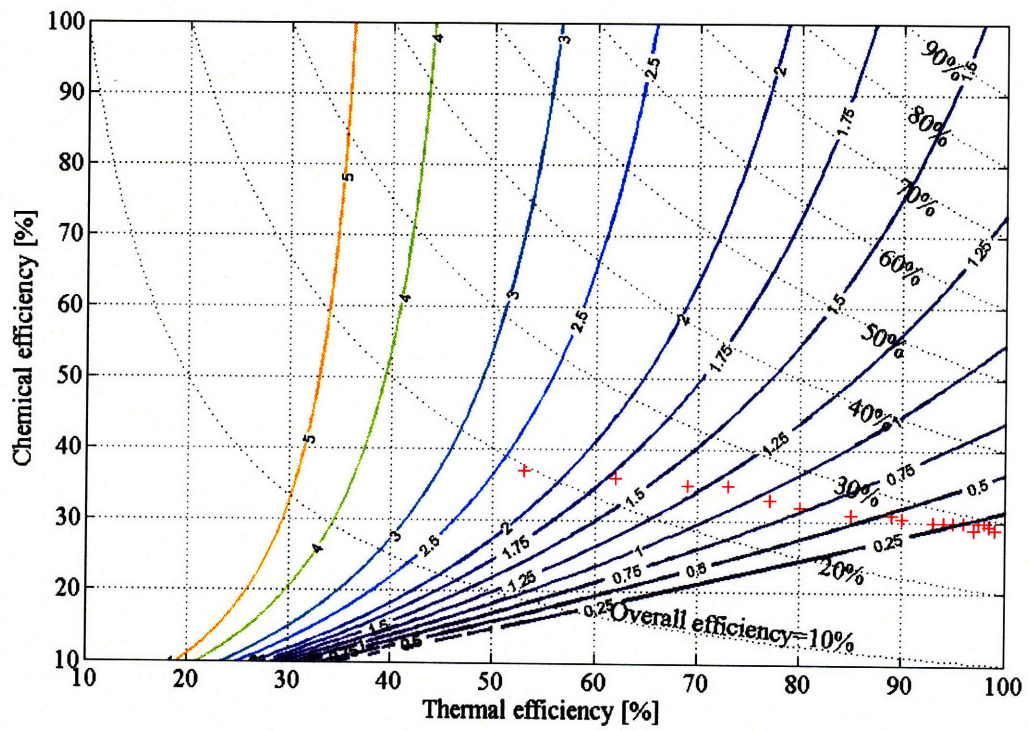


Figure 4-19: Non-dimensional operating map of silicon micro-combustor based on catalytic propane results (data obtained from Spadaccini [2])

(see Figure 1-4). As stated in Section 4.2.3, the non-dimensional map is determined by the thermal boundary conditions of the device. Thus, Figure 4-19, which was synthesized for the propane silicon micro-combustor, can be also used to estimate the performance of the liquid-fueled combustor if it had a recirculation jacket as the silicon device did. Referring to Figure 4-18 again, the thermal efficiency would become approximately 86%, for the design mass flow rate, if a similar recirculation jacket is built in the liquid-fueled micro-combustor. On Figure 4-19, the Peclet number of 0.55 and the thermal efficiency of 86% correspond to an overall combustor efficiency of about 28%, which translates to an exit gas temperature of 1100 *K*. This is still short of the design requirement, but shows about a 200 *K* increase in the exit gas temperature and an 8%-point gain in the overall combustor efficiency.

To further improve the efficiency of the combustor, the combustor volume may be increased by 50% to obtain a Peclet number of 0.75 at the design flow rate, and/or other schemes for better thermal isolation of the combustor may be adopted. One possible solution would be to minimize the contact area between the catalyst and the combustor structure by suspending the catalytic insert in the combustion chamber on seats. However, Spadaccini [2] found that the existence of a bypass flow around the catalytic insert discourages the fuel and air mixture from flowing through the catalyst, so the seats must not allow a bypass flow path; concentric circles will work the best. Large surface areas of the extended packaging block and the ceramic clamps are responsible for the large heat loss as well. Reducing the size of these structures will also be helpful. A surface treatment, such as low-emissivity coating, may be applied on the exterior of the device to reduce radiative heat loss.

4.5.2 Case #2: Combustor for TPV application

The liquid-fueled micro-combustor is a potential heat source for microscale thermophotovoltaic (TPV) systems. A fundamental difference between combustion systems for an engine and a TPV system is that the latter desires the structure to be hot, and the heat transfer through the combustor walls to be large. The catalytic combustor has shown these characteristics, so it becomes an attractive option for the

TPV application. Let us design a catalytic JP8 combustor for a TPV system with the following specifications:

$$T_{wall} = 1200 K, \quad \text{Heat source power} = 100 W$$

When the structural temperature is $1200 K$, the exit gas temperature may be estimated to be $1250 K$ from our previous experiences. Assuming a stoichiometric equivalence ratio, this exit gas temperature matches with an overall efficiency of 33%⁵. If the combustor's surface area is $10 cm^2$, the total heat transfer across the structure becomes about $100 W$, resulting in $10 W/cm^2$ of heat flux⁶. Supposing the mass flow rate to be $0.06 g/sec$, the chemical and thermal efficiencies are computed to be 90% and 35%⁷, respectively. Now, according to the non-dimensional operating map, the matching Peclet number is about 2.5. To achieve this Peclet number with the exit gas temperature of $1250 K$ and the mass flow rate of $0.06 g/sec$, the combustor volume must be approximately $920 mm^3$, according to the Equation (4.11). The design parameters are summarized in Table 4.1.

Parameter	Value
structural temperature (T_{wall})	1200 K
exit gas temperature (T_{exit})	1250 K
mass flow rate (\dot{m})	0.06 g/sec
equivalence ratio (ϕ)	1.0
heat source power	100 W
combustor volume	920 mm ³
combustor surface area	10 cm ²

Table 4.1: A workable set of design parameters for liquid-fueled catalytic combustor for a microscale TPV system

⁵This is a fluid power to fuel power efficiency as is usually defined for an engine combustor. For a TPV system, however, the efficiency is usually defined by a heat source power to fuel power ratio.

⁶This number is based on the heat transfer model described in Appendix D which assumes a natural convection boundary condition. In TPV systems, however, the device is often actively cooled on the opposite side of the photo-emitter, and it may induce more heat transfer.

⁷Again, this is a thermal efficiency based on the fluid power.

4.6 Performance of the fuel vaporizer

Fuel boiling in the vaporizer channels was observed through the window on the SD-2 glass layer during the experiments. In addition, thermal infrared images (Figure 4-2) show that the highest temperature occurs around the inlet region of the combustor, which implies that the mixture lights off shortly after it enters the combustion chamber. One can be certain that the fuel vaporizer and the mixing chamber work as intended. Although the fuel enters the vaporizer through a single hole, the fuel was distributed along the fuel plenum, and circumferential non-uniformity was not visible. At the fuel flow rates below 0.006 g/sec , which is approximately a third of the design point, the boiling front was formed in the middle of the fuel supply channel, not in the fuel vaporizer (Figure 4-20). However, this was as predicted by the fuel vaporizer model⁸. At the fuel flow rates around 0.006 g/sec , the fuel started to enter the vaporizer channels and was vaporized in them. The operability of the fuel vaporizer was demonstrated at fuel flow rates up to 0.01 g/sec , which is about a quarter of the design point because the total mass flow rate could not be increased further.

4.7 Assessment of device degradation

The catalytic combustion experiments were conducted for a total of over ten hours with several light-up and cool-down cycles. There was no observable degradation in terms of performance until the fully-loaded configuration cracked due to thermal stresses. The exit gas temperature response was repeatable for the same conditions, showing that catalysis was not lost. However, when the parts were taken apart and observed under a microscope, considerable discoloration was notable. Figure 4-21 shows the fuel injection holes before and after operation. This discoloration was attributed to deposition of decomposed carbon and oxidation of silicon. However, pressure change in the fuel supply tube due to a blockage of the fuel flow path was not observed.

⁸If 1 mm is used for the vaporizer's hydraulic diameter, 0.006 g/sec of fuel flow can be vaporized in 30 mm , which is about the length of the fuel supply channel.

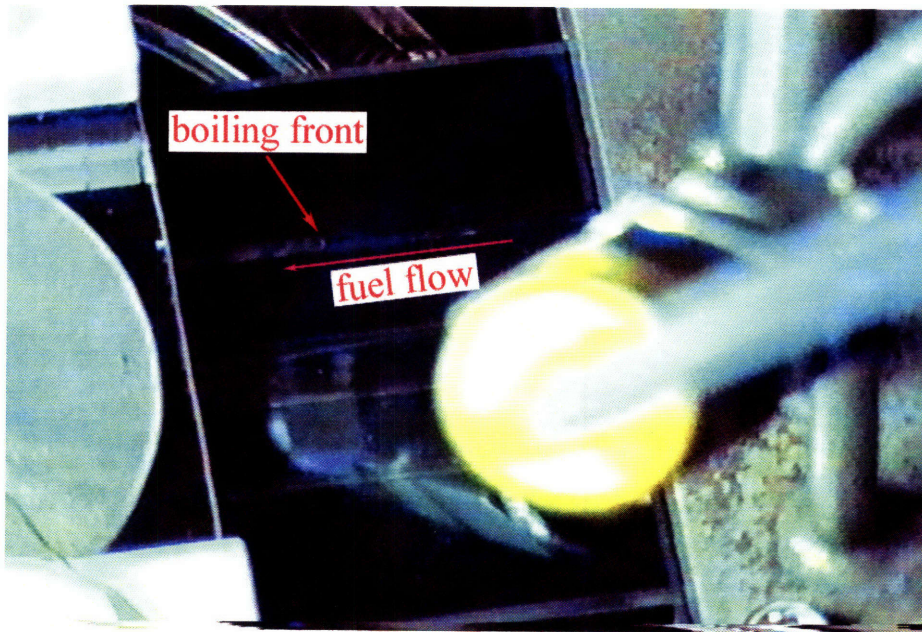
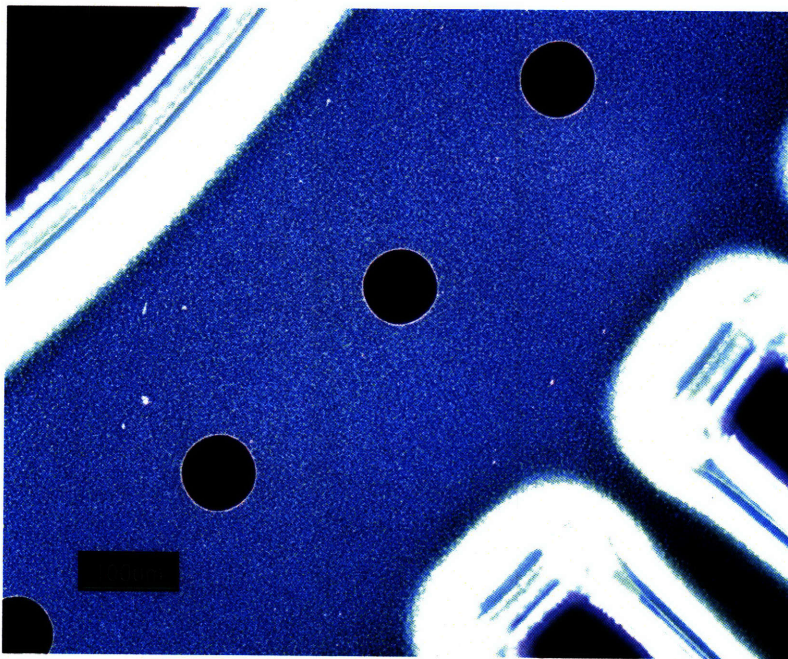


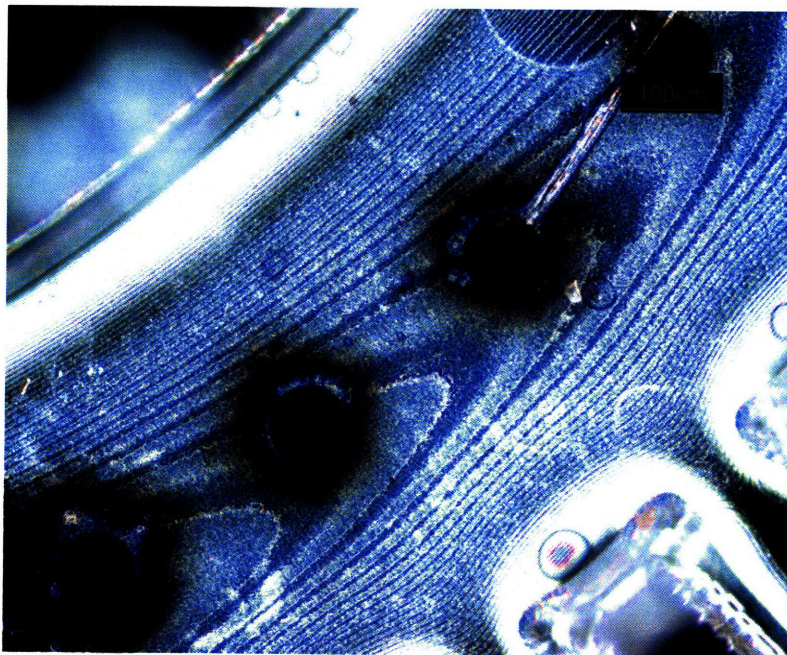
Figure 4-20: Boiling front formed in the middle of the fuel supply channel at low fuel flow rates

The catalytic insert showed even more discoloration (Figure 4-22). The insert was observed in an SEM, and the images are also included in Figure 4-22. Such damages as cracks, peel-offs, and agglomeration were visible. When using the SEM, the specimen did not allow increasing the magnification power beyond 2000 \times . This is because a good amount of carbon is burnt by the electron beam, disturbs the detector, and prevents the SEM from acquiring a clear image [64].

Even with some coking and oxidation, the performance degradation of the device was not notable during about ten hours of operation. So, the device life is expected to be at least several hours. However, the device was tested below the operational requirement of 1300 K exit gas temperature. If the device operates at a raised temperature, oxidation may become severe. How coking will be affected by the elevated temperatures remains uncertain.

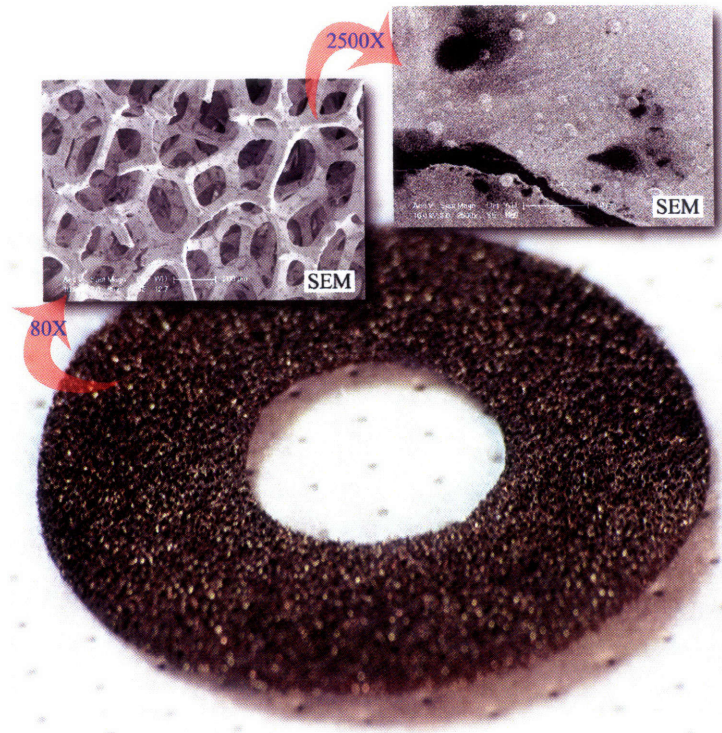


(a)

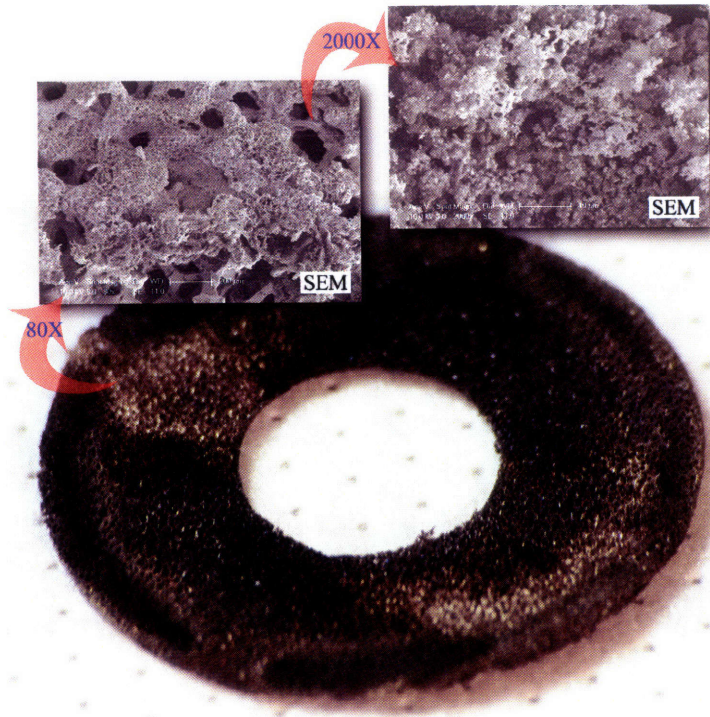


(b)

Figure 4-21: Fuel injection holes before testing (a) and after 10 hours of operation (b)



(a)



(b)

Figure 4-22: Catalytic insert before testing (a) and after 10 hours of operation (b)

4.8 Chapter summary

The liquid-fueled micro-combustor was experimentally characterized, and the results were presented in this chapter. With the combustion chamber fully loaded with a catalyst, JP8 combustion was stably sustained at mass flow rates up to 0.1 g/sec , at which point the structure failed due to thermal stresses. The highest exit gas temperature achieved was 780 K , and the overall combustor efficiency ranged from 10 to 20%.

The combustor was also tested with just two thirds of the volume filled with a catalyst. Catalytically-anchored gas-phase combustion was not initiated in this device configuration, but the performance was like a catalytic combustor with two thirds of the baseline volume. In this partially-loaded catalytic combustor, the mass flow rate could be extended to 0.2 g/sec without damaging the device. The corresponding exit gas temperature was 640 K , leading to the best power density realized in the device, 54 MW/m^3 . The overall efficiencies were as high as 19%. The partially-loaded configuration gave higher thermal efficiencies over the fully-loaded device even though the chemical efficiencies were lower, resulting in higher overall combustor efficiencies. However, the operational requirement ($T_{exit} = 1300\text{ K}$ at $\dot{m} = 0.3\text{ g/sec}$) could not be met in both configurations. Including a recirculation jacket around the combustion chamber like the silicon micro-combustor would be necessary, as well as other schemes for better thermal management, to reach the design requirement.

An analysis on the performance of the catalytic JP8 combustor was conducted using a non-dimensional operating map, which was constructed based on the empirical data. The map can explain the different characteristics of the fully-loaded and the partially-loaded catalytic combustors. The map was also used to provide a suggestion for future liquid-fueled micro-combustor. A design case study on TPV combustors was also included in the chapter.

The performance did not degrade for over ten hours of operation, but coking and oxidation were observed. The fuel vaporizer worked as intended as well.

Chapter 5

Summary and Conclusions

This chapter summarizes the research described in this thesis and presents conclusions and recommendations for future work.

5.1 Summary of research

As part of an effort to develop a microscale gas turbine engine using micro-fabrication techniques, this thesis has presented work regarding the combustion system utilizing JP8 as a fuel. Three aspects were covered in the thesis:

Design : The experimental apparatus was designed to explore the concept of the liquid-fueled micro-combustor. Several design models were developed and used. First, a catalytic combustion model was developed to estimate the catalytic combustion time-scale of JP8. Based on this model, the volume of the combustion chamber was determined to be 1.4 *cc*, corresponding to a mass flow rate of 0.3 *g/sec* and an exit gas temperature of 1300 *K*. A two-phase heat transfer model was developed to design the fuel vaporizer, and the vaporizer was designed accordingly: 49 channels, each having a hydraulic diameter of 500 μm and a length of 10 *mm* to have a vaporizing capacity of 0.04 *g/sec*. Detailed design methodologies and important dimensions were presented in Chapter 2.

Fabrication : The apparatus was fabricated utilizing ultrasonic machining and sili-

con micro-fabrication techniques. Ultrasonic machining was used in fabricating the sapphire parts and the SD-2 packaging glass. The three silicon layers were micro-machined in the Micro Technology Laboratory (MTL) at MIT. Direct silicon fusion bonding and anodic bonding were used to establish bonding between parts. Non-bondable parts were mechanically clamped with spring-loaded ceramic blocks. The catalytic insert was cut out of nickel foam and impregnated with platinum. Key fabrication steps were explained in Chapter 3.

Testing : The liquid-fueled micro-combustor was then experimentally characterized.

With the entire combustion chamber filled with a catalyst, JP8 combustion was sustained stably in the micro-combustor at mass flow rates up to 0.1 g/sec , at which point the structure failed due to thermal stresses. An exit gas temperature of 780 K and an overall combustor efficiency of 19% were achieved. The performance of the device was limited both by the chemical and the thermal efficiencies. There is a possibility, however, that the thermal efficiency may be improved by designing the flow path more carefully, whereas the low chemical efficiency is inherently due to the small volume.

The combustor was also tested with just two thirds of the volume filled with a catalyst, expecting that this configuration could provide extended mass flow rate capabilities like a catalytic combustor as well as high exit gas temperatures like a gas-phase combustor. However, gas-phase ignition was not realized, which is believed to be because the presence of the catalytic combustion inhibited the ignition of the gas-phase combustion. Instead, the performance resembled a catalytic combustor with two thirds of the original volume. Therefore, the performance was limited mainly by insufficient flow residence time at high mass flow rates. In this device configuration, a mass flow rate of 0.2 g/sec , and a corresponding exit gas temperature of 640 K were acquired, leading to the best power density realized in the device, 54 MW/m^3 .

A non-dimensional operating map was generated from the experiments. Using the non-dimensional operating map, it was found that the exit gas temperature

requirement would not have been achieved even though the mass flow rate could be pushed to the design point (0.3 g/sec). If the device had a recirculation jacket like the silicon micro-combustor, the overall efficiency and the exit gas temperature would have been improved to 28% and 1100 K respectively, which is still short of the design requirement (1300 K). To achieve the operational requirement of the microengine without increasing the combustor volume, therefore, other thermal management schemes must be included along with the adoption of the recirculation jacket. The non-dimensional operating map can also provide preliminary guidance for designing a catalytic combustor with similar thermal boundary conditions.

Durability of the device was also assessed. The performance of the catalyst did not degrade for over ten hours of operation although some local destruction of the structure was visible under a microscope. The fuel vaporizer was tested for over ten hours without failure, but it showed some coking and oxidation. The device life was proven to be at least five to ten hours.

5.2 Review of contributions

The contributions of this research project can be summarized as:

- ***Demonstration of JP8 combustion in an environment replicating the MIT microengine***

Catalytic JP8 combustion was achieved at a mass flow rate of 0.2 g/sec within a combustor volume of 1.4 cc . This results in a combustor power density of 54 MW/m^3 and an overall efficiency over 20%. The device did not meet the operational requirement with the designed combustor volume because of poor thermal efficiencies. The thermal efficiency may be enhanced by including a thermally-isolating flow path around the combustion chamber.

- ***Development of a design methodology for catalytic combustion time-scales***

To estimate the required volume of the combustion chamber, a simplified model was developed. The model can predict the time-scale of catalytic combustion, whose reaction mechanism is not known. The model can be more generally used to approximate the time-scales of diffusion-limited catalytic combustion.

- ***Development of a heat transfer model for a fuel vaporizer***

A two-region, dual-phase heat transfer model was constructed and used in designing an on-board fuel vaporizer.

- ***Design, fabrication, and integration of an on-board MEMS fuel vaporizer***

An on-board fuel vaporizer was designed using the above heat transfer model, and fabricated with silicon micro-fabrication techniques. Its operability was demonstrated at fuel flow rates up to 0.01 g/sec, which is about a quarter of the design point because the total mass flow rate could not be increased further.

- ***Construction of an empirical non-dimensional operating map***

A non-dimensional operating map was generated based on all the experimental data acquired in the liquid-fueled micro-combustor. Via the non-dimensional operating map, it was shown that the design requirement could be achieved by improving the thermal isolation of the combustion chamber without increasing the combustor volume. The operating map is useful in both explaining the characteristics of liquid-fueled catalytic micro-combustors and designing a catalytic combustor with similar thermal boundary conditions.

- ***Investigation of device deterioration***

After ten hours of operation including several heat-up and cool-down cycles, minimal degradation of the device was observed. Although some localized destruction of catalyst was detected, the exit gas temperature response was repeatable for the same conditions, showing that the catalyst did not lose its catalysis. Deposition of decomposed carbon was observed on the walls of the device, especially along the fuel flow path. However, pressure change in the fuel

supply tube due to a blockage in the fuel flow path was not observed.

5.3 Recommendations for future work

Based on the conclusions of this thesis, the following is additional work recommended:

- *Development of a scheme for better thermal isolation*

It has been shown that the current design of the liquid-fueled catalytic micro-combustor cannot satisfy the exit gas temperature requirement because of low thermal efficiencies. If the device had a recirculation jacket like the silicon micro-combustor, the performance would have been improved, but it would still have not achieved the design requirement. A possible solution would be suspending the catalytic insert in the combustion chamber using some structures such as seats. But there must be no bypass flow path around the catalyst, so seats with the geometry of concentric circles may work the best. The exterior of the device may be coated with a low-emissivity material to reduce radiative heat loss.

- *Use of a more thermally durable material*

The fully-loaded catalytic device failed at one-third of the design mass flow rate. Thermal stresses induced by temperature gradients in the sapphire structure is believed to be the reason for the failure. A material that can better distribute the thermal load may be pursued. Silicon has a thermal conductivity that is a few times larger than that of sapphire, so it would significantly reduce the thermal stresses. However, use of a better thermal conductor can compromise the thermal efficiency of the combustor further. Hence, a scheme for better thermal isolation must be implemented as well.

- *Integration with the microengine*

The models developed and experimental results obtained in this work indicate that a catalytic JP8 micro-combustor is compatible for integration into the MIT microscale gas turbine engine for demonstrating self-sustaining operation. A combustor volume of 1.4 cc should be adequate to achieve an exit gas tem-

perature of 1300 K at a mass flow rate of 0.3 g/sec as long as better thermal management schemes are adopted relative to the micro-combustor presented in this work. This combustor volume is equivalent to the 1.4 cc volume of the self-sustained microengine (SSE) [65]. Thus, adding a fuel vaporizer layer to the SSE design as well as including catalyst in the combustion chamber could be a good starting point for integrating a liquid-fueled combustor with the microengine with minimal design changes. The fuel vaporizer can be built in the engine without a major modification.

- ***High-efficiency liquid-fueled micro-combustor***

The current work focused on maximizing power density by trying to achieve the required enthalpy rise of the flow within a combustor volume as small as possible. Catalytic combustion was a good option for this objective because it allowed stable combustion even with small combustor volume and low efficiencies. Had it not been for the catalytic combustion, it would not have been possible to sustain JP8 combustion at the mass flow rate of interest in this device size. Although it was shown that the operational requirements could be met without increasing the combustor volume, this approach led to poor combustor efficiencies. Ultimately, a high-efficiency liquid-fueled micro-combustor must be pursued. Since the required exit gas temperature is rather low compared to the adiabatic flame temperature of stoichiometric JP8 combustion, the high-efficiency combustor should be operated at low overall equivalence ratio. To efficiently burn JP8 fuel at low equivalence ratio, the combustor must be either a dual-zone gas-phase combustor or a multistage catalytic-homogeneous hybrid combustor. Either of them is likely to require much larger combustor volume. In particular, hybrid combustors are typically larger and heavier than gas-phase combustors [43], so their use is almost exclusively limited to reduce toxic emissions for ground-based power-generating engines. Comparing figure of merits of those two combustors and optimizing between high power density and efficiency are no trivial task, and thus open to further research.

Appendix A

Drawings of Photomasks

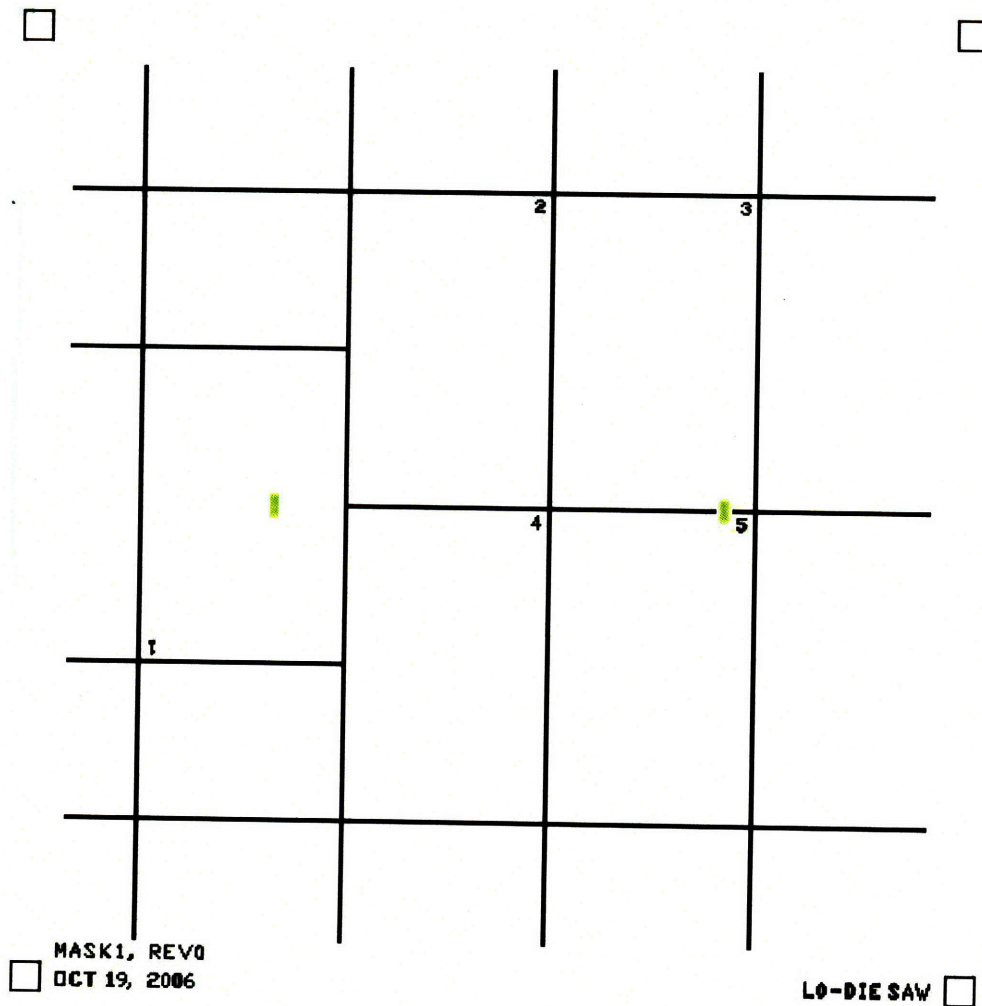
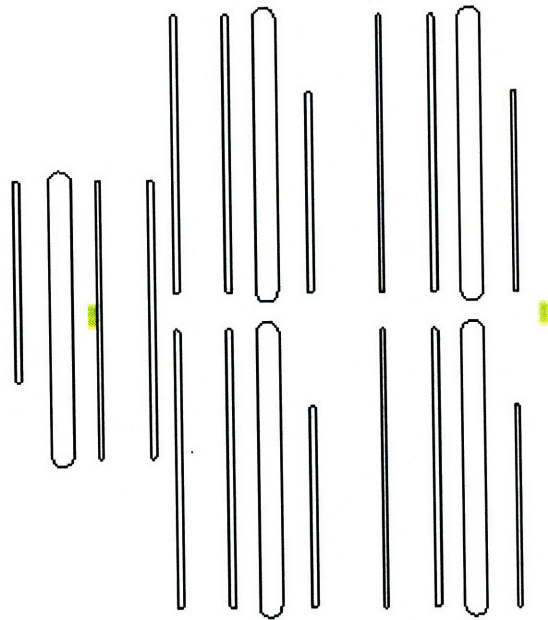
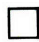


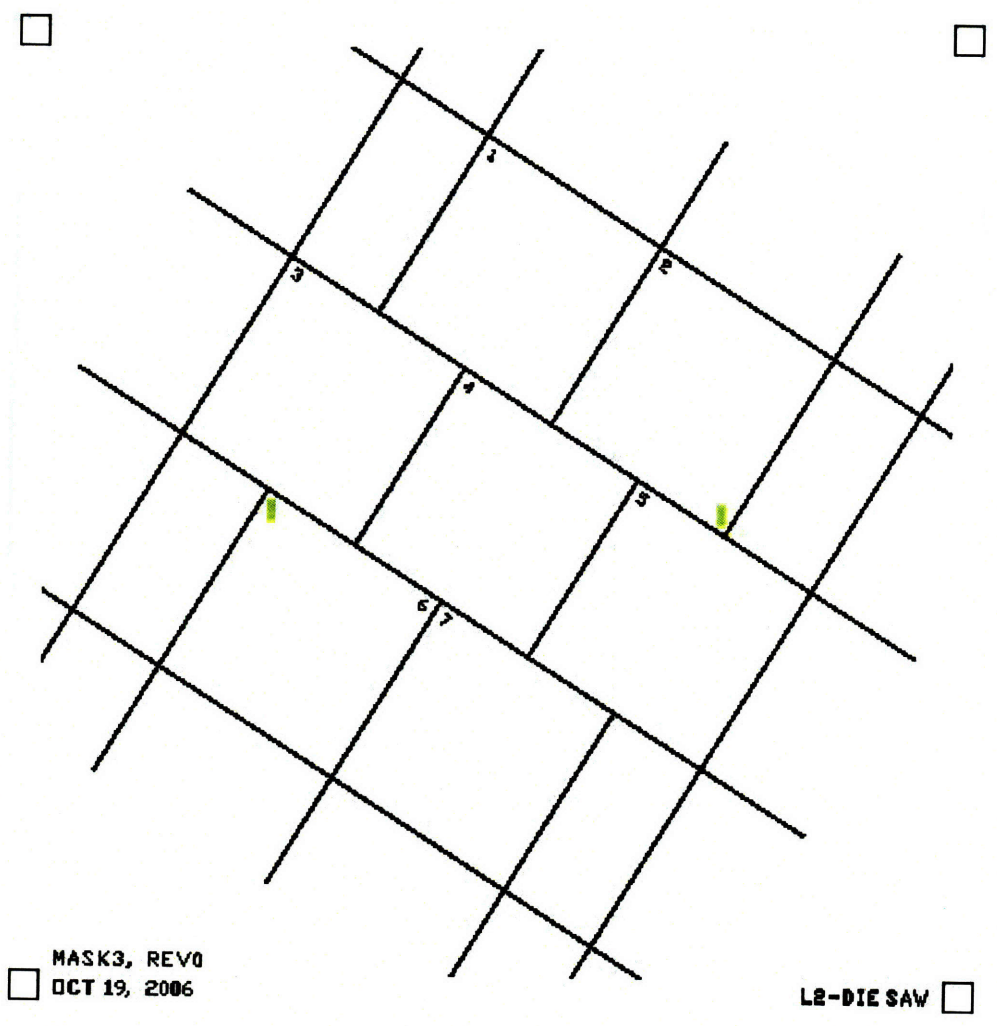
Figure A-1: Mask #1



 MASK2, REV0
OCT 19, 2006

LO-FR 

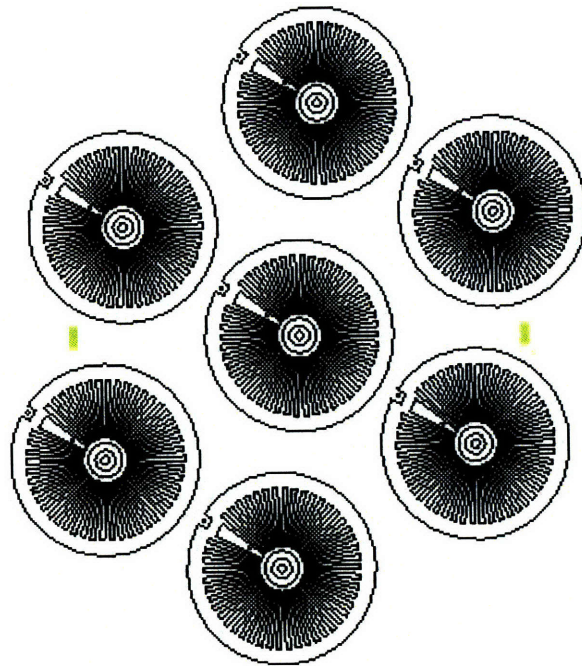
Figure A-2: Mask #2




□ MASK3, REV0
□ OCT 19, 2006

LB-DIE SAW □

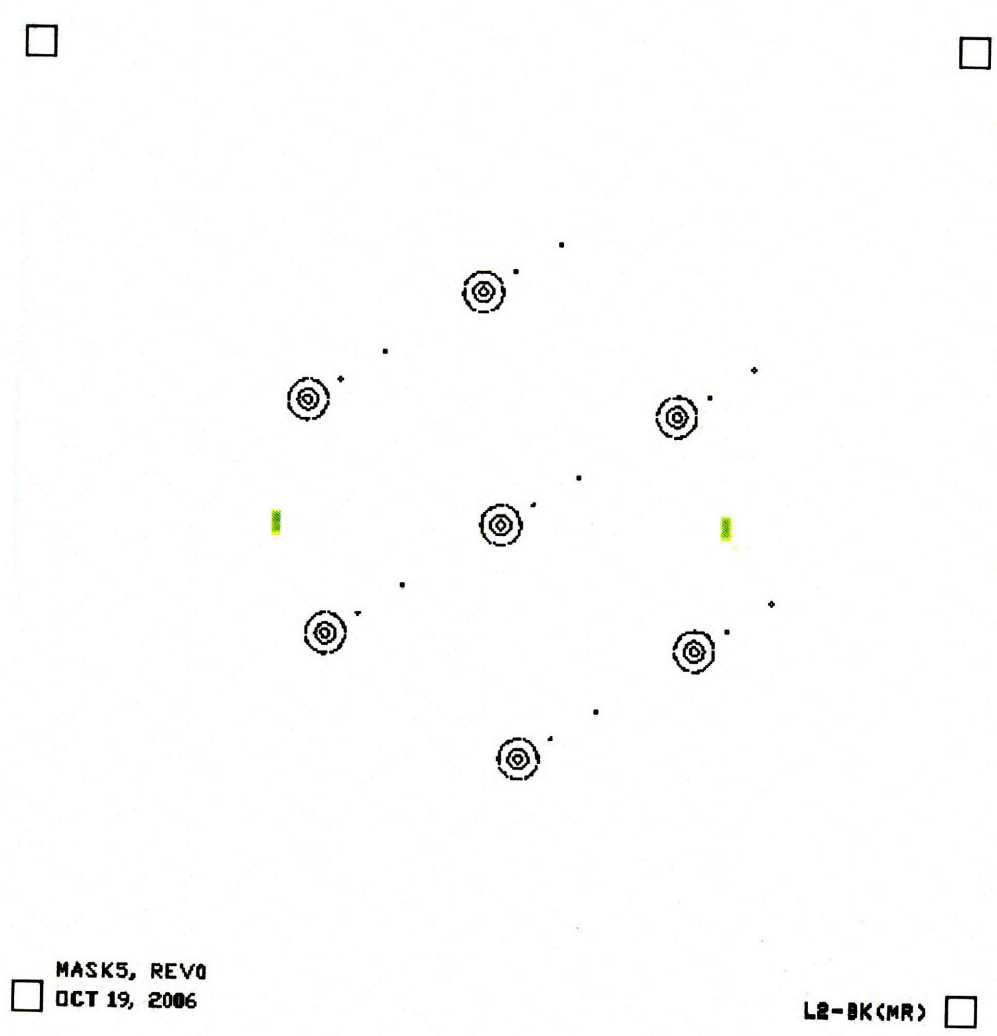
Figure A-3: Mask #3



 MASK4, REV0
OCT 19, 2006

L2-FR 

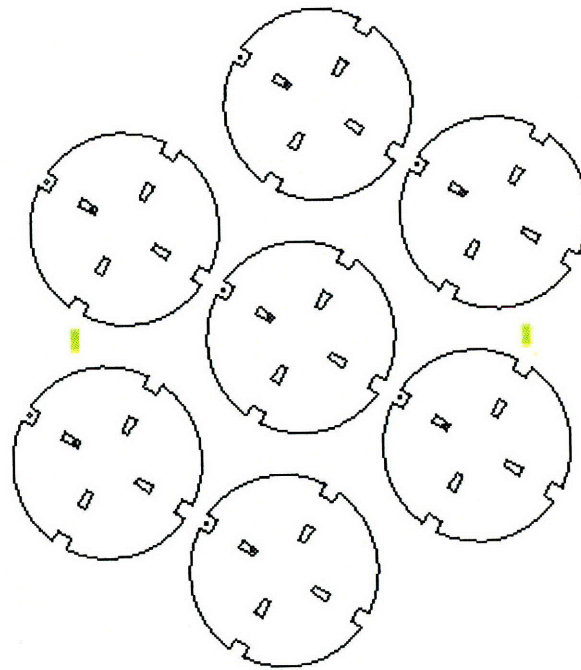
Figure A-4: Mask #4

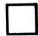


MASK5, REV0
 OCT 19, 2006

L2-BK(MR)

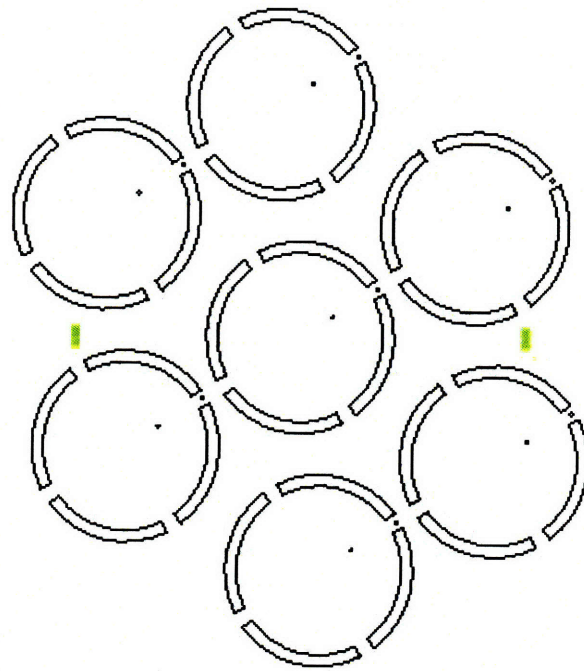
Figure A-5: Mask #5

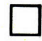


 MASK6, REV0
OCT 19, 2006

L3-FR 

Figure A-6: Mask #6



 MASK7, REV0
OCT 19, 2006

L3-BK(MR) 

Figure A-7: Mask #7

Appendix B

Mechanical Drawings of Ultrasonically Machined Parts

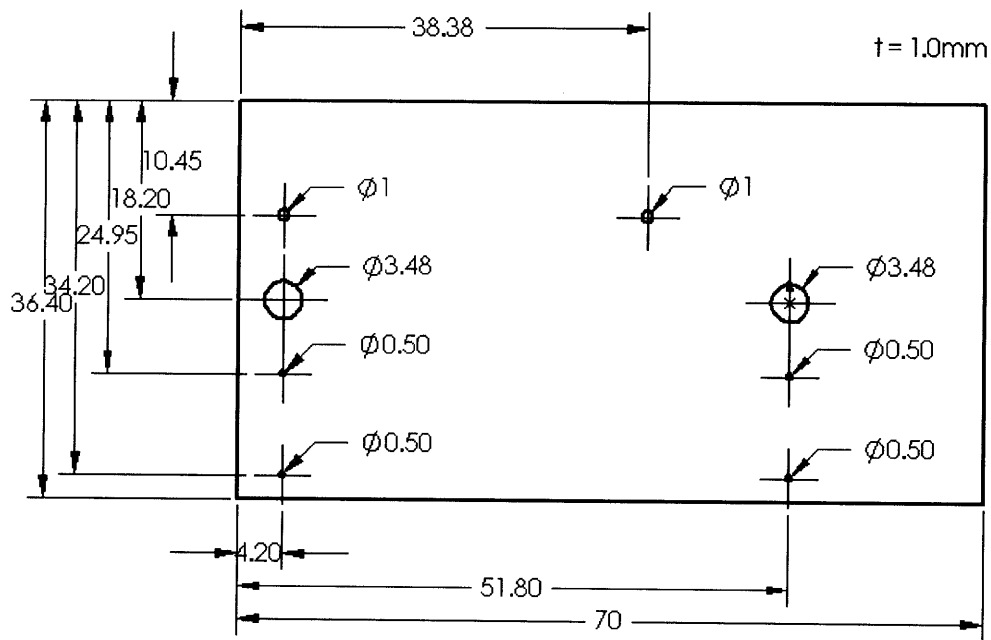


Figure B-1: Layer 2 (SD-2 glass)

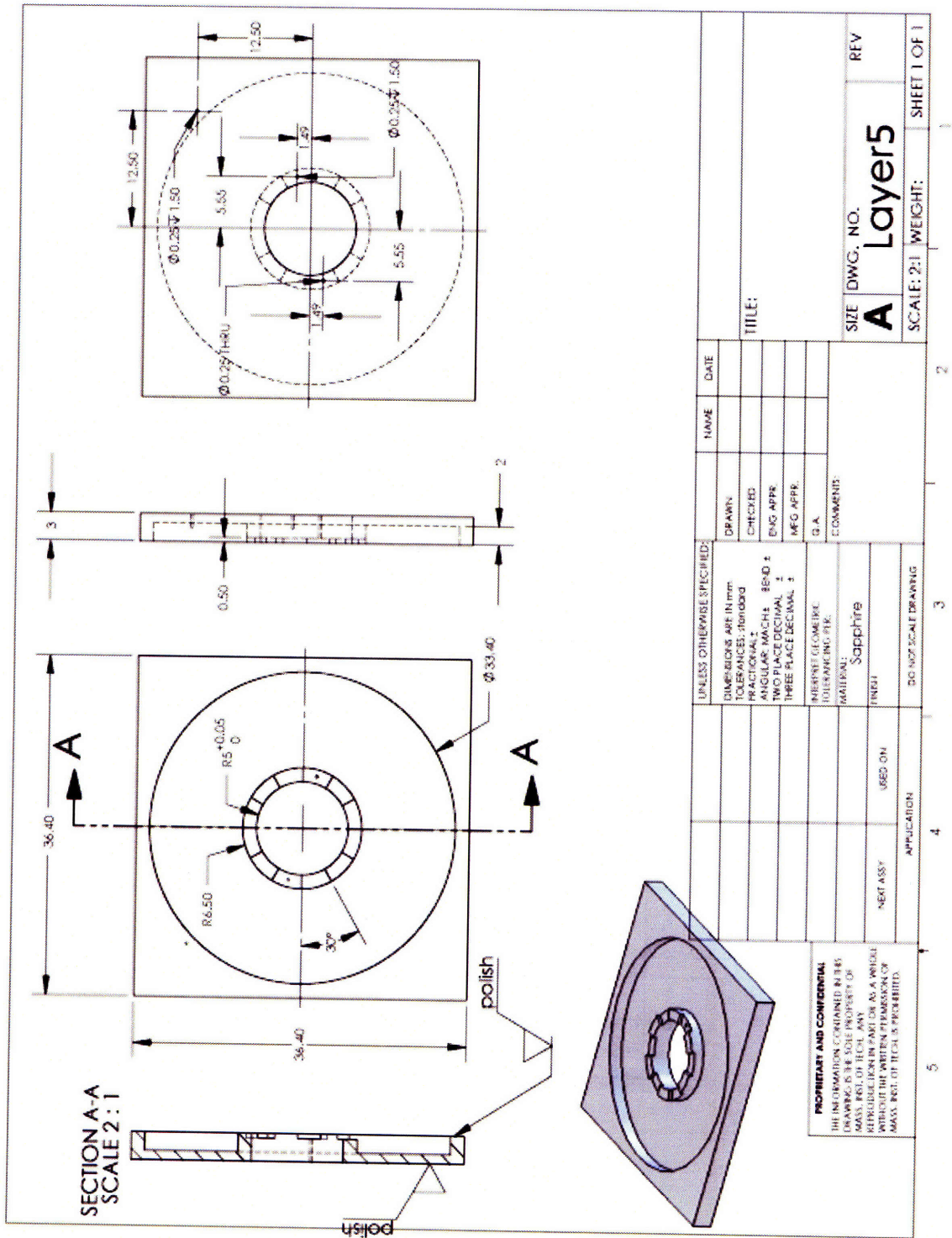


Figure B-2: Layer 5 featuring the combustion chamber (sapphire)

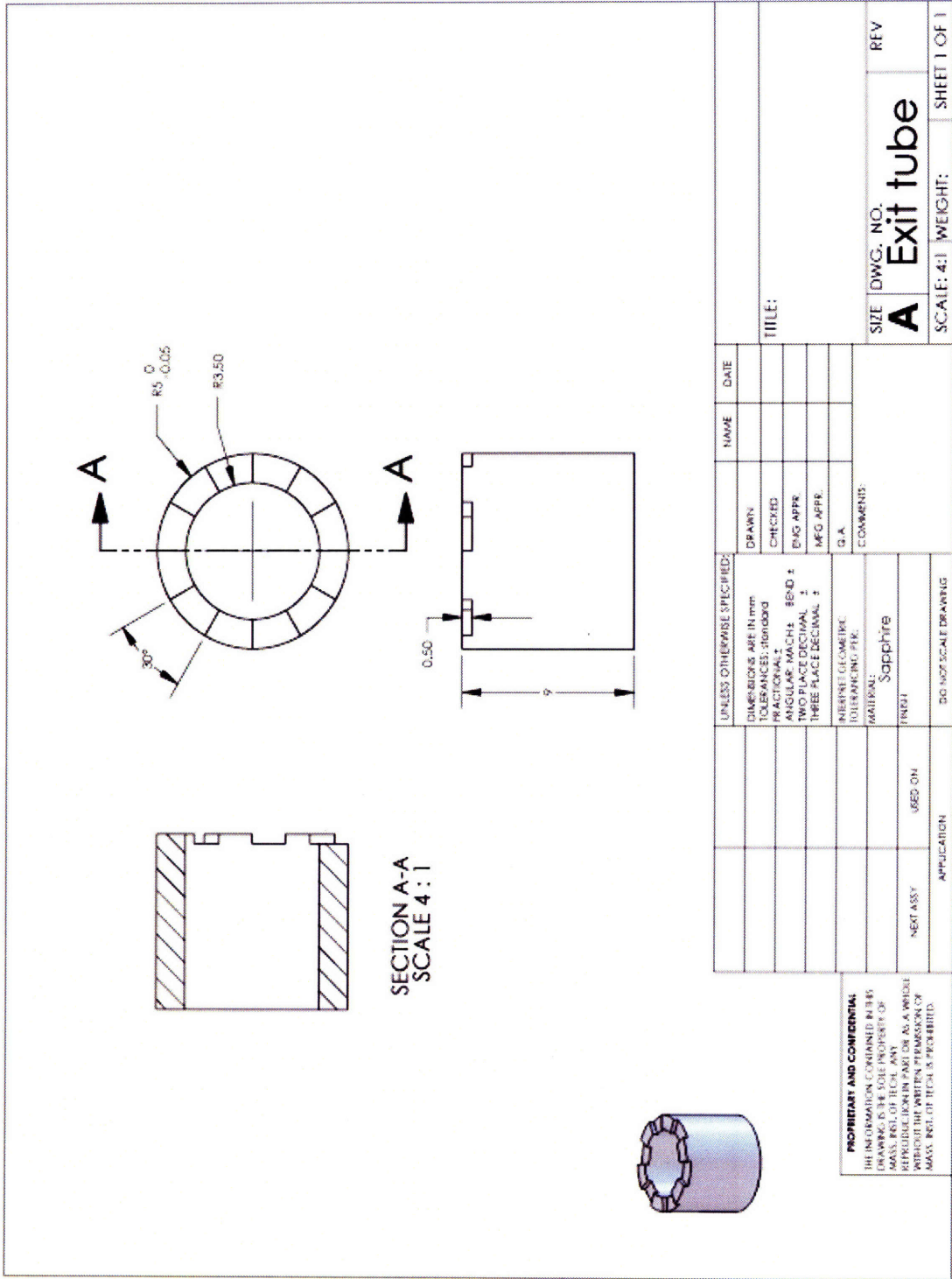


Figure B-3: Exit tube (sapphire)

Appendix C

Monte-Carlo Simulation on the Fuel Vaporizer Design Model

The fuel vaporizer design model introduced in Chapter 2 uses the fluid properties of JP8, properties of silicon, inlet temperature of the fuel, and wall temperature of silicon. There are uncertainties associated with these values. To see how these uncertainties in the parameters affect the model results, a Monte-Carlo simulation was conducted. Each input parameter was expressed as an independent, normally-distributed random variable. All the fuel properties and the thermal conductivity of silicon were modeled to have a standard deviation that matches 10% of the mean value. The model cannot calculate the result when the boiling point is lower than the wall temperature, so those parameters were adjusted so that the upper limit of the boiling point is 594 K , and the lower limit of the structural temperature is 596 K . The inlet temperature of the fuel must have relatively small uncertainty, so its standard variation was set to 1% of the mean. All the random variables, their baseline value, standard deviation, upper and lower limits are summarized in Table C.1.

A Monte-Carlo simulation was conducted on the vaporizer design model using 10,000 randomly generated parameter sets, and the result is shown in Table C.2. The result shows that the model required the channel length to be less than 2.66 mm for 90% of all the simulation cases. In fact, it predicted 5 mm or shorter over 99% of the time. Whereas the required length was about 5 mm based on the mean value, the

mean of all simulation cases was shifted to 1.8 mm . Uncertainties in each parameter had a combined effect of reducing the required length of the vaporizer channel. Therefore, designing based on the baseline values would be a conservative and safe approach. The Monte-Carlo simulation result also indicates that the boiling point of the fuel is the parameter that affects the result most strongly. Following next are the structural temperature, the thermal conductivity of JP8, and the specific heat of JP8 in order. Other parameters have relatively little influence on the model results.

Parameter	Mean (baseline)	Std. deviation	Lower limit	Upper limit
ρ_l [kg/m^3]	635	63.5	381	889
ρ_v [kg/m^3]	2.96	0.296	1.78	4.14
μ_l [Ns/m^2]	0.000253	0.0000253	0.000152	0.000354
σ [N/m]	0.017	0.0017	0.0102	0.0238
C_p [J/kgK]	2640	264	1584	3696
k_l [W/mK]	0.1034	0.01034	0.0620	0.1448
h_{fg} [kJ/kg]	270	27	162	378
$T_{B.P.}$ [K]	590	59	354	594
k_{wall} [W/mK]	80	8	48	112
T_{inlet} [K]	300	3	288	312
T_{wall} [K]	600	60	596	840

Table C.1: Input parameters for the Monte-Carlo simulation

Required channel length [mm]	Percentile
2.66	10%
2.30	20%
2.05	30%
1.86	40%
1.69	50%
1.53	60%
1.37	70%
1.19	80%
0.97	90%
0.12	100%

Table C.2: Monte-Carlo simulation result: percentile

Appendix D

Heat Loss Model

Overall combustor efficiency is computed directly from the thermocouple measurements at the combustor inlet and exit. To understand the performance of the combustor better, the overall efficiency is decomposed into thermal and chemical efficiencies:

$$\eta_{overall} = \eta_{chemical} \times \eta_{thermal} \quad (D.1)$$

where,

$$\eta_{overall} = \frac{(\dot{m}_a + \dot{m}_f)h_{exit} - \dot{m}_a h_{inlet}}{\dot{m}_f h_f} \quad (D.2)$$

$$\eta_{chemical} = \frac{[(\dot{m}_a + \dot{m}_f)h_{exit} - \dot{m}_a h_{inlet}] + q_{loss}}{\dot{m}_f h_f} \quad (D.3)$$

$$\eta_{thermal} = \frac{(\dot{m}_a + \dot{m}_f)h_{exit} - \dot{m}_a h_{inlet}}{[(\dot{m}_a + \dot{m}_f)h_{exit} - \dot{m}_a h_{inlet}] + q_{loss}} \quad (D.4)$$

Hence, it becomes necessary to quantify the total heat loss out of the device. The total heat loss can be estimated by summing up convective and radiative heat losses. Conductive heat loss turns out to be less than 1 W for most cases, which is only a few of percent of the convective or radiative heat losses. Thus, conductive heat loss is neglected. Heat flow from the test rig to the ceramic clamp blocks is insulated with graphite, so the temperature of the clamps is below 400 K. Conductive heat loss to the clamps are therefore neglected as well. The control volume was taken as Figure

D-1, and each heat transfer mode was investigated.

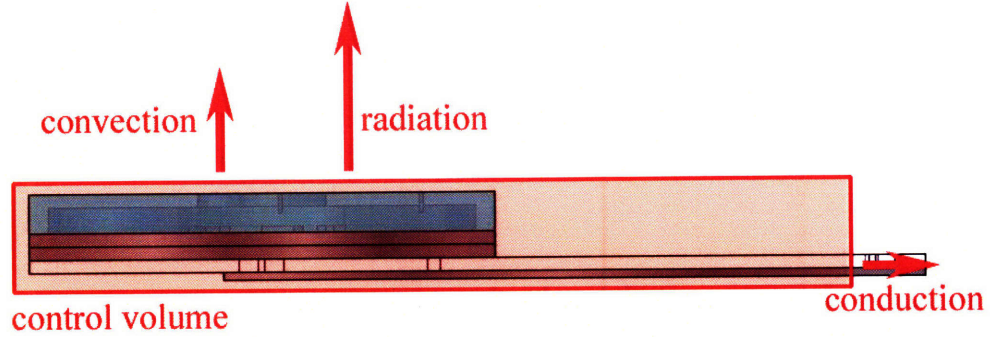


Figure D-1: Control volume for heat loss calculations

D.1 Convective heat loss

Convective heat loss can be calculated based on natural convection:

$$q_{conv} = (h_u A_u + h_l A_l)(T_{wall} - T_\infty) \quad (D.5)$$

where the subscripts u and l indicate the upper surface and the lower surface, respectively. The heat transfer coefficients can be evaluated with Equations D.7 through D.10 [46].

$$h_u = \frac{Nu_u L}{k} \quad (D.6)$$

$$h_l = \frac{Nu_l L}{k} \quad (D.7)$$

$$Nu_u = 0.54 Ra_L^{0.25} \quad (D.8)$$

$$Nu_l = 0.27 Ra_L^{0.25} \quad (D.9)$$

$$Ra_L = \frac{g \beta L^3}{\nu \alpha} (T_{wall} - T_{ambient}) \quad (D.10)$$

D.2 Radiative heat loss

Radiative heat loss is estimated as:

$$q_{rad} = \varepsilon\sigma(A_u + A_l)(T_{wall}^4 - T_{\infty}^4) \quad (D.11)$$

The emissivity of the structure was assumed to be 0.8.

D.3 Conductive heat loss

Heat conduction is calculated by:

$$q_{cond} = \frac{\Delta T}{R_{thermal}}; \quad R_{thermal} = \frac{L}{kA} \quad (D.12)$$

Since $L \sim 5 \text{ mm}$, $k \sim 10 \text{ W/mK}$ (for SD-2 glass), $A \sim 50 \text{ mm}^2$, and $\Delta T \sim 10 \text{ K}$, the conductive heat loss is on the order of 1 W .

Finally,

$$q_{loss} = q_{conv} + q_{rad} \quad (D.13)$$

Appendix E

Uncertainty Analysis on Experimental Measurements

E.1 Uncertainties in the independent measurements

Table E.1 lists the 95%-confidence uncertainties of the independently measured quantities such as the flow rates, pressures, and temperatures. These numbers were quoted by their manufacturers. An exception is the gas temperature. Tzeng [31] found that exposure to flame causes type-K thermocouples a drift by roughly 20 *K*. Thus, the 95%-confidence interval was set to ± 32 *K* for the gas temperature measurement although the same type of thermocouple was used as the wall temperatures.

Measurements	95%-confidence uncertainty
air flow rate	± 0.0015 <i>g/sec</i>
JP8 flow rate	± 0.0004 <i>g/sec</i>
pressures	± 0.5 <i>psi</i>
wall temperature	± 12 <i>K</i>
gas temperature	± 32 <i>K</i>

Table E.1: Uncertainties of the independently measured quantities

E.2 Uncertainties in the derived quantities

E.2.1 Equivalence ratio

The equivalence ratio was computed as:

$$\phi = \frac{\dot{m}_f/\dot{m}_a}{(\dot{m}_f/\dot{m}_a)_{stoichiometric}} \quad (\text{E.1})$$

Unlike hydrogen or propane, JP8 fuel is a mixture of various species. Since the exact composition is unknown, there is a precision uncertainty in the stoichiometric fuel-to-air ratio:

$$p_\phi = \frac{\partial \phi}{\partial ((\dot{m}_f/\dot{m}_a)_{stoichiometric})} P_{(\dot{m}_f/\dot{m}_a)_{stoichiometric}} \quad (\text{E.2})$$

JP8 was modeled as $C_nH_{1.8n}$ ($n = 13$), and the stoichiometric fuel-to-air ratio was taken to be 0.0693. But for liquid hydrocarbon fuels, it is known that hydrogen-to-carbon ratio may vary from 1.6 to 2.0. Therefore, the stoichiometric fuel-to-air ratio can range from 0.0680 to 0.0707, or ± 0.0014 . The precision uncertainty in the equivalence ratio, p_ϕ , becomes ± 0.0195 .

There is also a bias uncertainty caused by the flow rate measurements:

$$\begin{aligned} b_\phi &= \frac{\partial \phi}{\partial \dot{m}_f} b_{\dot{m}_f} + \frac{\partial \phi}{\partial \dot{m}_a} b_{\dot{m}_a} \\ &= \frac{1}{(\dot{m}_f/\dot{m}_a)_{stoichiometric}} \left[\frac{1}{\dot{m}_a} b_{\dot{m}_f} - \frac{\dot{m}_f}{\dot{m}_a^2} b_{\dot{m}_a} \right] \\ &= \phi \left[\frac{b_{\dot{m}_f}}{\dot{m}_f} - \frac{b_{\dot{m}_a}}{\dot{m}_a} \right] \end{aligned} \quad (\text{E.3})$$

Here, $b_{\dot{m}_a}$ and $b_{\dot{m}_f}$ are 0.0015 g/sec and 0.0004 g/sec, respectively (Table E.1). Among the data presented in this thesis, the maximum bias uncertainty occurred at an equivalence ratio of 1.3 and a mass flow rate of 0.05 g/sec. The corresponding uncertainty was ± 0.1540 .

The overall uncertainty can be calculated as the following [66]:

$$u_\phi = \sqrt{p_\phi^2 + b_\phi^2} \quad (\text{E.4})$$

Finally, 95%-confident uncertainty is ± 0.1552 , and this value was included in Figure 4-3. The large uncertainty in the equivalence ratio is mainly because the fuel flow controller was operated only up to 20% of its full capacity.

E.2.2 Overall combustor efficiency

The overall combustor efficiency is calculated by:

$$\begin{aligned} \eta_{overall} &= \frac{(\dot{m}_a + \dot{m}_f)h_{exit} - \dot{m}_a h_{inlet}}{\dot{m}_f h_f} \\ &= \frac{(\dot{m}_a + \dot{m}_f)C_{p,exit}T_{exit} - \dot{m}_a C_{p,inlet}T_{inlet}}{\dot{m}_f h_f} \end{aligned} \quad (\text{E.5})$$

A precision uncertainty is introduced because of the uncertainties in the fluid property values such as C_p and h_f :

$$p_{\eta_{overall}} = \sqrt{\left(\frac{\partial \eta_{overall}}{\partial C_{p,exit}} p_{C_{p,exit}}\right)^2 + \left(\frac{\partial \eta_{overall}}{\partial C_{p,inlet}} p_{C_{p,inlet}}\right)^2 + \left(\frac{\partial \eta_{overall}}{\partial h_f} p_{h_f}\right)^2} \quad (\text{E.6})$$

Due to a small fraction of the fuel (less than 7% by weight at stoichiometry), the enthalpy was estimated assuming the fluid was just air. Thus, C_p was supposed to have a large uncertainty due to this simplification, and assumed to be uncertain within $\pm 15\%$ ¹. The heating value of JP8 is well documented [50], and is reported to be $43,240 \pm 210 \text{ kJ/kg}$. Among the experimental data presented in the thesis, the maximum precision uncertainty is $\pm 2.53\%$.

The bias uncertainty is propagated from the measured values such as the mass

¹At the inlet conditions (300 K and 1 atm), C_p of the JP8-air mixture is approximately 1066 J/kgK [50], which is 6% larger than pure air's 1005 J/kgK. At a typical exit condition (1000 K and 1 atm), C_p of air is 1143 J/kgK, whereas that of equilibrium, frozen, and fixed composition burned gas is about 1300 J/kgK ($\phi = 1$ with $C_n H_{2n}$ fuel) [44], which is 14% larger than the air's. This is why $\pm 15\%$ used.

flow rates and the temperatures:

$$b_{\eta_{overall}} = \frac{\partial \eta_{overall}}{\partial \dot{m}_f} b_{\dot{m}_f} + \frac{\partial \eta_{overall}}{\partial \dot{m}_a} b_{\dot{m}_a} + \frac{\partial \eta_{overall}}{\partial T_{exit}} b_{T_{exit}} \quad (E.7)$$

The maximum bias uncertainty is $\pm 4.72\%$ ($\phi = 0.7$, $\dot{m} = 0.05 \text{ g/sec}$).

The total uncertainty in the overall combustor efficiency is:

$$u_{\eta_{overall}} = \sqrt{p_{\eta_{overall}}^2 + b_{\eta_{overall}}^2} = \pm 5.36\% \quad (E.8)$$

E.2.3 Chemical efficiency

The chemical efficiency is given by:

$$\eta_{chem} = \frac{[(\dot{m}_a + \dot{m}_f)h_{exit} - \dot{m}_a h_{inlet}] + q_{loss}}{\dot{m}_f h_f} \quad (E.9)$$

For ease of calculation, a new variable, ξ , is defined as:

$$\xi \equiv \frac{q_{loss}}{\dot{m}_f h_f} = \frac{(h_u A_u + h_l A_l)(T_{wall} - T_{\infty}) + \varepsilon \sigma (A_u + A_l)(T_{wall}^4 - T_{\infty}^4)}{\dot{m}_f h_f} \quad (E.10)$$

Then,

$$\eta_{chemical} = \eta_{overall} + \xi \quad (E.11)$$

Let us first evaluate the uncertainties in the variable ξ using the same procedure as the previous analyses,

$$p_{\xi} = \sqrt{\left(\frac{\partial \xi}{\partial h_u} p_{h_u}\right)^2 + \left(\frac{\partial \xi}{\partial h_l} p_{h_l}\right)^2 + \left(\frac{\partial \xi}{\partial \varepsilon} p_{\varepsilon}\right)^2 + \left(\frac{\partial \xi}{\partial h_f} p_{h_f}\right)^2} \quad (E.12)$$

The two heat transfer coefficients were assumed to have uncertainties of $\pm 10\%$. And an uncertainty of ± 0.1 was assumed in the value of ε . For p_{h_f} , $\pm 210 \text{ kJ/kg}$ was used as before. Then, the precision uncertainty for ξ is computed to be $\pm 3.70\%$.

The bias uncertainty in the variable ξ is:

$$b_{\xi} = \frac{\partial \xi}{\partial \dot{m}_f} b_{\dot{m}_f} + \frac{\partial \xi}{\partial T_{wall}} b_{T_{wall}} = \pm 8.72\% \quad (\text{E.13})$$

Using $p_{\eta_{overall}} = \pm 2.53\%$ and $b_{\eta_{overall}} = \pm 4.72\%$,

$$p_{\eta_{chemical}} = \sqrt{p_{\eta_{overall}}^2 + p_{\xi}^2} = \pm 4.48\% \quad (\text{E.14})$$

$$b_{\eta_{chemical}} = b_{\eta_{overall}} + b_{\xi} = \pm 13.44\% \quad (\text{E.15})$$

Finally,

$$u_{\eta_{chemical}} = \sqrt{p_{\eta_{chemical}}^2 + b_{\eta_{chemical}}^2} = \pm 14.17\% \quad (\text{E.16})$$

Again, high uncertainties in the fuel flow rate measurement propagate through, and result in a large uncertainty in the chemical efficiency.

E.2.4 Thermal efficiency

The thermal efficiency of the combustor is calculated by:

$$\eta_{thermal} = \frac{(\dot{m}_a + \dot{m}_f)h_{exit} - \dot{m}_a h_{inlet}}{[(\dot{m}_a + \dot{m}_f)h_{exit} - \dot{m}_a h_{inlet}] + q_{loss}} \quad (\text{E.17})$$

The precision uncertainty and the bias uncertainty are given by:

$$p_{\eta_{thermal}} = \sqrt{\left(\frac{\partial \eta_{thermal}}{\partial C_p} p_{C_p}\right)^2 + \left(\frac{\partial \eta_{thermal}}{\partial h} p_h\right)^2 + \left(\frac{\partial \eta_{thermal}}{\partial \varepsilon} p_{\varepsilon}\right)^2} = \pm 3.80\% \quad (\text{E.18})$$

$$b_{\eta_{thermal}} = \frac{\partial \eta_{thermal}}{\partial \dot{m}_a} b_{\dot{m}_a} + \frac{\partial \eta_{thermal}}{\partial T_{exit}} b_{T_{exit}} + \frac{\partial \eta_{thermal}}{\partial T_{wall}} b_{T_{wall}} = \pm 2.24\% \quad (\text{E.19})$$

Therefore, the uncertainty in the thermal efficiencies is:

$$u_{\eta_{thermal}} = \sqrt{p_{\eta_{thermal}}^2 + b_{\eta_{thermal}}^2} = \pm 4.41\% \quad (\text{E.20})$$

E.2.5 Peclet number

Peclet number is defined as the ratio between the flow residence time-scale in the combustion chamber and the diffusion time-scale of the fuel molecules onto catalyst surfaces:

$$\begin{aligned}
 Pe &= \frac{\tau_{res}}{\tau_{reac}} \\
 &= \frac{\frac{\rho V}{\dot{m}}}{(-\ln(0.1)) \frac{R^2}{Sh_D D_{ab}}}
 \end{aligned}
 \tag{E.21}$$

This can be rewritten as:

$$Pe = \left(\frac{1.013 \times 10^{-2} \rho_0 T_0 V Sh_D \sqrt{1/M_a + 1/M_b}}{(-\ln(0.1)) P_0 R^2 (v_a^{1/3} + v_b^{1/3})^2} \right) \frac{T_{ave}^{0.75}}{\dot{m}}
 \tag{E.22}$$

Because Peclet number is a comparison between characteristic time-scales, it is only meaningful in the context of relative numbers. Therefore, precision uncertainties associated with values that are constant throughout the experiment do not need to be considered. Only bias uncertainties in the values of T_{ave} and \dot{m} propagate:

$$b_{Pe} = \frac{\partial Pe}{\partial T_{ave}} b_{T_{ave}} + \frac{\partial Pe}{\partial \dot{m}} b_{\dot{m}}
 \tag{E.23}$$

Using $b_{T_{ave}} = \pm 16 \text{ K}^2$ and $b_{\dot{m}} = \pm 0.0015 \text{ g/sec}$, the uncertainty in the Peclet number calculation is 0.183.

Table E.2 lists the 95%-confidence uncertainties of the derived quantities including the equivalence ratio, efficiencies, and Peclet number.

$${}^2 b_{T_{ave}} = \frac{1}{2} b_{T_{exit}}$$

Measurements	95%-confidence uncertainty
equivalence ratio	± 0.1552
combustor efficiency	$\pm 5.36\%$
chemical efficiency	$\pm 14.17\%$
thermal efficiency	$\pm 4.41\%$
Peclet number	± 0.183

Table E.2: Uncertainties of the derived quantities

Bibliography

- [1] A. Mehra, X. Zhang, A. A. Ayon, I. A. Waitz, M. A. Schmidt, and C. M. Spadaccini. "A Six-Wafer Combustion System for a Silicon Micro Gas Turbine Engine". *IEEE/ASME Journal of Microelectromechanical Systems*, Vol. 9, No. 4, pp. 517-527, December 2000.
- [2] C. M. Spadaccini. "Combustion Systems for Power-MEMS Applications". PhD thesis, Massachusetts Institute of Technology, Department of Aeronautics and Astronautics, 2004.
- [3] J. A. Schetz. "Injection and Mixing in Turbulet Flow". *AIAA Progress in Aeronautics and Astronautics*, Vol. 68, 1980.
- [4] "ICAO Approves Methanol Cartridges on Planes". *Fuel Cells Belletin*, Vol. 2006, Issue 1, pp. 6, January 2006.
- [5] Specialists in Business Information. "U.S. Market for Residential Generators". <http://www.sbireports.com>, September 2007.
- [6] Smart Fuel Cell. <http://www.efoy.de>.
- [7] A. H. Epstein, S. D. Senturia, O. Al-Midani, G. Anathasuresh, A. Ayon, K. Breuer, K-S. Chen, F. F. Ehrich, E. Esteve, L. Frechette, G. Gauba, R. Ghodssi, C. Groshenry, S. A. Jacobson, J. L. Kerrebrock, J. H. Lang, C-C Lin, A. London, J. Lopata, A. Mehra, J. O. Mur Miranda, S. Nagle, D. J. Orr,

- E. Piekos, M. A. Schmidt, G. Shirley, S. M. Spearing, C. S. Tan, Y-S Tzeng, and I. A. Waitz. "Micro-Heat Engines, Gas Turbines, and Rocket Engines - The MIT Microengine Project -". AIAA 97-1773, 28th AIAA Fluid Dynamics Conference, 4th AIAA Shear Flow Control Conference, Snowmass Village, CO, June 1997.
- [8] A. H. Epstein, S. A. Jacobson, J. M. Protz, and L. G. Frechette. "Shirtbutton-sized Gas Turbines: The Engineering Challenges of Micro High Speed Rotating Machinery". In *Proceedings of the 8th Int'l Symposium on Transport Phenomena and Dynamics of Rotating Machinery (ISROMAC'8)*, Honolulu, HI, January 2000.
- [9] S. A. Jacobson. "Aerothermal Challenges in the Design of a Microfabricated Gas Turbine Engine". AIAA 98-2545, 29th AIAA Fluid Dynamics Conference, Albuquerque, NM, June 1998.
- [10] J. M. Protz. "An Assessment of the Aerodynamic, Thermodynamic, and Manufacturing Issues for the Design, Development, and Microfabrication of a Demonstration Micro Engine". PhD thesis, Massachusetts Institute of Technology, Department of Aeronautics and Astronautics, 2000.
- [11] N. Savoulides. "Development of a MEMS Turbocharger and Gas Turbine Engine". PhD thesis, Massachusetts Institute of Technology, Department of Aeronautics and Astronautics, 2004.
- [12] B. Philippon. "Design of a Film-Cooled Micro Turbine". Master's thesis, Massachusetts Institute of Technology, Department of Aeronautics and Astronautics, 2001.
- [13] S. W. Evans. "Thermal Design of a Cooled Micro Gas Turbine". Master's thesis, Massachusetts Institute of Technology, Department of Aeronautics and Astronautics, 2001.

- [14] L. G. Frechette. "Development of a Microfabricated Silicon Motor-Driven Compression System". PhD thesis, Massachusetts Institute of Technology, Department of Aeronautics and Astronautics, 2000.
- [15] C. C. Lin. "Development of a Microfabricated Turbine-Driven Air Bearing Rig". PhD thesis, Massachusetts Institute of Technology, Department of Mechanical Engineering, 1999.
- [16] C. W. Wong. "Desing, Fabrication, Experimentation and Analysis of High-Speed Microscale Gas Bearings". Master's thesis, Massachusetts Institute of Technology, Department of Mechanical Engineering, 2001.
- [17] L. X. Liu. "Theory for Hydrostatic Gas Journal Bearings for Micro-Electro-Mechanical Systems". PhD thesis, Massachusetts Institute of Technology, Department of Mechanical Engineering, 2005.
- [18] C. J. Teo. "MEMS Turbomachinery Rotordynamics: Modeling, Design and Testing". PhD thesis, Massachusetts Institute of Technology, Department of Aeronautics and Astronautics, 2006.
- [19] A. Mehra. "Development of a High Power Density Combustion System for a Silicon Micro Gas Turbine Engine". PhD thesis, Massachusetts Institute of Technology, Department of Aeronautics and Astronautics, 2000.
- [20] I. A. Waitz, G. Gauba, and Y-S Tzeng. "Combustor for Micro Gas Turbine Engines". *ASME Journal of Fluids Engineering*, Vol. 20, pp. 109-117, March 1998.
- [21] Y-S Tzeng. "An Investigation of Microcombustion Thermal Phenomena". Master's thesis, Massachusetts Institute of Technology, Department of Aeronautics and Astronautics, 1997.

- [22] J. Lee. “Computational Modeling of a Silicon Microcombustor”. Master’s thesis, Massachusetts Institute of Technology, Department of Aeronautics and Astronautics, 2000.
- [23] J. Peck. “Development of a Catalytic Combustion System for the MIT Micro Gas Turbine Engine”. Master’s thesis, Massachusetts Institute of Technology, Department of Aeronautics and Astronautics, 2003.
- [24] C. M. Spadaccini, A. Mehra, J. Lee, X. Zhang, S. Lukachko, and I. A. Waitz. “High Power Density Silicon Combustion Systems for Micro Gas Turbine Engines”. *ASME Journal of Engineering for Gas Turbine and Power*, Vol. 125, pp. 709-719, July 2003.
- [25] C. M. Spadaccini, X. Zhang, C. P. Cadou, N. Miki, and I. A. Waitz. “Preliminary Development of a Hydrocarbon-Fueled Catalytic Micro-combustor”. *Sensors and Actuators A: Physical*, Vol. 103, pp. 219-224, January 2003.
- [26] C. M. Spadaccini, J. Peck, and I. A. Waitz. “Catalytic Combustion Systems for Microscale Gas Turbine Engines”. *Journal of Engineering for Gas Turbines and Power*, Vol. 129, pp. 49-60, January 2007.
- [27] A. A. Ayon, C. C. Lin, R. Braff, R. Bayt, H. H. Sawin, and M. A. Schmidt. “Etching Characteristics and Profile Control in a Time Multiplexed Inductively Coupled Plasma Etcher”. Solid State Sensors and Actuator Workshop, Hilton Head Island, SC, June 1998.
- [28] A. A. Ayon, J. Protz, R. Khanna, X. Zhang, and A. H. Epstein. “Application of Deep Silicon Etching and Wafer Bonding in the MicroManufacturing of Turbochargers and Micro-Air Vehicles”. 47th International Symposium of the American Vacuum Society, Boston, MA, October 2000.

- [29] N. Miki, X. Zhang, R. Khanna, A. A. Ayon, D. Ward, and S. M. Spearing. "Multi-Stack Silicon-Direct Wafer Bonding for 3D MEMS Manufacturing". *Sensors and Actuators A: Physical*, Vol. 103, pp. 194-201, 2003.
- [30] A. Mehra and I. A. Waitz. "Development of a Hydrogen Combustor for a Microfabricated Gas Turbine Engine". The Solid-State Sensor and Actuator Workshop, Hilton Head Island, SC, June 1998.
- [31] W. M. Yang, S. K. Chou, C. Shu, H. Xue, Z. W. Li, D. T. Li, and J. F. Pan. "Microscale Combustion Research for Application to Micro Thermophotovoltaic Systems". *Energy Conversion and Management*, Vol. 44, pp. 2625-2634, 2003.
- [32] J. M. Hatfield and R. B. Peterson. "A Catalytically Sustained Microcombustor Burning Propane". IMECE, New York, NY, November 2001.
- [33] D. C. Kyritsis, B. Coriton, F. Faure, S. Roychoudhury, and A. Gomez. "Optimization of a Catalytic Combustor Using Electrosprayed Liquid Hydrocarbons for Mesoscale Power Generation". *Combustion and Flame*, Vol. 139, pp. 77-89, 2004.
- [34] W. Deng, J. F. Klemic, X. Li, M. A. Reed, and A. Gomez. "Liquid Fuel Microcombustor Using Microfabricated Multiplexed Electrospray Sources". In *Proceedings of the Combustion Institute*, volume Vol. 31, No. 2, pp. 2239-2246, January 2007.
- [35] E. N. Sieder and G.E. Tate. "Heat Transfer and Pressure Drop of Liquids in Tubes". *Industrial and Engineering Chemistry*, Vol. 28, No. pp. 1429-1435, 1936.
- [36] R. H. S. Winterton. "Where did the Dittus and Boelter equation come from?". *International Journal of Heat and Mass Transfer*, Vol. 41, Issue 4-5, pp. 809-810, 1998.

- [37] K-S. Chen. "Materials Characterization and Structural Design of Ceramic Microturbomachinery". PhD thesis, Massachusetts Institute of Technology, 1999.
- [38] A. Lefebvre, W. Freeman, and L. Cowell. "Spontaneous Ignition Delay Characteristics of Hydrocarbon Fuel/Air Mixtures". Technical report, NASA Contractor Report 175064, Lewis Research Center, February 1986.
- [39] W. J. Dodds and D. W. Bahr. *Combustion System Design, Design of Modern Gas Turbine Combustors*. Academic Press Limited, 1990.
- [40] K. K. Kuo. *Principles of Combustion*. Wiley, 1986.
- [41] Goodfellow Corporation. "Technical data: sapphire".
<http://www.goodfellow.com>.
- [42] W. M. Yim and R. J. Paff. "Thermal Expansion of AlN, Sapphire, and Silicon". *Journal of Applied Physics*, Vol. 45, Issue 3, March 1974.
- [43] R. E. Hayes and S. T. Kolaczkowski. *Introduction to Catalytic Combustion*. Gordon and Breach Science Publishers, 1997.
- [44] J. Heywood. *Internal Combustion Engine Fundamentals*. McGraw-Hill, first edition, 1988.
- [45] A. F. Mills. *Basic Heat and Mass Transfer*. Prentice Hall, second edition, 1999.
- [46] F. P. Incropera and D. P. DeWitt. *Fundamentals of Heat and Mass Transfer*. Wiley, fifth edition, 2002.
- [47] A. F. Mills. *Heat Transfer*. Prentice Hall, second edition, 1998.
- [48] V. V. Klimenko. "A Generalized Correlation for Two-phase Forced Flow Heat Transfer". *Int. J. Heat Mass Transfer*, Vol. 31, pp. 541-552, 1988.

- [49] National Institute of Standards and Technology. *Chemistry Standard Reference Database*.
- [50] Coordinating Research Council. *Handbook of Aviation Fuel Properties*, 1983.
- [51] National Renewable Energy Laboratory. *Advanced Vehicles and Fuels Research*.
- [52] HOYA Corporation USA. corporate literature. <http://www.hoyaoptics.com>, Fremont, CA, 2007.
- [53] Apple Rubber Products Inc. "MicrOringTM Seals from Apple Rubber", 1996.
- [54] F. Laermer and A. Schilp. "Method of Anisotropically Etching Silicon". Robert Bosch GmbH: U.S. Patent 5,501,893.
- [55] M. J. Madou. *Fundamentals of Microfabrication*. CRC Press, second edition, 2002.
- [56] J. L. Kerrebrock. *Aircraft Engines and Gas Turbines*. The MIT Press, second edition, 1992.
- [57] R. A. Dalla Betta, J. C. Schlatter, D. K. Yee, D. G. Loffler, and T. Shoji. "Catalytic Combustion Technology to Achieve Ultra Low NO_x Emissions: Catalyst Design and Performance Characteristics". *Catalysis Today*, Vol. 26, Issue 3-4, pp. 329-335, December 1995.
- [58] R. A. Dalla Betta. "Catalytic Combustion Gas Turbine Systems: the Preferred Technology for Low Emissions Electric Power Production and Co-generation". *Catalysis Today*, Vol. 35, Issue 1-2, pp. 129-135, March 1997.
- [59] R. A. Dalla Betta and T. Rostrup-Nielsen. "Application of Catalytic Combustion to a 1.5 MW Industrial Gas Turbine". *Catalysis Today*, Vol 47, Issue 1-4, pp. 369-375, January 1999.

- [60] K. W. Beebe, K. D. Cairns, V. K. Pareek, S. G. Nickolas, J. C. Schlatter, and T. Tsuchiya. "Development of Catalytic Combustion Technology for Single-digit Emissions from Industrial Gas Turbines". *Catalysis Today*, Vol. 59, Issue 1-2, pp. 95-115, June 2000.
- [61] R. Carroni, V. Schmidt, and T. Griffin. "Catalytic Combustion for Power Generation". *Catalysis Today*, Vol. 75, Issue 1-4, pp. 287-295, July 2002.
- [62] V. Dupont, S.-H. Zhang, and A. Williams. "High-Temperature Catalytic Combustion and Its Inhibition of Gas-Phase Ignition". *Energy and Fuels*, Vol. 9, No. 6, pp. 1576-1584, 2002.
- [63] J. F. Griffiths, K. J. Hughes, and R. Porter. "The Role and Rate of Hydrogen Peroxide Decomposition during Hydrocarbon Two-stage Autoignition". *Proceedings of the Combustion Institute*, Vol. 30, Issue 1, pp. 1083-1091, January 2005.
- [64] W. Kim. Personal communication. Massachusetts Institute of Technology, Department of Materials Science and Engineering, 2007.
- [65] S. A. Jacobson. Personal communication. Massachusetts Institute of Technology, Gas Turbine Laboratory, 2008.
- [66] T. G. Beckwith, R. D. Marangoni, and J. H. Leinhard. *Mechanical Measurements*. Addison-Wesley Publishing Company, fifth edition, 1993.